Discovery of Heterometallic Layered Oxides using Solid-State Reactions of Nano-Precursors

Samuel John Alexander

A thesis submitted to University College London for the degree of Doctor of Philosophy

Supervisor: Prof. Jawwad A. Darr

Department of Chemistry, University College London.

October 2011

I, Samuel John Alexander confirm the work presented in this thesis is my own. Where information has been derived from other sources, I confirm that this has been indicated in the thesis.

Samuel John Alexander

Abstract

The synthesis of new solid-state materials is often a laborious task due to the low speed of diffusion in bulk solids, meaning each reaction requires high-temperatures and multiple steps. Shortening diffusion distances has been shown to increase reaction rates and lower reaction temperatures.

This thesis addresses the need to increase the rate of solid-state materials discovery, by heat-treatment of nanosized precursors. The nano-precursors were synthesised using continuous hydrothermal flow synthesis, CHFS. In CHFS a flow of metal nitrate salts are brought into contact with a flow of supercritical water to precipitate metal oxides and/or hydroxides. The reaction between $La(OH)_3$ and $Ni(OH)_2$ co-precipitated using CHFS was investigated using *in-situ* X-ray diffraction. This resulted in the formation of La_2NiO_4 in 78 minutes, an order of magnitude faster than when using more traditional routes, highlighting the effectiveness of this approach.

A high-throughput CHFS reactor was then used to synthesise $La_4Ni_{2.7}M_{0.3}O_{10-\delta}$ (where M = V, Cr, Mn, Fe, Co, Cu and Al). By calcining the nano-precursors for these compositions in parallel it was possible to reduce the synthesis time to make twenty-four solid-state compounds to 12 hours. Structure and properties were screened and, $La_4Ni_{2.7}V_{0.3}O_{10-\delta}$, $La_4Ni_{2.7}Cr_{0.3}O_{10-\delta}$, $La_4Ni_{2.7}Mn_{0.3}O_{10-\delta}$ and $La_4Ni_{2.7}Al_{0.3}O_{10-\delta}$ were characterised. Subsequently this process was carried out using automation to increase the number of compositions synthesised. Firstly, for the $La_4Ni_{3-x}Fe_xO_{10-\delta}$ system (x = 0.0 – 3.0 and Δx = 0.1), 62 samples were synthesised, resulting in identifying a greatly increased phase boundary, up to a maximum Fe content of $La_4Ni_{2.06}Fe_{0.94}O_{10}$. Secondly for the $La_4Ni_{3-x}M_xO_{10-\delta}$ and $La_3Ni_{2-x}M_xO_{7-\delta}$ systems (x = 0.0 – 2.0. Δx = 0.2 and M = Mn, Al, Pd, Ga) in which 240 samples were synthesised. $La_4Ni_{3-x}Ga_xO_{10-\delta}$ was isolated up to a maximum Ga content of x = 0.6, and $La_2Ni_{1-x}Pd_xO_4$ could be synthesised with a maximum Pd content of x = 0.4.

Acknowledgements

I would like to thank my supervisor Jawwad for his help and support over the last three years. I would also like to thank Jeremy Cockcroft and Martin Vickers, who have been a great help in learning powder diffraction. Dan Brett is thanked for his help and advice in constructing electrical equipment, fuel cell science, and a few beers along the way. Kevin Phillips in the basement is thanked for his help with electron microscopy. Andrew Smith is thanked for using his own beamtime to collect EXAFS data for four of my samples, and I would like to thank Sankar for not only analysing the data, but having the time to sit and explain to me what and how you were doing it. I would like to thank Tian, Kenan, Kathryn and Suella, all ex members of the group who designed and put together RAMSI along with Jawwad. I'm glad I put all your good work to use. Along the way I enjoyed trips to Diamond Light Source and the ILL so I extend a word of thanks to both those organisations. In particular Julia, Stephen and Chiu on I11 at Diamond for not only keeping my experiments running but lending an extra hand in your own time. It was greatly appreciated.

I would also like to thank my fellow group members Sofia, Rob Chris Josie Raul and Eva who have helped me along the way with advice, cake and coffee. A special mention in particular to Rob, Chris and the staff and management of the Euston Tap for the warm welcome on a Friday evening. I would like thank my family whose support has been invaluable in me completing this thesis.

Finally I would like to thank Faye who has had to put up with me complaining about having to be at work at 9:30! and more recently for dealing with what she has called 'thesis Sam' without a bad word. I'll meet you in the Tap for a swift half, remember no science after 6!

Table of Contents

List of Figures

Chapter 1

Chapter 2

Chapter 3

Chapter 4

Chapter 5

Chapter 6

0.2) after heat-treatment for 12 hours in air. At% of Al = $n_{Al}/(n_{La}+n_{Ni}+n_{Al})$. Each point represents a unique composition, some of which are mixtures and some of which are phase pure compounds. In each case the phase identified from powder XRD is given in the key.,,,,,,,,,,,,,,,,,,,,...139

Figure 6.7. Phase diagram at room temperature pressure for the phases formed from CHFS precursors for the compositions La_3:$Ni_{2-x}Al_x$ (where x = 0.2 – 0.0 and Δx = 0.2) after heat-treatment for 12 hours in air. At% of Al = $n_{Al}/(n_{La}+n_{Ni}+n_{Al})$. Each point represents a unique composition, some of which are mixtures and some of which are phase pure compounds. In each case the phase identified from powder XRD is given in the key...140

Figure 6.8. Phase diagram at room temperature pressure for the phases formed from CHFS precursors for the compositions La_4:$Ni_{3-x}Ga_x$ (where x = 0.2 – 0.0 and Δx = 0.2) after heat-treatment for 12 hours in air. At% of Ga = $n_{Ga}/(n_{La}+n_{Ni}+n_{Ga})$. Each point represents a unique composition, some of which are mixtures and some of which are phase pure compounds. In each case the phase identified from powder XRD is given in the key. Samples marked with an asterisk were selected for further investigation...141

Figure 6.9. Phase diagram at room temperature pressure for the phases formed from CHFS precursors for the compositions La_3:$Ni_{2-x}Ga_x$ (where x = 0.2 – 0.0 and Δx = 0.2) after heat-treatment for 12 hours in air. At% of Ga = $n_{Ga}/(n_{La}+n_{Ni}+n_{Ga})$. Each point represents a unique composition, some of which are mixtures and some of which are phase pure compounds. In each case the phase identified from powder XRD is given in the key...142

Figure 6.10. Le Bail refinement of $La_2Ni_{0.67}Pd_{0.33}O_{4+\delta}$ (nominal composition). $R_{wp} = 0.1163$, $R_p = 0.0796$, $\chi^2 = 2.781$. Measured data points are shown in red, calculated profile is shown in green and the difference shown in purple. Vertical tickmarks show the calculated peak positions for orthorhombically distorted $La_2Ni_{0.67}Pd_{0.33}O_{4+\delta}$ phase (lower) and NiO (upper) respectively.............................144

Figure 6.11. The NiO (111) reflection demonstrating the asymmetry, and hence the inhomogeneity. Measured data points are shown in red, calculated profile is shown in green and the difference shown in purple. The vertical tickmark shows the calculated peak position for NiO...145

Figure 6.12. Graph showing change in unit cell volume with nominal Pd content in $La_2Ni_{1-x}Pd_xO_{4+\delta}$. Error bars are smaller than symbols in all cases...........................146

List of Tables

Chapter 1

Chapter 2

Chapter 3

Chapter 4

Chapter 5

Chapter 6

List of Abbreviations

BPR – Back pressure regulator
CHFS – Continuous hydrothermal flow synthesis
CGO – Ceria doped gadolinia
DC – Direct current
DI – Deionised
EDX – Energy dispersive X-ray spectroscopy
EXAFS – Extended X-ray absorption fine structure
GUI – Graphical user interface
HiTCH – High-throughput continuous hydrothermal
HPLC – High-pressure liquid chromatography
ID – Internal diameter
IT-SOFC – Intermediate temperature solid oxide fuel cell
LSCF – $La_{1-x}Sr_xGa_{1-y}Mg_yO_{3-(x/2)-(y/2)}$
LSGM – $La_{1-x}Sr_xCo_{1-y}Fe_yO_3$
LSM – $La_{1-x}Sr_xMnO_3$
MAC – Multi-analyser crystal
MBE – Molecular beam epitaxy
OD – Outside diameter
PG – Pressure gauge
PLD – Pulsed laser deposition
PRV – Pressure relief valve
PSD – Position sensitive detector
PVD – Physical vapour deposition
RAMSI – Rapid automated materials synthesis instrument
scH_2O – Supercritical water
SEM – Scanning electron microscopy
SOFC –Solid oxide fuel cell
SS – Stainless steel
SV – Switch valve
TPB – Triple phase boundary
YSZ – Yttria stabilised zirconia
XRD – X-ray diffraction

Chapter 1

Introduction and Literature Review

1.1. Solid Oxide Fuel Cells

Solid oxide fuel cells (SOFCs) are electrochemical devices that operate at high temperatures (973 – 1273 K) and typically run on a fuel containing H_2 and CO, which are formed by steam reformation of hydrocarbons on the anode side of the cell. Air is used as an oxidant to produce H_2O, CO_2 and energy. SOFCs are usually constructed from three principle components, an anode, a solid oxide electrolyte and a cathode. The anode is an electrically and ionically conductive cermet, which must be porous in order to allow the fuel gasses to reach the reaction interface. The Electrolyte is an ionically conductive electrical insulator which conducts O^{2-} ions across the to the cathode side of the cell. In order to obtain an O^{2-}conductivity high enough to have a practical cell the operating temperature must be high often in excess of 973 K. The cathode material in an SOFC is a mixed electrical and ionic conductor which must be porous to allow the fuel gas to reach the reaction surface and must have high catalytic activity for the reduction of O_2. A schematic representation of the construction of a SOFC and the reactions at each component is represented in figure 1.1 below.

Figure 1.1. A schematic representation of a SOFC. Figure adapted from (Ormerod 2002)

Energy is generated from a fuel containing H_2 and CO, which reacts with O^{2-} to produce CO_2, H_2O and $4e^-$ as in equation 1.1 and 1.2.

$$H_2 + O^{2-} \rightarrow H_2O + 2e^- \qquad \textbf{(1.1)}$$

$$CO + O^{2-} \rightarrow CO_2 + 2e^- \qquad \textbf{(1.2)}$$

The electrons produced travel through an external circuit (where they can do work) to the cathode where they are used in the reduction of oxygen, shown in equation 1.3.

$$O_2 + 4e^- \rightarrow 2O^{2-} \qquad \textbf{(1.3)}$$

The O^{2-} anions produced pass back through the solid electrolyte to be used in reaction 1.2. The equation for the process is represented in equation 1.4.

$$H_2 + CO + O_2 \rightarrow H_2O + CO_2 + \Delta E \qquad \textbf{(1.4)}$$

1.1.1. Anodes

Anode materials in SOFCs should be porous and be both electrically and ionically conductive. They are generally cermets (a ceramic and metal mixture) with the metal being used as a conducting phase. The fuel gases are reducing in nature, however these metals cannot oxidise at operating temperature (973 – 1273 K) therefore the metals used are generally limited to Ni and Co.(Ormerod 2002) The most widely used anode is a Ni-$(ZrO_2)_{0.9}(Y_2O_3)_{0.1}$ (Ni-YSZ) because it has a high stability and thermal compatibility with yttria stabilised zirconia (YSZ) (a commonly used solid electrolyte), and good electrocatalytic activity.(Lashtabeg et al. 2006) The thermal compatibility relates to the similar thermal expansion that both materials undergo on heating. If the thermal expansion values are not compatible it can lead to mechanical failure of the fuel cell.

Reactions at the anode occur at the triple-phase boundary (TPB), which is the junction between the electrolyte, the metal and the gaseous fuel. The TPB is represented schematically in figure 1.2.

Figure 1.2. Schematic diagram of the triple phase boundary. Figure adapted from (McIntosh et al. 2004).

Given the rate of reaction is dictated by the area of the TPB, it is therefore desirable to increase the surface area of the TPB, often by using nanosized materials. It is also therefore important to have a good dispersion of Ni metal within the YSZ to maximise conductivity.(McIntosh et al. 2004) It was shown using CHFS that a good dispersion of Ni in nanosized YSZ could be achieved. Also, reduced sintering of Ni metal was observed after heat-treatment (via spark plasma sintering) as characterised by a Ni particle size range of 150 – 300 nm, compared with 500 – 2000 nm in commercial powders, representing a potentially large increase in the size of the TPB.(Weng et al. 2010)

1.1.2. Electrolytes

The electrolyte material for an SOFC must be electrically insulating but have high oxygen ion conductivity. They must also be fully dense to prevent mixing of the fuel and oxidant gas flows. The most commonly used material is yttria stabilised zirconia, YSZ (8 mol. % Y in ZrO_2). This material has high oxide ion mobility, a good stability in both oxidising and reducing atmospheres and is made of cheap abundant oxides. However, in order to achieve an oxide ion conductivity high enough for the fuel cell to work efficiently, temperatures of 973 – 1273 K are required. Many other materials have consequently been investigated in an attempt to achieve high oxide ion conductivities at lower temperatures. Ceria doped gadolina

(CGO) and $La_{1-x}Sr_xGa_{1-y}Mg_yO_{3-(x/2)-(y/2)}$ (LSGM) in particular have been identified as potential alternatives to YSZ.(Lashtabeg et al. 2006) A range of solid electrolytes and their measured conductivities are presented in figure 1.3.

Figure 1.3. Ionic conductivities of selected SOFC electrolyte materials. Figure adapted from (Azad et al. 1994).

1.1.3. Cathodes

The cathode material in an SOFC is a mixed electrical and ionic conductor which must be porous to allow the fuel gas to reach the reaction surface and must have high catalytic activity for the reduction of O_2. Cathode materials are generally a form of perovskite with the structure $LnMO_3$, (where Ln = lanthanide and M = transition metal) as these materials display high electrical and oxide ion conductivities within the temperature region of SOFC operation.(Skinner 2001) Two popular perovskite based SOFC cathode materials are $La_{1-x}Sr_xMnO_3$ (LSM) and $La_{1-x}Sr_xCo_{1-y}Fe_yO_3$ (LSCF). LSM is favoured as a cathode material as it has a high electrical conductivity and high activity for the electrochemical reduction of O_2.(Jacobson 2010) It also displays good chemical compatibility with YSZ and LSGM.(Jacobson 2010) LSM has been shown to react with YSZ when sintering

temperatures greater than 1373 K are used, however at an operating temperature between 973 – 1173 K no reaction was observed between LSM and YSZ after heating for 15 hours.(Yamamoto et al. 1987) LSCF has a superior conductivity to LSM however it also possesses a greater reactivity towards zirconia based electrolyte materials. Therefore LSCF is used in fuel cells using ceria electrolytes.(Ormerod 2002)

Whilst perovskites have been traditionally investigated as SOFC cathodes, more recently variations of perovskite, namely layered perovskites have been identified as demonstrating rapid oxygen ion diffusion and high electrical conductivity.(Tarancón et al. 2010; Taskin et al. 2007) Two main types of layered perovskite have been identified, Ruddlesden-Popper type lanthanum nickelates, and double perovskites. The former are discussed in detail below. The latter have the formula $A'A''B_2O_{5+\delta}$ (where A' = lanthanide cation, A'' = alkali metal, and B = transition metal), and are formed from simple ABO_3 perovskite units as shown in figure 1.4 below.

Figure 1.4. a) A simple $A'_{0.5}A''_{0.5}O_3$ where B is a transition metal, showing no A-site ordering. b) A layered $A'A''BO_6$ structure, formed by doubling the unit cell, this is only possible to form if the difference in A^{3+}:A'^{2+} ratio is large enough. c) The layered $A'A''BO_{5+\delta}$ ($0.0 < \delta > 1.0$) structure where O anions can be removed from the lanthanide A^{3+} layers to form O^{2-} diffusion channels. Figure adapted from (Taskin et al. 2007).

To form $AA'BO_{5+\delta}$ structures a large enough size ratio between the atomic radius of the A^{3+} and A'^{2+} cation is required. A range of these structures have been discovered which display high electrical conductivities at intermediate temperatures.(Kim et al. 2007) When the alternating alkali earth, and lanthanide planes are formed, large amounts of oxygen are removed from the LnO_x planes leaving a high O^{2-} vacancy concentration and high O^{2-} mobility as a result.(Maignan et al. 1999; Taskin et al. 2007) When electrical characterisation tests were performed on $GdBaCo_2O_{5+\delta}$ in a cell with CGO electrolytes these materials were found to be suitable at intermediate-temperature solid oxide fuel cell (IT-SOFC) operating temperatures between 873 – 973 K,(Tarancón et al. 2007) a result that was further corroborated by Kim *et al.*(Kim et al. 2009)

1.2. Lanthanum Nickelates

Lanthanum nickelates are mixed ionic and electronic conductors, and have shown potential as an IT-SOFC cathode material.(Takahashi et al. 2010) Ruddlesden-Popper type lanthanum nickelates have the formula $La_{n+1}Ni_nO_{3n+1}$ where n = 1, 2, and 3, $La_2NiO_{4+\delta}$, $La_3Ni_2O_{7-\delta}$ and $La_4Ni_3O_{10-\delta}$, respectively, and are represented in figure 1.5. 1.6 and 1.7.(Ruddlesden et al. 1957; Ruddlesden et al. 1958) They are formed of $LaNiO_3$ perovskite layers which extend infinitely in the *ab* plane and are connected by corner sharing NiO_6 octahedra. The perovskite layers are stacked in the *c* plane in n layers, with every n perovskite layers separated by rocksalt-type LaO layers. The average Ni valence increases from 2, to 2.5 to 2.67 through the series n = 1 - 3, the lanthanum cations are always 3+. The mixed Ni valency in the n = 2 and 3 compounds causes the oxygen stoichiometry to become deficient to stabilise the structure. By introducing dopants with increasing valence onto the Ni sites, the oxygen stoichiometry can be made more deficient. Equally by lowering the valence on the Ni site the opposite is true. The n = 1 structure where Ni is only in the 2+ state requires and oxygen excess to create a mixed valency to stabilise the tetragonal structure.(Zhang et al. 1995)

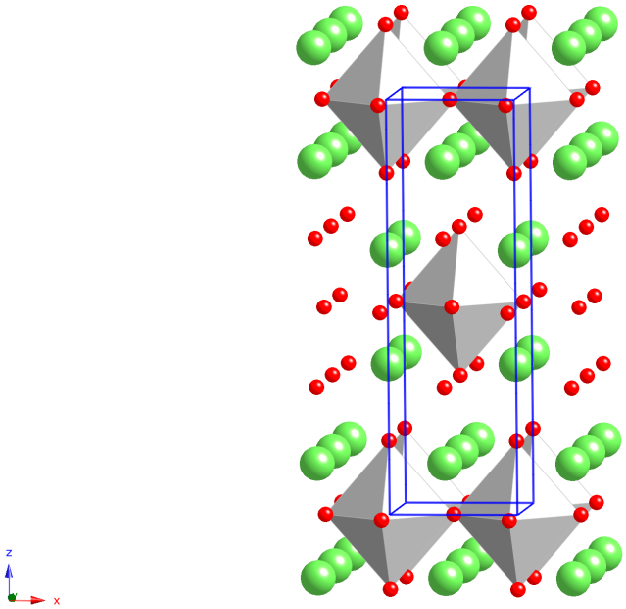

Figure 1.5. Crystal structure of $La_2NiO_{4+\delta}$ viewed close to the (010) direction. Lanthanum cations are represented by green spheres, oxygen anions are represented by red spheres and NiO_6 octahedra are represented by the grey octahedra.

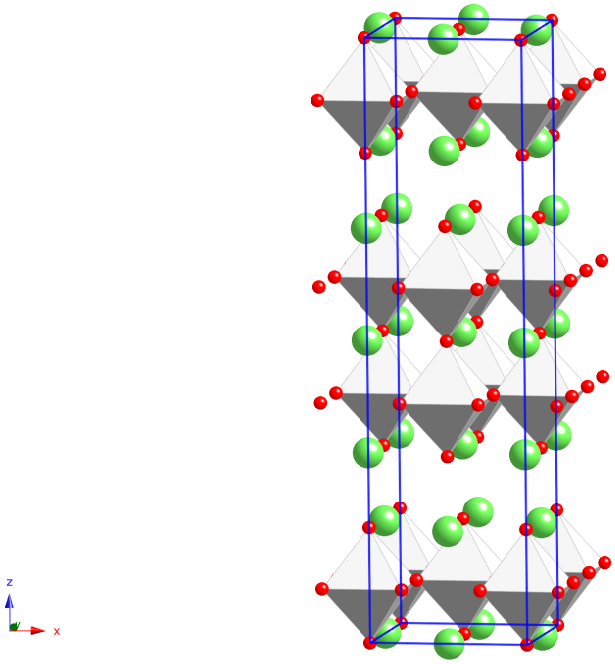

Figure 1.6. Crystal structure of $La_3Ni_2O_{7-\delta}$ viewed close to the (010) direction. Lanthanum cations are represented by green spheres, oxygen anions are represented by red spheres and NiO_6 octahedra are represented by the grey octahedra.

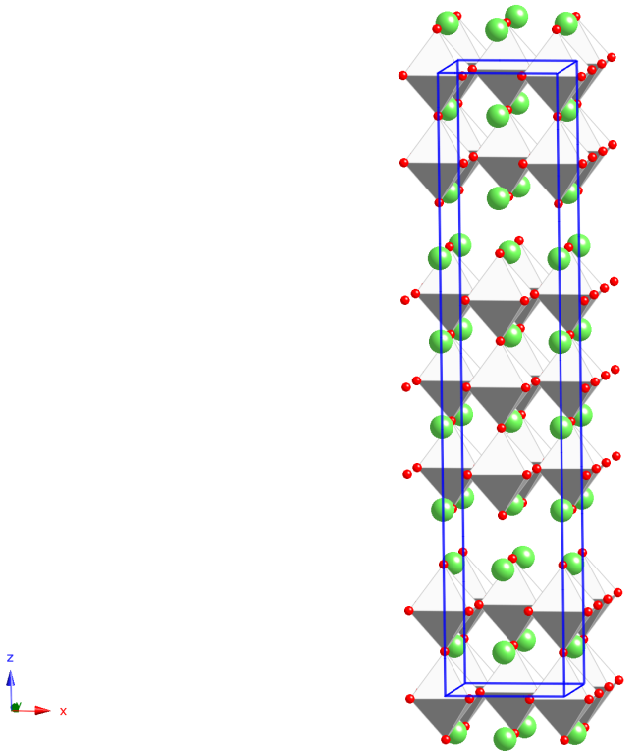

Figure 1.7. Crystal structure of $La_4Ni_3O_{10-\delta}$ viewed close to the (010) direction. Lanthanum cations are represented by green spheres, oxygen anions are represented by red spheres and NiO_6 octahedra are represented by the grey octahedra.

The n = 1 compound crystallises into the ideal tetragonal compound in the I4/mmm space group with cell dimensions of approximately a = 3.87 Å and c = 12.60 Å. Both n = 2 and 3 compounds have orthorhombic symmetry and are reported to crystallise in the Fmmm and Bmab space groups, respectively. The cell dimensions of the n = 2 and 3 compounds are a = 5.40, b = 5.45, c = 20.52 Å and a = 5.41, b = 5.46, c = 27.96 Å, respectively.(Ling et al. 1999)

Ruddlesden-Popper lanthanum nickelates were first reported by Wold and Arnott in 1959,(Wold et al. 1959) however it was not possible to isolate the n = 2 and n = 3 compounds as phase pure materials until the early 90s.(Sreedhar et al. 1994; Zhang et al. 1994; Zhang et al. 1995) Both $La_3Ni_2O_{7-\delta}$ and $La_4Ni_3O_{10-\delta}$ required lengthy heat-treatments of 4 days at 1573 K and 1373 K, respectively, and multiple regrinding stages to isolate as phase pure compound when using a traditional heat and grind approach.(Zhang et al. 1994; Zhang et al. 1995). Table 1.1 below compares the different reaction conditions for varying methods of synthesis for each compound in the $La_{n+1}Ni_nO_{3n+1}$ [$(LnO)(LnNiO_3)_n$] series (where n = 1, 2 and 3).

Table 1.1. Synthesis conditions for the $La_{n+1}Ni_nO_{3n+1}$ series reported in the literature (where n = 1, 2, and 3).

n	Method	Heat-Treatment Temperature / K	Time / hours	Grinding Required	Impurities	Notes	Ref.
1	Heat & grind	1470	24	y	n	—	1
1	Heat & Grind	1623	4	y	y	a	2
1	Heat & Grind	1123 – 1373	20 × 3	y	n	b	3
1	Sol-gel	1623	4	n	n		4
1	CHFS	1273	6	n	n	f	5
2	Heat & Grind	1420	10	y	n	—	1
2	Heat & Grind	1423 – 1473	96 – 120	y	n	c	6
2	Heat & Grind	1423	192	y	y	—	8
2	Heat & Grind	1373	48	y	y	a	2
2	Sol-gel	1373	70	n	n	d	3
2	Sol-gel	1373	48	n	n		4
2	CHFS	1423	12	n	n	f	5
3	Heat & Grind	1373	96 – 120	y	n	c	7
3	Heat & Grind	1273	288	y	y	—	8
3	Heat & Grind	1323	144	y	y	a	2
3	Sol-gel	1373	70	n	n	d	3
3	Sol-gel	1323	144	y	n	—	4
3	Coprecipitation	1350	5	n	n	e	1
3	CHFS	1348	6	n	n	f	5

Notes:

[a] Before the reaction, the starting materials were fired at 973 K and had been milled for 48 hours.

[b] Heated for 20 hours at each of three temperatures between 1123 and 1373 K.

[c] Precursors were preheated at 1273 K and dissolved in nitric acid.

[d] Oxides were dissolved in nitric acid and converted to nitrates or citrates prior to heat-treatment.

[e] Nitrates added to con. NaOH with bubbling Cl^- gas. The resulting precipitate was then heat-treated.

[f] CHFS indicates that the precursors were synthesised by CHFS then heat-treated.

References:

[1] (Mohan Ram et al. 1986); [2] (Takahashi et al. 2010); [3] (Voronin et al. 2001); [4] (Amow et al. 2006b); [5] (Weng et al. 2008); [6] (Zhang et al. 1994); [7] (Zhang et al. 1995); [8] (Ling et al. 1999).

From table 1.1 it is clear that there are a number of different routes to form $La_{n+1}Ni_nO_{3n+1}$ compounds, the heat and grind approaches taking the longest, up to many days in some cases with multiple regrinding stages required. Often after these long heat-treatments some impurity phases are still observed. These phases are mainly NiO and $La_2NiO_{4+\delta}$ and represent an incomplete reaction. By forming

precursors from aqueous solutions it is possible to reduce synthesis times to a matter of hours and often without regrinding stages (as shown by a reduction from 400 hours using heat and grind, to just 6 hours using a direct reaction of CHFS coprecipitates).(Weng et al. 2008; Zhang et al. 1995)

Electronic conduction occurs through the Ni-O bonds orthogonal to the basal plane and increases through the series $La_2NiO_{4+\delta}$ < $La_3Ni_2O_{7-\delta}$ < $La_4Ni_3O_{10-\delta}$.(Zhang et al. 1994; Zhang et al. 1995) $La_2NiO_{4+\delta}$ is a semiconductor at room temperature with a conductivity of *ca.* 60 $S.cm^{-1}$ at 923 K (approximate IT-SOFC operating temperature). Both $La_3Ni_2O_{7-\delta}$ and $La_4Ni_3O_{10-\delta}$ are metallic conductors at room temperature and have conductivities at 923 K of *ca.* 70 $S.cm^{-1}$ and 100 $S.cm^{-1}$, respectively as shown in figure 1.8.(Amow et al. 2006b)

Figure 1.8. Electrical conductivity *vs.* temperature for $La_2NiO_{4.15}$, $La_3Ni_2O_{6.95}$ and $La_4Ni_3O_{9.78}$. Figure adapted from (Amow et al. 2006b).

The measurements reported in figure 1.8 were made with pellets of 85 % maximum theoretical density for $La_2NiO_{4+\delta}$ and *ca.* 58 % maximum theoretical density for both $La_3Ni_2O_{7-\delta}$ and $La_4Ni_3O_{10-\delta}$. This density is the highest reported for these two compounds, however as they are not fully dense, their 'true' conductivities therefore are most likely to be greater than the values reported.

The effect of the increase in conductivity through the series is proportional to the increase in Ni^{3+} content as *n* becomes greater, however, the compound $LaSrNiO_4$,

in which the Ni is in a 3+ state does not have a greater conductivity than $La_4Ni_3O_{10-\delta}$ where the average Ni valence is 2.67.(Mohan Ram et al. 1986) It could be implied therefore that the differences in conductivity were associated with an increase in perovskite layers.(Mohan Ram et al. 1986) Greenblatt *et al.* report that as the number of Ni-O bonds in the *c* plane increases with *n*, the expected increase in the *c* cell length due to multiplication of the standard Ni-O bond length is not produced.(Zhang et al. 1995) This was attributed to hybridisation of the Ni 3d and O 2p orbital increasing electron delocalisation in the *c* direction.(Zhang et al. 1995) The Ni 3*d* and O 2*p* hybridisation increased along the crystallographic (001) direction with increasing Ni (greater *n*) valence resulting in greater Ni-O-Ni orbital overlap, as shown in figure 1.9. This increase in electronic coordination results in electrons delocalising in the conduction band and causing the $n = 2$ and $n = 3$ compounds to display metallic-type conductivity.(Zhang et al. 1995)

Figure 1.9. Band structure diagrams for $La_2NiO_{4+\delta}$, $La_3Ni_2O_{7-\delta}$, $La_4Ni_3O_{10-\delta}$ and $LaNiO_3$ near the Fermi energy, E_f. Figure adapted from (Sreedhar et al. 1994).

A decrease in the ionic radius of the B site cation causes structural distortions from the ideal perovskite structure in the NiO_6 octahedra.(Zhang et al. 1995) The

effect therefore of doping the B-site of the Ruddlesden-Popper phases is to alter the Ni 3*d* and O 2*p* orbital overlap, resulting in an alteration of the conductivity. This was demonstrated by Amow *et al.* who synthesised the compounds $La_4Ni_{3-x}Co_xO_{10-\delta}$ (where $x = 0.0 – 3.0$, and $\Delta x = 0.2$) and showed that the conductivity decreased with increasing Co^{3+} content, as a result of hole doping the conduction band. This trend was reversed when $x > 2.0$ as a result of band filling due to increased presence of Co^{2+}.(Amow et al. 2006a) There have also been some studies investigating the substitution of Ni by Fe in $La_4Ni_3O_{10-\delta}$.(Carvalho et al. 2009; Kiselev et al. 2007; Tsipis et al. 2007) However no comprehensive characterisation of the electrical conductivity has been conducted on these samples to investigate the effect of the Fe cation on the Ni sites.

Oxygen non-stoichiometry plays a large part in the properties of the $La_{n+1}Ni_nO_{3n+1\pm\delta}$ series. The $n = 1$ compound is hyperstoichiometric and the $n = 2$ and $n = 3$ compounds are hypostoichiometric.(Bannikov et al. 2006) In both the $n = 2$ and $n = 3$ compounds an increase in oxygen content, δ, was observed with increasing temperature.(Bannikov et al. 2006) Kharton *et al.* found that in $La_2NiO_{4+\delta}$ there were two oxygen transport mechanisms, the first being oxygen interstitial migration through the LaO rocksalt layers. The second being oxygen diffusion through vacancies in the $LaNiO_3$ perovskite layers.(Kharton et al. 2001)

1.3. Overview of Solid-Solid Reactions

Using traditional solid-state techniques, layered metal oxides can be produced as thermodynamic compounds at temperatures of c*a.* 1273 K with comminution stages being required to complete mass transfer in reactions. The formation of these compounds occurs with little knowledge of the mechanism or insight into the nature of reaction intermediates. The rate of reaction is often limited by the velocity of solid-state diffusion, with the energy required for diffusion usually meaning that high-temperatures and long reaction times are required. As a result, many thermodynamically stable phases are inaccessible or decompose due to the high-energies required for diffusion.(Stein et al. 1993) The consequence of slow diffusion is that discovery of new polycrystalline heterometallic compounds is often slow and laborious or not possible via conventional routes. Faster reaction rates and some control over the reaction mechanism and the resulting product can be achieved by

utilising precursors which have inherently shorter diffusion distances such as using aqueous or intimately mixed precursors. By doing this, the rate limiting step for the reaction becomes nucleation of the new crystallites, which is a considerably faster process.(Novet et al. 1991)

1.3.1. Kinetic Description of Solid-Solid Reactions

Diffusion between two substances can be described by Fick's laws of the diffusion. The first law can be written as:

$$J = -D\frac{dc}{dx} \qquad \textbf{(1.5)}$$

Where J = the flux of matter (mol.m^{-2}.s^{-1}), D = diffusion coefficient (m^2.s^{-1}), c = concentration per unit area (mol.m^{-3}), and x = the length (m). Fick's first law describes that the particle flux, J, is proportional to the concentration gradient, and matter therefore travels from high to low concentration. Fick's second law can be written as:

$$\frac{\partial c}{\partial t} = D\frac{\partial^2 c}{\partial x^2} \qquad \textbf{(1.6)}$$

Where c = concentration per unit area (mol.m^{-3}), x = diffusion distance (m), t = time (s), D = diffusion coefficient (m^2.s^{-1}). Fick's second law relates the change in concentration over time to the concentration gradient. It shows that the rate of the change of concentration is proportional to the concentration with respect to distance. Fick's laws can therefore be used to describe diffusion of metal ions between two solids.

The diffusion couple between two solids was described by Wagner,(Wagner 1969) one-dimensional diffusion between two solids is described in terms of the relationship between the velocity of the reactants, ν_n, and their molar fluxes, J_n, through equations 1.7 and 1.8, where subscript 1 and 2 relate to reactant 1 and 2 respectively.

$$\nu_1 = \frac{J_1}{\left(N_1 / V_m\right)} \quad \textbf{(1.7)}$$

$$\nu_2 = \frac{J_2}{\left(N_2 / V_m\right)} \quad \textbf{(1.8)}$$

V_m = molar volume an N_n = mole fraction of component n. These velocities are dependant on the position of the interface between the two reactants. ν_1 - ν_2 is invariant, therefore it was an appropriate basis for a diffusion coefficient, D.(Wagner 1969)

Both velocities ν_1 and ν_2 are proportional to N_2 over diffusion distance x, giving equation 1.9:

$$\frac{\nu_1 - \nu_2}{N_2 / \partial x} \quad \textbf{(1.9)}$$

In order to obtain a diffusion coefficient that can be related to Fick's law of diffusion Wagner multiplies by N_1N_2 to give equation 1.10:

$$D = \frac{N_1 N_2 \left(\nu_1 - \nu_2\right)}{\partial N_2 / \partial x} = \frac{V_m \left(N_2 J_1 - N_1 J_2\right)}{\partial N_2 / \partial x} \quad \textbf{(1.10)}$$

The relationship between the diffusion velocity and molar flux has been shown experimentally using interdiffusion reactions of Ni/Zr diffusion couples, finding that an amorphous NiZr compound is formed that grows to a critical thickness, before the nucleation of an ordered solid occurs. The amorphous layer shrinks leaving a single layer of ordered solid between the two reactants.(Gösele et al. 1989) This is shown schematically in figure 1.10.

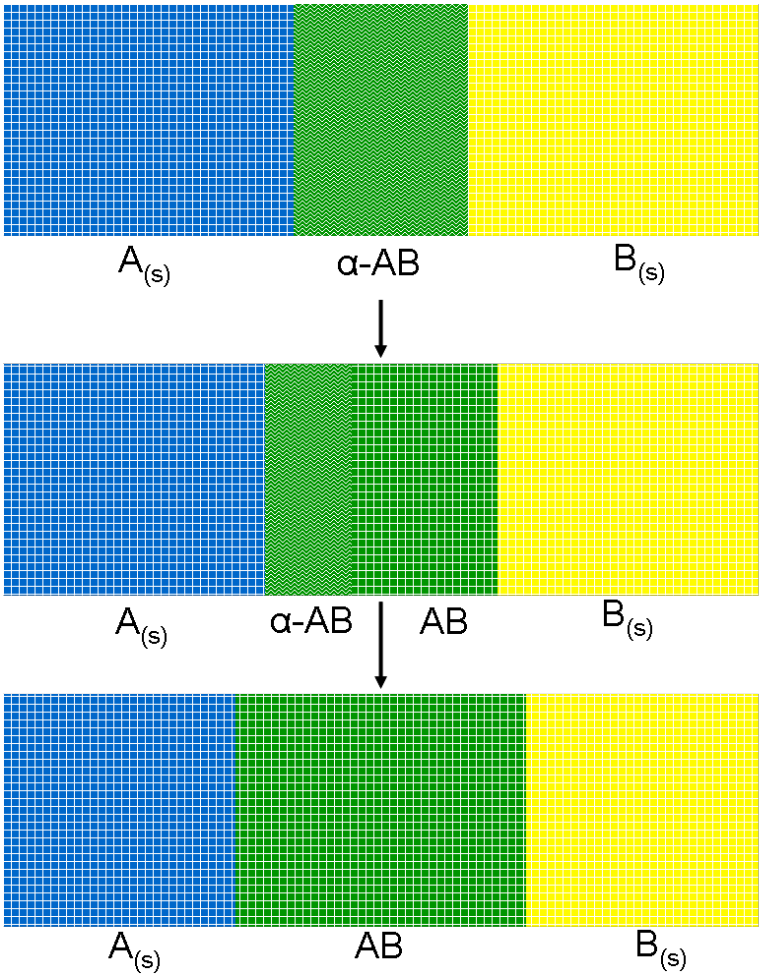

Figure 1.10. Diagram to show the formation of an amorphous layer, α-AB, between two reactant layers, A and B (top). As the critical length of the amorphous phase is reached, nucleation of a crystalline phase AB occurs (middle). Diffusion continues between A and B to form the crystalline phase AB (bottom).

The formation of the ordered AB nucleus is dictated by two competing timescales. The first timescale, τ_{int}, is the time taken for the atoms to rearrange to form the target nucleus AB, at each given interface. The length of the interface is L and diffusion velocity of A through α-AB or B through α-AB is υ_{int}. Then the interface timescale is given by equation 1.11:

$$\tau_{int} = \frac{L}{\upsilon_{int}} \qquad \textbf{(1.11)}$$

In this timescale τ_{int}, the amorphous layer grows a distance of L. The second timescale that of nucleation of the ordered AB phase is given by equation 1.12:

$$\tau_{nuc} = \left\{ k \exp\left(-\frac{\Delta G^* + Q}{k_B T} \right) \right\}^{-1} \quad \textbf{(1.12)}$$

Where, k is the rate constant, Q is the activation energy for diffusion through the interface and ΔG^* is the barrier to nucleation of the AB phase. The inequality between the two timescales dictates if α-AB can continue to grow, which occurs when equation 1.13 is true:

$$\tau_{\text{int}} \leq \tau_{nuc} \qquad \textbf{(1.13)}$$

The lower critical velocity of A or B travelling over the interface is therefore:

$$v_{\text{int}} \geq \frac{L}{\tau_{nuc}} \qquad \textbf{(1.14)}$$

Below this value of υ_{int} the nucleation of AB is favoured to the growth of the α-AB layer. (Meng et al. 1988) This work showed that by reducing the layer thickness, the time taken for the ordered AB phase to form at the interface, τ_{int} is reduced. Equation 1.13 shows that if $\tau_{int} \geq \tau_{nuc}$, the rate of formation of the nucleus AB will be greater, therefore increasing the rate of the solid-state diffusion. The experimental kinetics of the reaction would also depend on crystal imperfections such as dislocations, grain boundaries and internal surfaces.(Frischat 1974)

The effect of a reduced diffusion distance on the reaction and diffusion mechanism has been described by Novet *et al.* When using ultrathin (*ca.* 2 – 5 nm) layers of alternating Fe and Si, the elements diffused to the interfaces where an amorphous intermediate was formed that contained a concentration gradient. At this point interfaces no longer existed and the diffusion stage was complete. Once the interfaces were removed, nucleation of the ordered product became the rate limiting step (an inherently faster process). As the concentration gradient began to decrease, structures with short-range order in the amorphous intermediate started to form that could act as nucleation sites for the new crystallite.(Novet et al. 1992) This process is described schematically in figure 1.11.

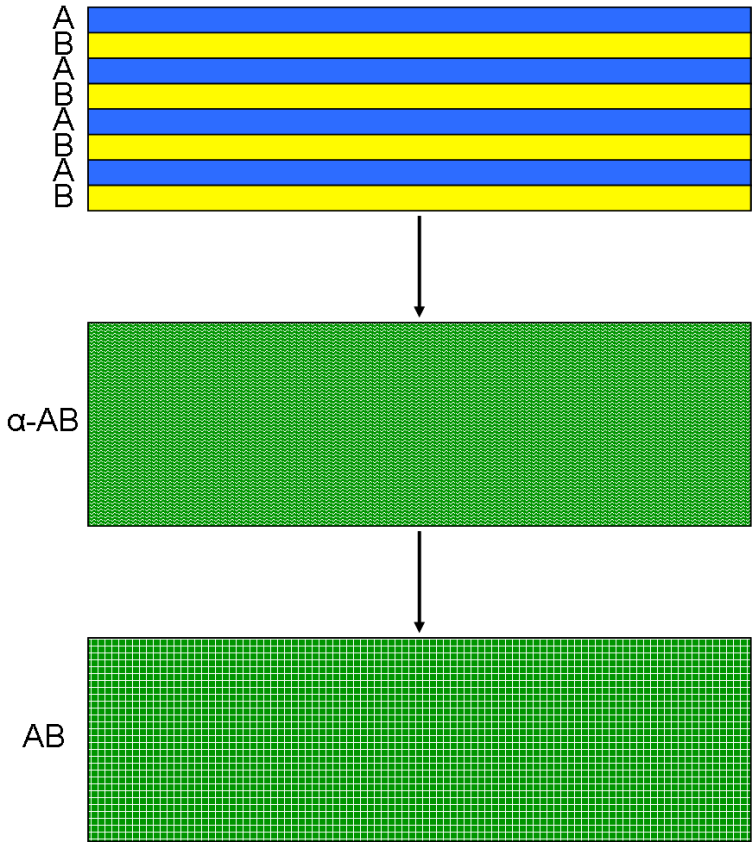

Figure 1.11. The mechanism of diffusion between thin layers of two solids. Applied heat or pressure causes diffusion to occur in ultra-thin layers of two reactants, A and B (top). Interfacial diffusion is completed relatively quickly, forming an amorphous intermediate (middle). Nucleation of the crystalline solid AB is then the rate limiting step (bottom).

The diffusion reaction between La_2O_3 and CoO to form the perovskite $LaCoO_{3-\delta}$ and the Ruddlesden-Popper type layered oxide La_2CoO_4, both of which are similar to the phases in this thesis, has been investigated by Palcut *et al.*(Palcut et al. 2007) The diffusion behaviour of the reactants was investigated using a Pt tracer experiment. Pt markers were used to indicate the position of the interface as the reaction proceeded as shown in figure 1.12.

Figure 1.12. Schematic diagram and SEM image of the La_2O_3-CoO diffusion couple. The small circles indicate the Pt markers. Phases are indicated by: 1 = La_2O_3, 2 = CoO and 3 = $LaCoO_3$. Figure adapted from (Palcut et al. 2007)

Figure 1.12 shows the position of the Pt markers and that growth of the $LaCoO_{3-\delta}$ layer occurred at the $La_2O_3/LaCoO_{3-\delta}$ interface. Co^{3+} must therefore have diffused through the product layer to the $La_2O_3/LaCoO_{3-\delta}$ interface. This result suggested that diffusion of Co^{3+} is greater than diffusion of La^{3+}, $D_{Co}>>D_{La}$ and occurred through a vacancy mechanism.(Palcut et al. 2007) Palcut *et al.* determined that a parabolic increase in the rate constant was proportional to the partial pressure of oxygen pO_2 and to the number of cobalt vacancies.(Palcut et al. 2007) The formation of La_2CoO_4 was also found to be diffusion based and occurred through a Co vacancy mechanism. The reaction rate was similar to the formation of $LaCoO_{3-\delta}$.(Palcut et al. 2007)

In summary when diffusion distances were long, an interfacial amorphous layer was formed, and then nucleation of a crystallite occurred at the same interface.

Both phases were then competition and the crystalline phase continued to grow as diffusion progresses until the reactants were consumed, as shown in figure 1.10. When diffusion distances were shorter, interfacial diffusion was completed relatively quickly, and an amorphous intermediate was formed, at which point nucleation of the crystalline phase became the rate limiting step.

1.4. Overview of the Synthesis of Layered Heterometallic Oxides

The synthesis of heterometallic oxides in the solid-state can be achieved through the reaction of stoichiometric mixtures of metal precursors with the addition of energy (which aids diffusion) that can come from a change in conditions such as temperature or pressure. Due to the slow rate of diffusion between two solids, large amounts of energy are often required to obtain a thermodynamic product. As described above in section 1.3, the chemistry that occurs between solid reactants is largely governed by the diffusion between them. The diffusion distances between two solids can be reduced by altering the physical properties of the reactants, such as: size, morphology, crystallinity, and intimacy of mixing. In doing this, the energy required for the subsequent transformation can be reduced. This was shown experimentally by Fister *et al.* who artificially reduced diffusion distances by layering ultrathin films of Se and Mo and found that the reactants diffused initially to form an amorphous alloy before crystallising to form $MoSe_2$.(Fister et al. 1992) This route differs from that between particles or layers of longer length scale described by Gösele *et al.*, in which an amorphous layer was formed initially between the two reactants. Subsequently a crystalline phase nucleated and competed with the amorphous phase until just the crystalline product phase remained at the interface as shown in figure 1.10.(Gösele et al. 1989) There are a number of techniques that are used in laboratories to synthesise the complex layered heterometallic oxides which are the subject of this thesis, the ones most widely used are described below.

1.4.1 Solid precursor route

Traditional solid-state synthesis involves the reaction of a stoichiometric mixture of solid micron-sized metal oxide precursors to form the required compound. The metal oxide precursors are mixed, milled to decrease particle size, and then calcined at high-temperature. The milling and calcining procedure must be repeated often in order to complete the reactions due to the large energy barrier to diffusion. Frequent milling increases the reaction speed by presenting more unreacted surfaces to each other. Due to the high-temperatures required, decomposition products are often observed as well as undesirable by-products, also syntheses are often long and a high energy cost is required to reach completion. However the solid precursor route is versatile, a large range of chemistries are available and highly crystalline compounds can be formed. Ruddlesden-Popper type lanthanum nickelate compounds have been made extensively using this type of processing. $La_4Ni_3O_{10-\delta}$ was made from a 4 – 5 day heat treatment of La_2O_3 and NiO at 1373 K with 2 – 3 intermediate regrinding stages.(Zhang et al. 1995) The synthesis of $La_4Ni_3O_{10-\delta}$ was also repeated by Ling *et al.* who reacted the stoichiometric mixture of La_2O_3 and NiO at 1273 K overnight and reground for 30 minutes, then reacted for 2 days at 1273 K and reground for 10 minutes, this process had to be repeated 12 times in order to complete mass transfer and obtain phase pure material.(Ling et al. 1999)

1.4.2. Mechanochemical Reactions

Mechanochemical routes to complex oxides use high-energy milling to grind simple metal oxides to bring about chemical change.(Zhang 2004) During the milling process the homogeneity of the oxide mixture is increased by fragmentation of the particles, as this occurs new unreacted surfaces constantly come into contact. The fragmentation leads to the formation of high defect densities at the surfaces of the particles. Nucleation of a new crystalline phase occurs at particle-particle interfaces after sufficient activation. If no crystalline phase has been formed, amorphisation can occur.(Zhang 2004) The amorphous phase is intimately mixed and if calcined can lead to fast reaction times at low temperatures due to short diffusion distances. However the complete process is very high energy due to the long milling times required prior to heat-treatment and contamination of the sample can occur.

Using mechanochemical synthesis it has been possible to isolate Ruddlesden-Popper type metal oxide $Sr_3Ti_2O_7$, where it was found that mechanochemical activation of SrO and TiO_2 leads to an increased defect concentration and subsequently a higher internal energy in the oxides. This shortened diffusion distances and meant that the temperature of the final calcination step could be reduced by 450 K.(Hungría et al. 2002)

1.4.3. Coprecipitation

When making heterogeneous metal oxides the aim of a coprecipitation reaction is to form a homogeneous mixture of metal precursors. This mixture can then be calcined to bring about solid state transformations without the need for grinding. When performing a coprecipitation reaction for this purpose, control of reaction conditions such as: reactant concentration, pH and temperature is important to ensure complete precipitation of all metals and to obtain an intimate mixture with the correct stoichiometry. The coprecipitation of metal oxides can be performed at room temperature using a base such as NaOH or KOH to precipitate directly from a metal salt solution. The products which are usually amorphous often need to be heat-treated to form metal oxides or solid solutions.(Cushing et al. 2004)

Coprecipitation has been used as a preliminary technique to form intimate mixtures of metal oxides in order to reduce diffusion distances between reactants and subsequently the energy barrier to reaction. This was shown clearly by Zhu *et al.* who synthesise $CaCu_3Ti_4O_{12}$ from a coprecipitate at 973 K in 1 hour, in comparison to 1273 K for 20 hours when using a traditional solid-state synthesis.(Zhu et al. 2009)

1.4.4. Sol-Gel

The sol-gel process is a multi-stage process which begins by forming a sol from colloidal metal particles in water. The colloidal particles interact through polycondensation reactions until a network is formed. The solution is left to age for a period of hours or days to allow the polycondensation reactions continue and form a gel. The gel is then dried to form an aerogel, which is densified at high temperature to form an intimate mixture of metal oxide particles.(Gopalakrishnan 1995; Hench et al. 1990) The main advantage of using sol-gel chemistry is that complex

compositions can be formed due to the good homogeneity of the metal mixture that is achieved by initially mixing the precursors in solution.

The Pechini method is a widely used form of sol-gel reaction which varies in that the initial metal-chelates are formed using a complexing agent such as citric acid, and then a polyalcohol such a ethylene glycol is added, in order to link the chelates the polyesterification reaction subsequently occurs to form the gel.(Cushing et al. 2004)

Sol-gel and Pechini reactions have been used in the synthesis of polycrystalline complex heterogeneous layered metal oxides, such as lanthanum nickelates and their doped derivatives.(Amow et al. 2006a; Poltavets et al. 2006). In these studies, an intimate mixture of metal oxides are formed in the sol-gel process, which are then further heat-treatment to bring about the final solid-state transformation.

1.4.5. Molten Salt Flux Synthesis

Molten-salt fluxes have been primarily used for the synthesis of heterometallic chalcogenides at intermediate temperatures of 473 – 773 K.(Kanatzidis 1997) By using a molten-salt mixture, the reactants are mixed in the liquid phase and therefore at an atomic level to ultimately reduce diffusion distances.(Gopalakrishnan 1995) This method has been extended to the synthesis of complex layered metal oxides by reacting simple metal oxide precursors in an alkali hydroxide that melts at temperatures between 473 – 773 K, for example KOH and NaOH. $La_{1-x}M_xCuO_4$ (where M = K, Na) has been synthesised by melting a KOH and NaOH mixture at 573 K, which is made acidic by careful control of the water content. Stoichiometric amounts of La_2O_3 and CuO were then added and dissolved. The melt was kept at 573 K for 100 hours, resulting in a slow loss of water and gradual increase in pH, as a result, $La_{1-x}M_xCuO_4$was collected as a precipitate.(Ham et al. 1988) This technique has also been used to synthesise layered oxides such as $Bi_5Ti_3FeO_{15}$ and $LaBi_4Ti_3FeO_{15}$ from a N_2SO_4/K_2SO_4 molten salt flux.(Porob et al. 2006) As a result of decreased diffusion distances afforded by this technique, both phases could be formed in 1 hour at 1073 – 1173 K, when they would normally take 2 – 4 days by traditional solid-state heating and grinding at temperatures greater than 1273 K.

1.4.6. Physical Vapour Deposition

Physical vapour deposition (PVD) uses a physical process to convert particles into a gaseous state whereupon they can be deposited as thin films on a target.(Reichelt et al. 1990) In particular two forms of PVD, molecular beam epitaxy (MBE) and pulsed laser deposition (PLD) can be used to synthesise layered compounds on a layer by layer basis, and in doing so access metastable states.

1.4.6.1. Molecular Beam Epitaxy

Molecular beam epitaxy (MBE) is a method of MBE in which epitaxial thin films can be grown on a crystalline substrate from molecular beams.(Joyce et al. 2004) The molecular beam is formed in a Knudson cell which is a heated evaporator. By using a molecular beam it is possible to obtain layer by layer control over the deposition, and as such MBE has been used to form layered compounds. For example the formation of $LaFeO_3$-$LaCrO_3$ superlattices, in which $LaFeO_3$ and $LaCrO_3$ were deposited layer by layer onto a $SrTiO_3$ single crystal target.(Ueda et al. 1998) By using this method, a lattice was formed that was not thermodynamically stable when made using a more traditional method.(Ueda et al. 1998) Also the Ruddlesden-Popper type structure $Sr_{n+1}Ti_nO_{3n+1}$ (where n = 1, 2, 3, 4 and 5) has been formed using this technique.(Haeni et al. 2001)

1.4.6.2. Pulsed Laser Deposition

Pulsed Laser Deposition (PLD) is a related method to MBE in which a pulsed laser is used to excite molecules into a gaseous state whereupon they can be deposited onto a target. Similarly to MBE it is possible to obtain layer by layer control of the deposition to form layered metal oxides. This method has been used to form the Ruddlesden-Popper type compound $Ca_{n+1}Mn_nO_{3n+1}$ series, (where n = 1, 2, 3, 4, 5, and 6) the n = 4, 5, and 6 compounds all being unobtainable by other methods.(Yan et al. 2007)

1.4.7. Continuous Hydrothermal Flow Synthesis

Continuous hydrothermal flow synthesis (CHFS) utilises a continuous flow of supercritical or subcritical water to precipitate metal oxides and hydroxides from the respective aqueous metal salts in flow. The precipitates formed can then be

cooled and collected as a slurry after passing through a back-pressure regulator. A version of CHFS was first developed in the 1990s by the Arai group in Japan who managed to synthesise a range of simple nanosized metal oxides.(Adschiri et al. 1992) CHFS utilises the properties of supercritical water in order to produce well-dispersed nanosized metal oxides and hydroxides in seconds.

1.4.7.1. Properties of Supercritical Water

A fluid is considered supercritical when it raises above its critical temperature (T_c) and critical pressure (P_c), the critical point of water is 647.1 K, and 22.1 MPa.(Weingärtner et al. 2005) As water approaches its critical point, a number of changes occur. The phase diagram of water is presented in figure 1.13 below.

Figure 1.13. The phase diagram of water, TP = triple point solid-liquid-gas phase boundary. CP = critical point at liquid gas interface. Figure adapted from (Weingärtner et al. 2005).

The density of water is about 1000 $kg.m^{-3}$ under ambient conditions, this falls to 712 $kg.m^{-3}$ at 573 K following a saturation curve (the curve by which the pressure is just great enough to maintain the liquid state). At the critical point the density drops further to 322 $kg.m^{-3}$.

Figure 1.14. Variation in the dielectric constant of water with pressure and temperature. Figure adapted from (Fukushima 2000).

The dielectric constant is a dimensionless constant that is used to demonstrate the polarity of a solvent. The dielectric constant of water decreases from 80 at ambient conditions to 33 at 483 K (similar to methanol), and then to 5 at the critical point (similar to ethyl acetate). This value can fall further to 2 at 773 K (similar to hexane), meaning that water becomes a non-polar solvent when in the supercritical state. The implication of the changing dielectric constant and the density is that when polar inorganic salts are mixed with supercritical water they are far less soluble than when in water at ambient temperature and pressure. This property results in supersaturation of the dissolved metal salts when in supercritical water. When producing nanoparticles the key factor is to increase nucleation rates, this can be achieved through supersaturation. Supersaturation is the ratio of the concentration of the species in a solution to the saturation concentration, therefore the lower the saturation concentration, the greater the supersaturation will be. By mixing metal salt solutions with a flow of scH_2O, supersaturation can be very large resulting in high nucleation rates.

A further change is in the behaviour of ions, which is very different in scH_2O than in water at ambient conditions. This behaviour can be described in terms of the

ionic product, *K*, which is the product of the concentrations of the dissociated H^+ and OH^- ions and is given by equation 1.16 and is described schematically in figure 1.15.

Figure 1.15. Ionic product logK *vs.* temperature of water at various pressures between 10 and 100 MPa. Figure adapted from (Fukushima 2000).

In H_2O at ambient temperature and pressure the ionic product is 10^{-14} $mol^2.dm^{-6}$, at 573 K a maximum of 10^{-11} $mol^2.dm^{-6}$ is reached. This equates to a 30 times increase in the concentration of both H^+ and OH^- in solution, and means that near-critical water can be both strongly acidic and alkaline. At the critical point a rapid change is observed as is highlighted in figure 1.15, meaning the ionic product of supercritical water can be finely tuned using variations in temperature and pressure. The resulting effect is that supercritical water is both strongly hydrolysing and strongly dehydrating. This leads to the formation of metal oxides through equations 1.17 and 1.18:

$$M(NO_3)_{x(aq)} + xH_2O \rightarrow M(OH)_x + xHNO_3 \quad \textbf{(1.17)}$$

$$M(OH)_x \rightarrow M(O)_{x/2} + x/2H_2O \quad \textbf{(1.18)}$$

In summary, when metal salts under ambient conditions are exposed to near or supercritical water conditions, the many changes in properties of water are favourable for rapid hydrolysis of the metal salts to hydroxides, subsequent dehydration to oxides and rapid precipitation (in seconds) and/or crystallisation of well defined nanomaterials.

1.4.7.2. Continuous Hydrothermal Flow Synthesis

Continuous hydrothermal flow synthesis is a method of producing metal oxides or hydroxides in a continuous flow of supercritical water. A schematic diagram of the standard CHFS equipment in use at UCL is presented in figure 1.16.

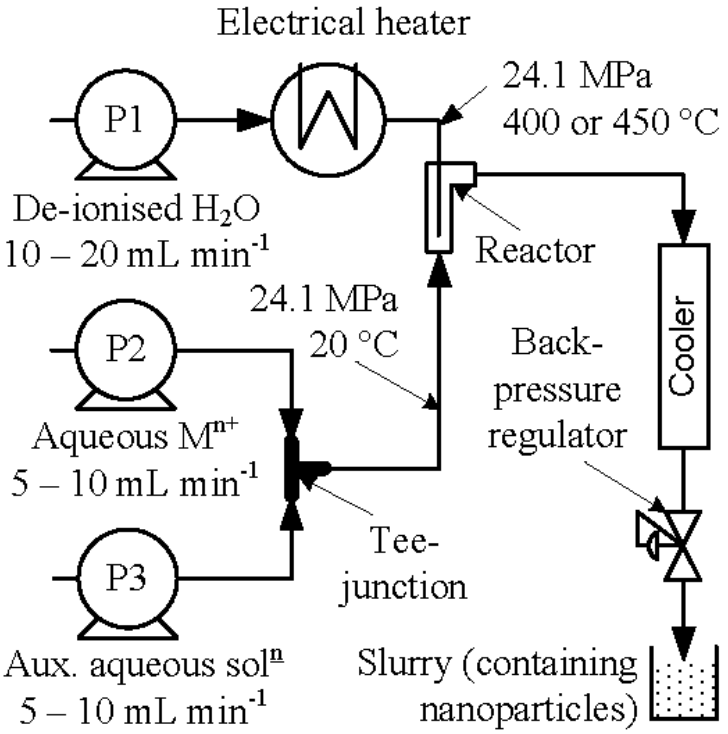

Figure 1.16. A schematic diagram of the CHFS process. P = HPLC pump.

In this system a continuous feed of metal salt solution is mixed in flow with a stream of supercritical water at 723 K at 24.1 MPa. The equipment was set up with three HPLC pumps. The water feed (pump 1 in figure 1.16) is pumped into a heater to heat the water to 723 K. The precursor feed (pump 2 in figure 1.16) was made up of an aqueous solution of various dissolved metal nitrate salts, whilst auxiliary solutions such as base (KOH) or a reducing agent such as hydrogen peroxide could be delivered by pump 3. The metal salt and auxiliary flows premixed in a T-piece mixer after which they met the flow of scH_2O at 723 K and 24.1 MPa from pump 1.

Rapid precipitation (in fractions of a second) of metal oxides or hydroxides then took place through the simultaneous hydrolysis and dehydration reactions described in section 1.4.7.1. The resulting slurry subsequently cooled in-line and passed through a back-pressure regulator, (which was used to maintain pressure) to be collected. The collected slurries were washed and freeze dried to produce a dry powder.

In this process, independent reaction parameters, such as: pH, metal salt concentration, pressure and temperature can be varied to maintain control of particle properties.(Darr et al. 1999) Hakuta *et al.* found that the particle size of γ-AlO(OH) could be controlled between *ca.* 70 and 300 nm by varying the reaction pH.(Hakuta et al. 2005) In the same work they also found that particle size of the same material could be further modified between *ca.* 170 and 300 nm by changing the reaction pressure.(Hakuta et al. 2005) Adschiri *et al.* found that control of morphology was possible through manipulation of the reaction temperature and pressure.(Adschiri et al. 2000)

The mixing geometry was important to ensure homogeneous mixing and prevent blockages or build up of pressure. The geometry was developed in-house jointly by Prof. J Darr, Dr. Chris Tighe and Robert Gruar and was a confined jet mixer which is shown in figure 1.17.

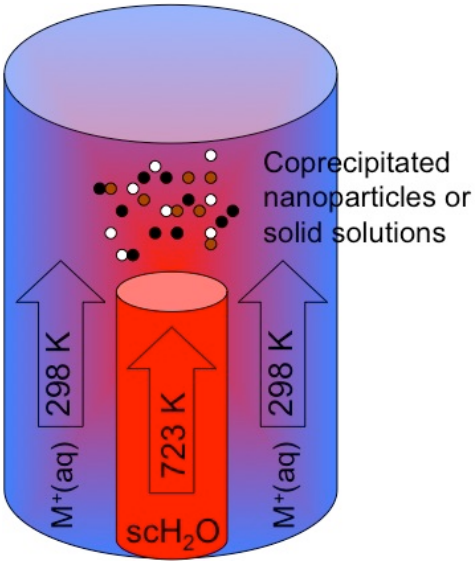

Figure 1.17. Schematic diagram of the mixing zone within the reactor.

In the confined jet mixer, the flow of scH_2O entered the mixer through a central pipe at 723 K, as the flow entered the larger mixing zone a jet of scH_2O was formed. The stoichiometric mixture of aqueous metal salts entered the mixing zone

at room temperature around the scH_2O pipe and was mixed with the scH_2O in the jet. Mixing this way ensured good mixing and also ensured that the conditions in the mixing zone, which were 657 K and 24.1 MPa, were above the critical point of water.

1.4.7.3. Materials Synthesised Using CHFS

CHFS has been mainly used to synthesise nanosized metal oxides and hydroxides. The resulting products often display high-surface areas and nano-crystallite sizes, with a small particle size distribution.(Kellici et al. 2010; Zhang et al. 2009) When first used by Adschiri *et al.*, simple Fe, Co, Ni, Zi and Ti oxides were synthesised and the effect of varying the reaction conditions on the resulting properties was investigated.(Adschiri et al. 1992)

In the right conditions, solid solutions can form directly, e.g. $Ce_{1-x}Zn_xO_2$ solid solutions were formed and showed extended phase boundaries from that previously reported.(Kellici et al. 2010) A high-throughput synthesis adaptation was used to make 66 solid solutions of $Ce_xZr_yY_zO_2$ that again showed extended phase boundaries.(Weng et al. 2009). The synthesis of bioceramics such as hydroxyapatite, $[Ca_{10}(PO_4)_6(OH)_2]$, an artificial bone material has also been successful. The nanosized compound was successfully synthesised without the usually required long ageing step.(Chaudhry et al. 2006) Energy materials such as Ni-YSZ (yttria stabilised zirconia) cermets for solid oxide fuel cells,(Weng et al. 2010) and $LiFePO_4$ a cathode materials in lithium ion batteries have also been synthesised directly.(Xu et al. 2008)

With respect to the synthesis of complex metal oxides CHFS has been used as a method of coprecipitation to produce intimately mixed metal oxides and hydroxides in stoichiometric amounts that can then be used as precursors for solid-state reactions. By doing this, solid-solid diffusion distances could be reduced for the subsequent solid-state reaction thereby lowering the energy barrier to conversion and removing the requirement for comminution stages. For example high-surface area La_2CuO_4 was synthesised at 873 K in 5 hours,(Galkin et al. 2000) rather than 12 hours at 1273 – 1473 K required when performing a conventional solid state synthesis.(Doshi et al. 1993) When produced using CHFS, this material had a considerably greater surface area, and hence showed a catalytic improvement in the reduction of CO compared to the same material made using a heat and grind

approach.(Galkin et al. 2000) Lanthanum nickelates, which are the subject of this thesis, have also been synthesised in a similar manner. By coprecipitating an intimate mixture of La_2O_3 and NiO in the correct stoichiometry, it was possible to reduce the synthesis time for $La_4Ni_3O_{10-\delta}$ from 96 – 120 hours (when made via traditional solid-state technique)(Zhang et al. 1995) to just 6 hours without the need for any intermittent grinding.(Weng et al. 2008)

1.5. High-Throughput Materials Discovery

High-throughput and combinatorial chemical synthesis methods have been in development for a number of years, particularly in the field of organic chemistry and drug discovery where large searches are performed to find new lead structures.(Balkenhohl et al. 1996; Drews 2000) Combinatorial methods in inorganic and materials science are however lagging behind. Some combinatorial adaptations have been made to a number of inorganic materials synthesis techniques,(Choi et al. 2010; Ding et al. 2009; Guerin et al. 2006a; Hyett et al. 2007; Klein et al. 1998; Thorne et al. 2010) however, none appear to match the current size and scope achieved in the drug discovery field.

Many of these high-throughput approaches are essentially batch process where *n* amount of samples are synthesised in parallel. For example Klein *et al.* describe a hydrothermal batch reactor with thirty-seven "reaction chambers" that can be filled with individual precursor compositions, shown in figure 1.18.(Klein et al. 1998) This method was used to synthesise a range of titanium containing silicate zeolite structures in microgram quantities, which were screened using X-ray diffraction to obtain information on crystallinity and structural type.(Klein et al. 1998) Ding *et al.* prepared perovskite type ABO_3 compounds using an adapted parallel solution combustion synthesis technique, in which, stoichiometric solutions were metered into microwells in a ceramic reaction plate which was then placed into a furnace and heated to bring about the combustion reaction. In this manner 16 samples were synthesised in parallel, and then tested for their photocatalytic performance.(Ding et al. 2009) Lee *et al.* describe a solid-state method in which manually ground powders were automatically mixed and placed into an eighteen well sample holder. Subsequent reactions could then be performed in parallel.(Lee et al. 2011)

Figure 1.18. Schematic diagram (top) and photograph (bottom) of the 37 well hydrothermal reactor used by Klein *et al.*(Klein et al. 1998)

Perhaps more successful high-throughput methods involve chemical and physical vapour deposition techniques where many hundreds of samples can be synthesised at once over a gradient. Hyett *et al.* used an adapted atmospheric-pressure CVD apparatus that incorporated two separate mixing chambers to mix reactant gas flows. Molar flow rates could be altered to adjust the stoichiometric composition creating a thickness and composition gradient over the substrate, as shown in figure 1.19. The resulting phases could then be investigated using X-ray diffraction mapping.(Hyett et al. 2006) This approach potentially allowed access to over one thousand compounds in a single experiment.(Hyett et al. 2007)

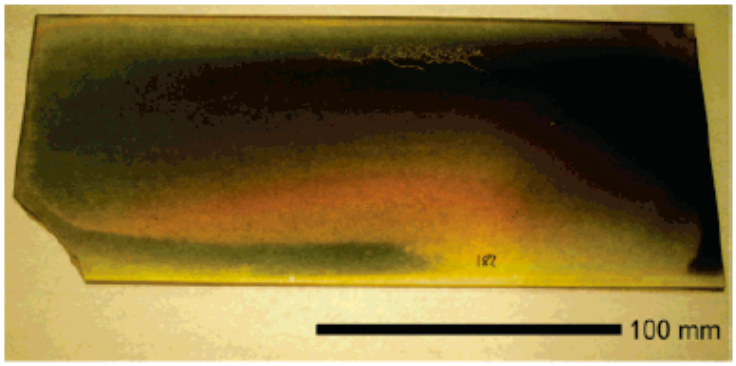

Figure 1.19. Photograph of $Ti_{3-\delta}O_4N$ deposited combinatorially on a glass substrate. The variation in composition and thickness over a substrate is highlighted by the change in colour.

Geurin *et al.* described a method of high-throughput PVD in which mixed metal oxides, hydroxides and nitrides with up to six components could be co-deposited on a target across a large compositional range.(Guerin et al. 2006a) Metals were deposited across compositional gradients in predetermined thicknesses on a silicon substrate, using three electron beams. Control of the deposition was provided by a number of shutters and a variable source temperature.(Guerin et al. 2006a) This method has been used to produce a wide range of materials including PtPdAu alloys,(Guerin et al. 2006b) $Mg_{1-x}Ni_xH_y$ hydrogen storage materials,(Guerin et al. 2008) and $Pb(Zr_{1-x}Ti_x)O_3$ solid solutions.(Anderson et al. 2009)

High-throughput adaptations to other techniques include sol-gel, in which doping reactions of TiO_2 were performed in parallel. (Choi et al. 2010) Also pulsed laser ablation equipment has been adapted to have 30 rotating targets in order to allow high-throughput synthesis capabilities.(Kahn et al. 2010)

An adaptation to CHFS was made called high-throughput continuous hydrothermal, HiTCH, flow synthesis, that was able synthesise a large number of compositions consecutively without contamination between samples. This is achieved by manually operating a switch valve that could divert an additional cleaning water feed into the reaction point between samples in order to clean the mixing point whilst maintaining reaction conditions. A schematic diagram is shown in figure 1.20 below.

Figure 1.20. a) Schematic diagram of the HiTCH flow synthesis equipment. Each metal salt solution was filled into the injector and pumped into the system. Each solution met a flow of 1.0 M KOH solution at a T-piece mixer, marked T. The solution then passed into the mixer whereupon it met a flow of supercritical water (723 K, 22.8 MPa). The resulting slurries were cooled in-line (marked c) and collected at room temperature through a back-pressure regulator. b) Compositions after heat-treatment at 1273 K were placed into a PTFE holder.(Weng et al. 2009)

Using HiTCH flow synthesis stoichiometric compositions with the formula $Ce_xY_yZr_zO_2$, ($x + y + z = 1$) were synthesised that were collected as either solid-solutions or phase mixtures. Sixty-six samples were synthesised in total in just 12 hours.(Weng et al. 2009) The heat-treated (1 hour at 1273 K) samples were screened using high-throughput powder X-ray diffraction at the Diamond Light Source synchrotron, scanning electron microscopy and energy dispersive X-ray spectroscopy in order to gain an insight into the structural changes in the series, which are shown in figure 1.21.

Figure 1.21. a) Representation of compositional space. Each hexagon represents a different sample, the colour is proportional to the molar concentration of Ce (red), Zr (green), and Y (Blue). b) Phase diagram, showing fluorite structure (white), monoclinic ZrO_2 (yellow), tetragonal ZrO_2 (red), bixbyite (blue) and $2 \times 2 \times 2$ oxygen vacancy ordered pseudo fluorite (green). The dots indicate when a binary mixture is present and the stripes show a smooth transition between phases. c) Lattice parameter information. Each value has been calculated from Rietveld refinement of powder diffraction data to a mean volume per $MO_{2-\delta}$ unit. d) Relative crystallite sizes calculated from the Scherrer equation. The diameter of the blue circle indicates the size with respect to each sample.

It is clear from figure 1.21 above that by using HiTCH flow synthesis, a large quantity of structural information from powder X-ray diffraction about the metal oxide tertiary system could be obtained rapidly, and which could then provide information to plan further experiments.(Cockcroft et al. 2011)

1.5.1. Automation of High-Throughput Materials Discovery

Automation has been shown to greatly increase the number of organic compounds that can be screened, particularly in the drug discovery sector. An internet search using Google Scholar of the terms "automated drug discovery" produces 118000 results. A good review of the history of automation and high-throughput techniques in the drug discovery process can be found in Science.(Drews 2000) Conversely due to the long reaction times and the multi-step processes required when forming new heterometallic materials automated materials synthesis methods do not have the same scope. As discussed previously the issue lies in the inhomogeneity of mixing of the precursors, and subsequent long diffusion distances, which occur when using conventional heat and grind synthesis. This results in the need for multiple stage reactions to achieve complete mass transfer which are unsuitable for automated high-throughput processes. Several techniques are now available that can shorten diffusion distances and reduce the number of reaction steps, subsequently some attempts to produce fully automated materials synthesis robots based on these techniques have been made.(Carey et al. 2011; Fujimoto et al. 2004; Pullar et al. 2007a). These robots involved the mixing of pre-prepared slurries or metal salt solutions, which are subsequently heat-treated to bring about chemical change with varying functionality. Pullar *et al.* had a five stage process which is shown in figure 1.22. The stages were: 1) mixing of premade metal oxide slurries in all possible combinations, 2) printing of slurries as dots using an ink-jet printer, 3) heat-treatment in a multi-zone furnace, 4) sample measurement, 5) data storage. This robot was named the London University Search Instrument, LUSI and the approach had the potential to make up to 10000 samples a day.(Pullar et al. 2007a; Pullar et al. 2007b).

Figure 1.22. Schematic diagram of the combinatorial printing and firing process of the LUSI robot. Figure adapted from (Pullar et al. 2007a).

The Carey *et al.* approach was similar, using a micro-litre scale solution processing robot to mix ceramic slurries in varying compositions that were then printed to produce combinatorial arrays of sample libraries. The libraries could be heat-treated to bring about further solid-state transformations if neccessary. Structural analysis was conducted using an X-ray diffractometer with an *xyz* translational stage, allowing collection of multiple patterns in-line.(Carey et al. 2011)

Figure 1.23. A photograph of the Li-Al-Mn-O library printed robotically from stabilised premixed slurries. Figure adapted from (Carey et al. 2011).

Fujimoto *et al.* reported a robot that automatically mixed aqueous metal salts and slurries of nano-sized Li_2O, Fe_2O_3 and TiO_2 in water, and subsequently heat-treated them at three different temperatures. Heating at three different temperatures allowed a much greater area of phase space to be investigated. An automated X-ray diffractometer was also developed for data collection and subsequent structural analysis.(Fujimoto et al. 2004)

The HiTCH flow synthesis process described in section 1.5 was adapted into an automated robotic platform by Darr and co-workers and called the rapid automated materials synthesis instrument, RAMSI. RAMSI incorporated a modified

HiTCH flow synthesis reactor which was controlled by a PC with GUI interface to control flow-rates, temperature and pressure. Automated liquid handling functions were able to conduct sample clean-up and printing. The synthesis section of RAMSI is shown in figure 1.24.

Figure 1.24. Schematic diagram of the RAMSI synthesis section. P = HPLC pump, Isco = ISCO syringe pump, RSV = Rheodyne switch valve, H = heater, R = reactor, BPR = backpressure regulator, SV = switch valve, LLS = liquid level sensor. Figure adapted from (Lin et al. 2010).

Samples had to then be manually heat-treated and embedded into wellplate libraries. RAMSI was previously used to synthesise a range of europium doped yttrium hydroxide (Eu^{3+}:$Y(OH)_3$) red nanophosphors.(Lin et al. 2010) Eight compositionally unique samples were generated at a rate of ~ 5 samples per hour; subsequently, these were cleaned and printed as ceramic dots. The ceramic dots for each composition could then be heat-treated at different temperatures to produce a library of samples, which were tested for fluorescence colour and intensity, as shown in figure 1.25. The system was limited by the speed of mixing of each precursor composition and the washing of the reactor between samples. These limitations could be reduced firstly by reducing any unnecessary length of pipe, lowering the overall residence time within the apparatus, and secondly by ordering the compositions in such a way that contamination between samples could be reduced. By doing this the washing times between samples could be reduced and thus the total throughput could

be increased. This report showed that RAMSI could perform and entire CHFS process from mixing to synthesis and production of dots, ready for heat-treatment.

Figure 1.25. a) A photograph under UV light (λ = 254 nm) showing the changes in fluorescence intensity with Eu^{3+} content (*x*-axis) heat-treatment temperature (*y*-axis). b) Contour plot of the extracted image intensities as a function of heat-treatment temperature and Eu^{3+} content. Figure adapted from (Lin et al. 2010).

1.6. Hypothesis

1.) Firstly can intimate mixtures of nano-sized metal oxides or hydroxides made via continuous hydrothermal flow synthesis (CHFS) be used as precursors for direct and efficient solid-state reactions? The aim being to reduce the time taken to directly form complex (difficult to make) layered heterometallic oxides by using short diffusion distances (of a couple of nm or so) in the precursors, so the two reactants can fully react. By virtue of being nano-sized, the energy barrier to diffusion may also be lowered as a greater amount of the atoms are on the surface and therefore able to react at a lower temperature.

2.) Secondly, if the first hypothesis is possible, can this route be extended to doped variants of the same compounds, which may normally be laborious to make. Ideally in order to make this efficient, a high-throughput continuous hydrothermal flow reactor (a variant of CHFS) might be used to make a nano-precursor library which differs in composition. Can I split this library into daughter libraries which can each be heat-treated in parallel at a different temperature to allow rapid optimisation of reaction conditions and composition for the mapping of phase diagrams of "difficult to make" heterometallic oxides which do not require any grinding in order to complete mass transfer.

3.) Can full automation be used in hypothesis 2 to increase the number of samples it is possible to synthesise practically in a single experiment? Further to this would automation allow the increase in the number of libraries that can be heat-treated, therefore getting an even better idea of the phase stability of a target phase and find the "true" phase boundary under a given set of conditions?

Chapter 2

Materials and Methods

2.1. Continuous Hydrothermal Flow Synthesis

2.1.1. System 1 – Manual Reactor

All precursors were synthesised using continuous hydrothermal flow synthesis (CHFS); the basic concept for which was described in chapter 1. In detail the system used in this thesis was based on the reactor described originally by Adschiri *et al.*(Adschiri et al. 1992) the basic design of system 1 is shown schematically in figure 2.1.

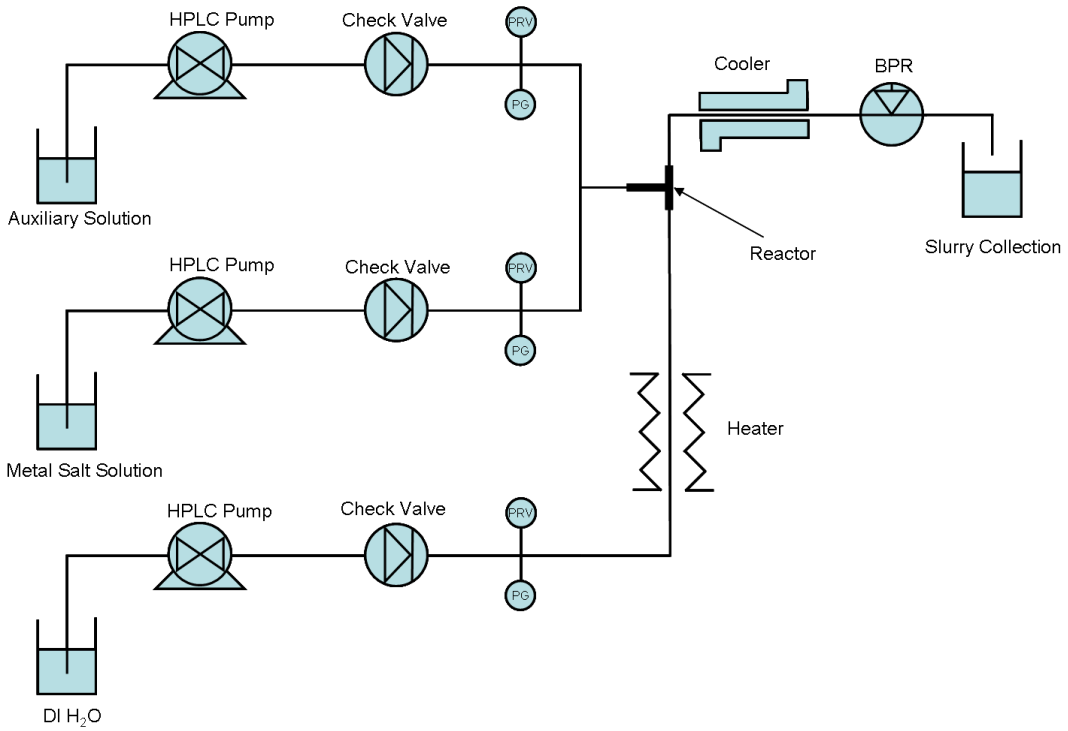

Figure 2.1. Schematic diagram of system 1. PRV = pressure release valve, PG = pressure gauge, BPR = back-pressure regulator.

System conditions were 723 K and 24.1 MPa unless otherwise stated. All pumps were fitted with stainless steel (SS) piston pump heads (Gilson 305 model). The first pump head was used to pump deionised (DI) water to a heater. Metal salt and auxiliary feeds were pumped using the other two pumps. Each pump feed consisted of a check valve (Swagelok™ SS-CHS2-1) to prevent back flow, and a

pressure release valve (Swagelok™ SS-4R3A-EP) set to 27.6 MPa, which are shown schematically in figure 2.2 and 2.3, respectively, and a pressure gauge (RS Cl 1.6). Feed line components were connected using 1/8" outside diameter (OD) stainless steel (316SS) tubing.

Figure 2.2. Components of the CH series Swagelok™ check valve. (Image adapted from Swagelok™ check valve catalogue).

Figure 2.3. Components of the R3A series Swagelok™ release valve. (Image adapted from Swagelok™ release valve catalogue).

The water feed, having passed through the valves, flows into a custom heater, which is shown schematically in figure 2.4 below.

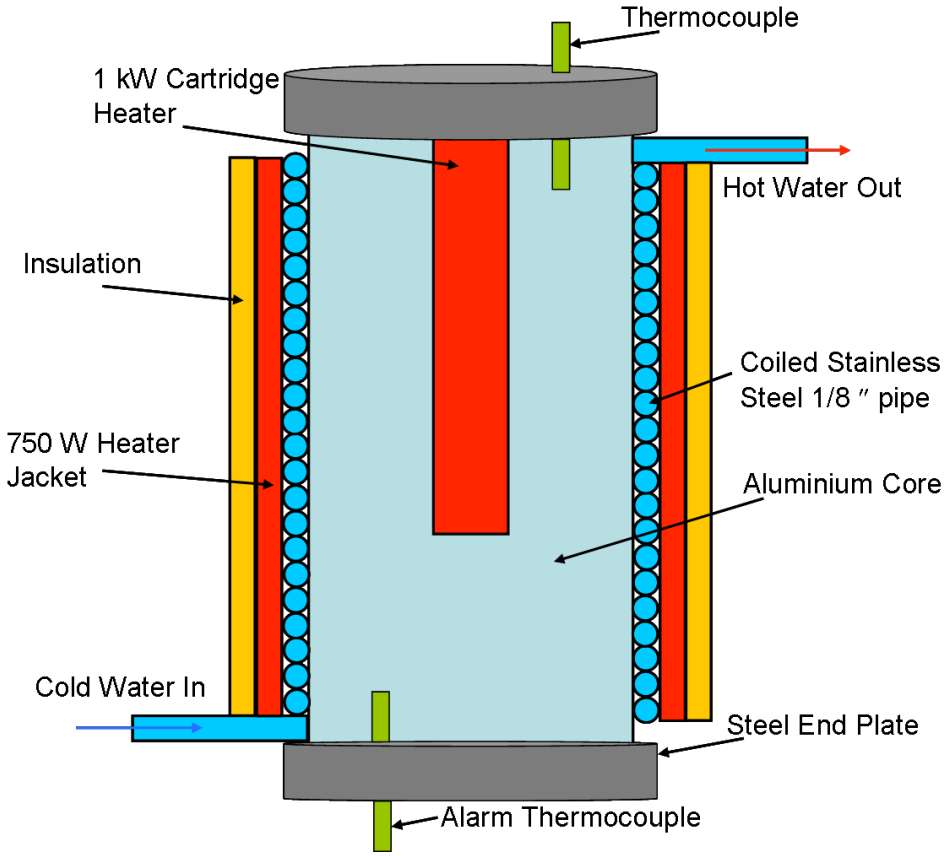

Figure 2.4. Schematic diagram of the heater assembly (not to scale).

The heater is constructed from a coil of 6 m of 316SS pipe ¼ " OD which is coiled around an aluminium core. The aluminium core was heated using a 1 kW cartridge heater (Watlow, Firerod) inserted into a drilled hole in the centre, further heating was provided by two 750 W heater jackets which were wrapped around the pipe coil. The whole assembly was insulated using a RS Microtherm® flexible insulating quilt and further ceramic blanket insulation. The temperature was monitored using a J-type thermocouple inserted into the top of the aluminium core, for safety a further J-type thermocouple was inserted into the bottom of the aluminium core to be used as an alarm. The assembly was held together between two steel end plates which were attached to each other with brass studding.

The metal salt and auxiliary feeds, once passed through the safety valves were mixed in flow in a 1/8 " OD T-piece (Swagelok™, part no.: SS-200-33). The resulting mixed flow passed into a confined jet mixer, whereupon it met the flow of scH_2O.

The confined jet mixing geometry is represented schematically in figure 2.5 below and an annotated photograph is presented in figure 2.6.

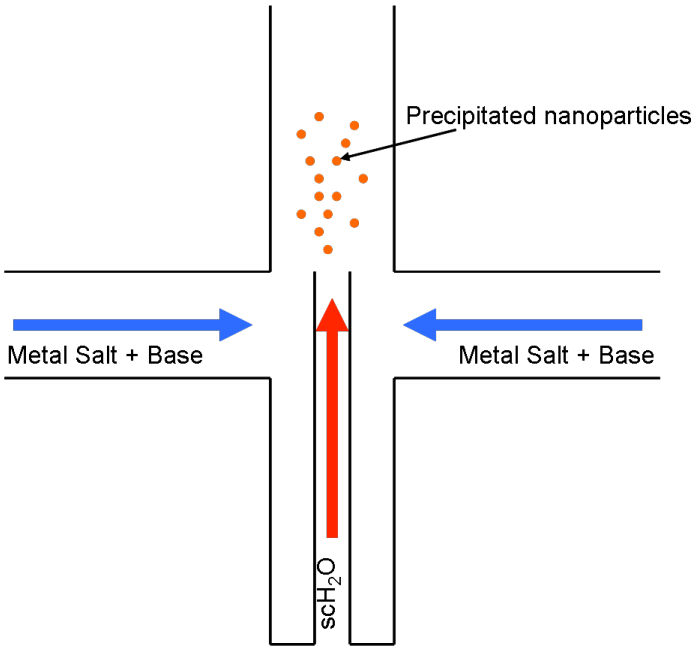

Figure 2.5. Schematic diagram of the co-current mixing geometry used in all reactors (not to scale).

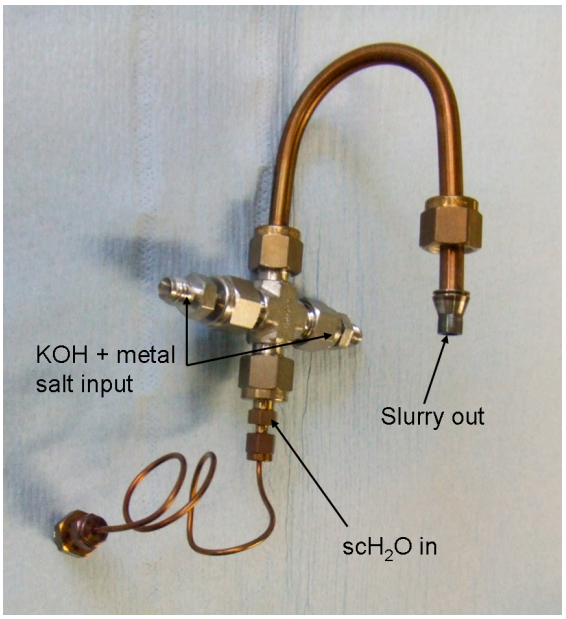

Figure 2.6. Annotated photograph of the co-current mixing point.

The confined jet mixer was constructed around a 1/4 " cross (Swagelok™, part no.: SS-400-4). The scH_2O (723 K) entered the cross through the bottom arm in a 1/16 " OD 316SS pipe, which was attached to the 1/4 " cross using a bored-through reducing union (Swagelok™ part no.: SS-100-R-4). The scH_2O formed a jet as it entered the larger diameter pipe. The mixture of metal salt and auxiliary feeds (299 K) entered the cross through the left and right arms in an 1/8 " OD SS316 pipe

which was connected to the cross by a reducing union (Swagelok™ part no.: SS-200-R-4). Precipitation of nanoparticles occurred (in fractions of a second) on mixing of the nitrate salt and auxiliary feeds in the jet of scH_2O. The resulting slurry exited the mixer through the top arm in a 220 mm 1/4 " OD 316SS pipe.

The slurry was then cooled in a pipe-in-pipe cooler, which is represented schematically in figure 2.7., and was constructed from straight 500 mm 1/4 " OD 316SS tubing fed through a 3/4 " OD 316SS tube connected to a continuous cooling water supply. The slurry then exited the system through a back pressure regulator (Tescom model: 26-1762-24-194).

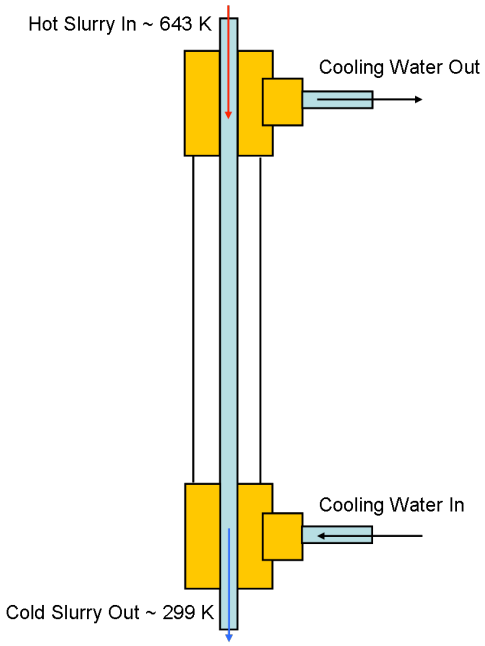

Figure 2.7. Schematic diagram of the pipe-in-pipe cooler (not to scale).

2.1.2. System 2 – High-Throughput Continuous Hydrothermal (HiTCH) Flow Synthesis

System 2 was designed for high-throughput synthesis of nanomaterials. Named high-throughput continuous hydrothermal (HiTCH) flow synthesis, system 2 differed slightly from system 1, and is represented schematically in figure 2.8.

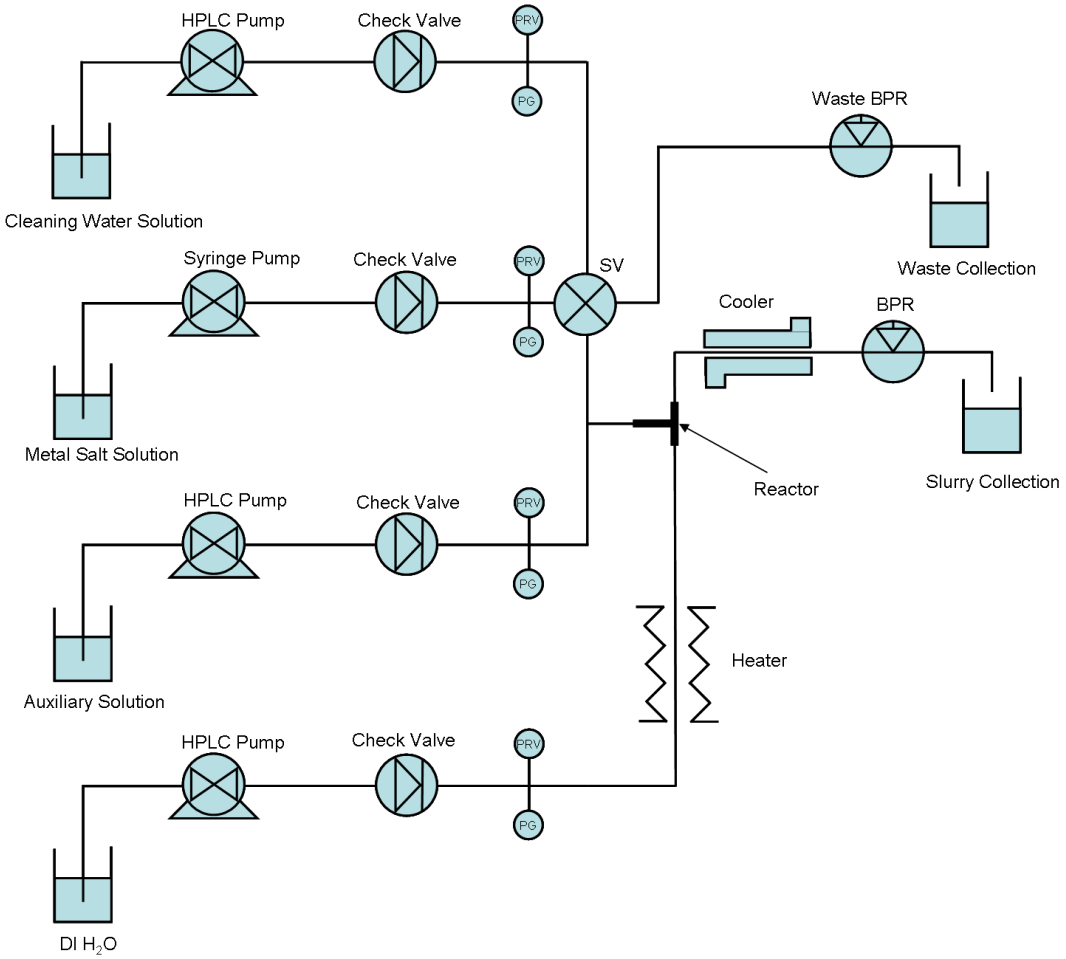

Figure 2.8. Schematic diagram of the HiTCH flow synthesis reactor. SV = switch valve, PRV = pressure release valve, PG = pressure gauge, BPR = back pressure regulator.

An extra cleaning water feed was included to prevent contamination between samples. A Rheodyne™(model 7010) switch valve that was used to control the direction of the metal nitrate and cleaning water flows. An ISCO (model 260d) syringe pump was used to inject premixed metal salt solutions through the switch valve and into the reactor sequentially. The switch valve had 2 inputs and 2 outputs. Input 1 was clean DI water and input 2 was the metal salt solutions from the ISCO syringe pump. Output 1 was to the reactor T-piece and output 2 was to a waste BPR. All inputs and outputs were linked with an internal 2 mL loop and could be in one of two positions as described in table 2.1.

Table 2.1. Destinations of both metal salt and cleaning water feeds based on switch valve position. SV = switch valve.

SV Position	Metal Salt Destination	Cleaning Water Destination
1	Reactor	Waste BPR
2	Waste BPR	Reactor

The valve was switched manually using an 'inject' button. Using this method of switching between metal salt and clean DI water feeds, it was possible to 'clean' the reactor between samples whilst maintaining reaction conditions. The sequence for cleaning between samples is shown in table 2.2.

Table 2.2. Cleaning sequence for high-throughput reactions. SV = switch valve

SV position	Process	Pump	Purpose	Time / s
1	Pre-run	ISCO	10 – 20 mL of the next metal salt	10 – 20
2	System wash	Gilson	H_2O rinse	120
1	Real run	ISCO	Metal salt solution for collection	Sample size dependant
2	System wash	Gilson	H_2O rinse	180

Once injected into the system the metal salts flowed through the reactor and were precipitated in the same manner as that described for system 1.

2.1.3. System 3 – Rapid Automated Materials Synthesis Instrument, RAMSI

System 3 was a HiTCH flow synthesis reactor that was attached to an automated robot called the Rapid Automated Materials Synthesis Instrument, RAMSI. The robot had three functionalities, synthesis, clean-up and printing (described below) and was designed for high-throughput combinatorial synthesis of nanomaterials. Samples were moved around and through the three functionalities using a *xyz* robot arm. RAMSI was constructed by Labman Automation LTD, Stokesley UK. The control of RAMSI was achieved through a GUI interface. All programming was performed by Dr. Tian Lin. Full blueprints, photographs, images and part lists of RAMSI and the GUI system, which may help understanding, are presented in appendix 1.

2.1.3.1. Synthesis

The synthesis section of RAMSI utilised a modified HiTCH reactor, the setup was close to system 2 a schematic diagram of which is shown in figure 2.8. System 3 differed from system 2 by the inclusion of an automated metal salt mixing station that was used to mix each metal salt composition prior to delivery into the reactor. The automated metal salt mixing section is shown schematically in figure 2.9 below.

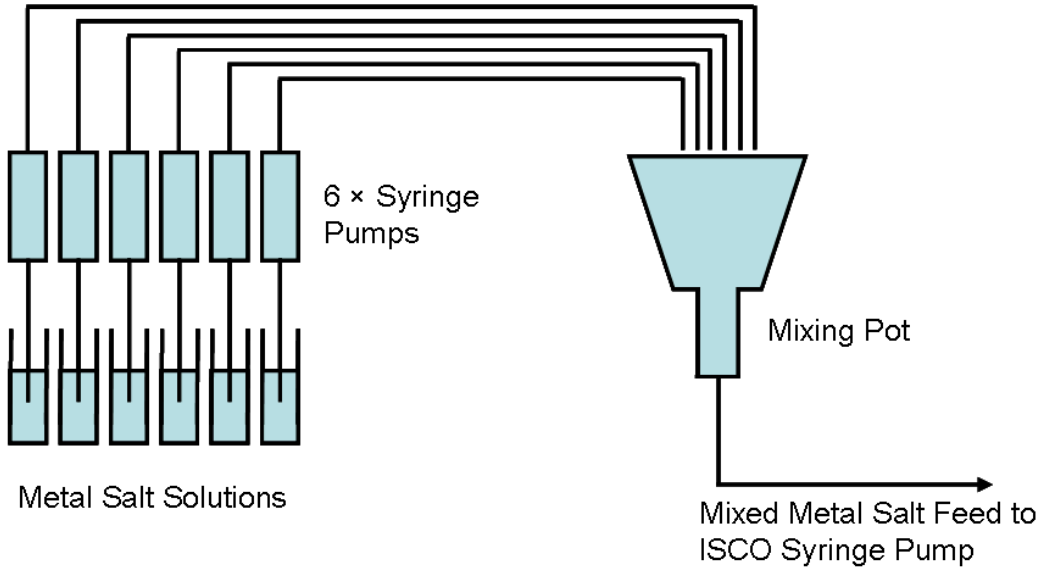

Figure 2.9. Schematic diagram of the automated metal salt mixing section of RAMSI.

All aspects of the synthesis are controlled by the RAMSI program through a graphical user interface, (GUI) and by the synthesis "RAN" form which designates parameters for each sample (e.g. metal salt mixtures, reactor temperature and pressure). The synthesis section starts with 6 × 25 mL Tecan syringe pumps with a dispersing resolution of 100 μL which metered the quantity of each metal salt designated by the starting parameters to a mixing pot. The mixing point had a stirrer, a drain and a feed to the ISCO syringe pump that could draw the mixed metal solution and then dispense it through the switch valve to the reactor. As the ISCO pump delivers metal salt to the reactor the switch valve diverts the cleaning water feed from Gilson pump 3 to the waste BPR (BPR 2).

Samples entered the HiTCH reactor in the same manner as system 2. Following the reaction slurries were collected in 50 mL falcon tubes in a collection carousel. Where they were collected by the robot arm and placed into tube racks in sequence.

2.1.3.2. Clean-up

The cleanup section of RAMSI consisted of two Sigma 4K-15R robotic centrifuges with capacity of 28 × 50 mL falcon tubes each, and a motor-driven clean-up carousel with stations for supernatant scanning and removal, deionised water addition and slurry redispersion. A fixed turbidimetry station was also used as a quick check to ensure each 50 mL falcon tube was clear at a particular level just after it was removed from the centrifuge. An eight station cleanup carousel shifted the sequence of sample tubes around, while the tubes at these stations could be processed in parallel.

(i) Centrifugation of Samples Tubes.

The robot arm sent tubes from the tube rack to a centrifuge where sample centrifuging was conducted for 1 minute at 4500 rpm. If at any point in the entire clean-up process, an odd number of tubes were being processed, the robot placed dummy tubes (filled with 50 mL of water) in the centrifuge in order to ensure the balance. When a centrifuge finished running a cycle, the robot arm sent all samples to the fixed turbidimetry station in sequence.

(ii) Fixed Turbidimetry Station.

At the fixed turbidimetry station each the sample passed across a fibre-optic sensor, which was used to determine whether the slurry was above or below a critical threshold of turbidity at a certain height of the falcon tube (corresponding to a volume level of 40 mL in the tube). This determined whether tubes were worth sending to the cleaning carousel or not, since part-settled tubes would still be turbid at this height due to suspended matter. Tubes that failed this test could immediately be returned to the centrifuge for further centrifugation.

(iii) The Clean Up Carousel.

The clean up carousel had eight stations, which allowed parallel operations to be carried out. The carousel had the following positions and functionalities: (1) tube loading position, (2) supernatant scan and removal, (3) DI water refill, (4) homogenisation, (5) DI water refill, (6) empty station, (7) empty station, and (8) tube pick-up position. At station 2, a second fibre-optic turbidimetry sensor (which was

motor-driven and scanned the *z*-axis), scanned the slurry filled tube vertically. A threshold value was set on the fibre-optic amplifier allowing calculation of the amount of supernatant which would have been removed according to the turbidimetry threshold. Then a *z*-axis movement needle (linked to a withdrawal pump) at the same station, removed water down to the calculated threshold height (thus a known amount of liquid was removed). The needle was withdrawn from the tube and rotated 90 degrees to be lowered and washed in an adjacent flowing water wash. The tubes then passed onto station 3 which was a DI water refill station. According to the parameters set by the original program, the tube was then refilled with clean deionised water (by a 25 mL Tecan syringe pump) up to usually 40 mL. At station 4, the slurry was redispersed in the clean supernatant using a high shear mixer (homogenizer) for a period of 30 seconds. The mixer was able to be lowered into the tube, run, stop, lift away and then be washed in a dedicated flowing water wash. At station 5, the tube was then topped up to a total of 50 mL (+10 mL) clean supernatant ready for further centrifugation. Each tube in the carousel eventually reached station 8 (unloading station) where the robot arm could take it back to the centrifuge if required. When all tubes had been cleaned (135 mL of DI water exchanged total), the supernatant was manually checked to ensure pH 7 had been reached before being concentrated for printing.

2.1.3.3. Printing

Cleaned slurries were prepared for printing by manually adding 600 – 1000 μL of DI water to wet slurry to achieve a concentration of *ca.* 1.0 ± 0.2 $g.mL^{-1}$ (per gram of wet slurry, actual DI water content was higher). The printing device of RAMSI was a customised pipette tip (on the robot arm) which was connected to a 5.0 mL Tecan syringe pump. The customised pipette tip could auto aspirate and dispense slurries and load/discard 5000 μL Eppendorf tips from a fixed tip rack. The robot arm moved to each slurry in turn and aspirated a set amount of the concentrated slurry given by the amount and volume of dots entered into the GUI originally. The robot arm then moved to the printing area where dots of slurry were dispensed from a height of 10 mm onto silicon release paper. Pipette tips were discarded in a pipette bin before collection of a new one for the following samples. Dots were left to dry in air overnight.

2.2. Synthesis Methodology

2.2.1. Synthesis of Lanthanum Nickelate – $La_4Ni_3O_{10-\delta}$

a) Synthesis of $La_4Ni_3O_{10-\delta}$ (Effect of base concentration)

8.660 g of [$La(NO_3)_3.6H_2O$] was dissolved in 200 mL of DI water to form a 0.1 M solution. 4.362 g of [$Ni(NO_3)_2.6H_2O$] was dissolved in 150 mL of DI water to form a 0.1 M solution. These precursors were pumped into system 1 described in section 2.1. Pump rates were 20 mL.min^{-1} for the scH_2O feed, and 10 mL.min^{-1} for both metal nitrate mixture and KOH auxiliary solution. KOH concentration was varied between samples as described in table 2.3.

Table 2.3. Precipitation conditions for each $La_4Ni_3O_{10-\delta}$ sample.

Heater Temperature / K	La:Ni Ratio	KOH Concentration / M
723	4:3	0.2
723	4:3	0.4
723	4:3	0.6
723	4:3	0.8
723	4:3	1.0

The resulting slurries were collected in 50 mL falcon tubes and washed 4 times by centrifuging at 4500 rpm for 1 minute. The supernatant was poured off and replaced with clean deionised water and redispersed using a vortex mixer each cycle. Following 4 washes the supernatant pH was 7. The slurries were then dried in a freeze dryer for 18 hours. All the dry powders were heat-treated at 1348 K for 12 hours using a ramp rate of 10 K.min^{-1}.

b) Effect of coprecipitation method on the formation of $La_4Ni_3O_{10-\delta}$.

The first coprecipitation method was by CHFS using system 1. 2.47 g of [$La(NO_3)_3.6H_2O$] was dissolved in DI water (57 mL) and 1.25 g of [$Ni(NO_3)_2.6H_2O$] was dissolved in DI water (43 mL). Both solutions were mixed to create a 0.1 M solution in a 4La:3Ni ratio. 1.0 M KOH was used throughput to aid precipitation. System 1 was used at 723 K and 24.1 MPa to co-precipitate green slurry that was cleaned using the method described above. Pump rates were 20 mL.min^{-1} for the scH_2O feed, and 10 mL.min^{-1} for both metal nitrate mixture and KOH auxiliary solution. The slurry was then freeze dried for 18 hours.

The second coprecipitation method was a direct coprecipitation method. [$La(NO_3)_3.6H_2O$] (28.57 mL, 1.237 g, 0.1 M) was added to [$Ni(NO_3)_2.6H_2O$] (21.43 mL 0.623 g, 0.1 M) and stirred whilst adding KOH (50 mL 2.805 g, 1.0 M) dropwise into the solution. Precipitation of a green slurry occurred, which was dried in air on a hotplate to produce a green powder (1.089 g, yield = 58.6 %).

Heat-treatments on both powders were conducted in air at 1348 K for 12 hours using a ramp rate of 10 $K.min^{-1}$.

c) Synthesis of $4La(OH)_3$:$3Ni(OH)_2$ for *In Situ* Powder Diffraction.

System 1 was used with a heater temperature of 723 K and pressure of 24.1 MPa. 2.47 g of [$La(NO_3)_3.6H_2O$] was dissolved in DI water (57 mL) and 1.25 g of [$Ni(NO_3)_2.6H_2O$] was dissolved in DI water (43 mL) to form a 4La:3Ni 0.1 M solution. 1.0 M KOH was used to aid precipitation of the mixture. Pump rates were 20 $mL.min^{-1}$ for the scH_2O feed, and 10 $mL.min^{-1}$ for both metal nitrate mixture and KOH auxiliary solution. Solutions were co-precipitated, cleaned using 4 centrifugation clean DI water and re-dispersion cycles until pH 7 was achieved. The resulting wet green powder was freeze dried for 18 hours.

2.2.2. High-Throughput Synthesis of $La_4Ni_{2.7}M_{0.3}O_{10-\delta}$ (Where M = V, Cr, Mn, Fe, Co, Ni, Cu, Al).

Samples were synthesised on system 2, reactor temperature and pressure were set to 723 K and 24.1 MPa respectively. Pump rates were 20 $mL.min^{-1}$ for the scH_2O feed, and 10 $mL.min^{-1}$ for both metal nitrate mixture and KOH auxiliary solution. 100 mL sample sizes which were made up of 57 mL of [$La(NO_3)_3.6H_2O$] (2.47 g, 0.1 M), 39 mL of [$Ni(NO_3)_2.6H_2O$] (1.12g, 0.1 M) and 4 mL of [$M(NO_3)_x.xH_2O$] (0.1 M) (where M = V, Cr, Mn, Fe, Co, Ni, Cu, Al and masses are given in table 2.4).

Table 2.4. Masses of the metal salt used in each solution.

Metal Salt	Mass / g
$[V(SO_5).5H_2O]$	0.101
$[Cr(NO_3)_3.9H_2O]$	0.160
$[Mn(NO_3)_2.4H_2O]$	0.100
$[Fe(NO_3)_3.9H_2O]$	0.162
$[Co(NO_3)_2.6H_2O]$	0.116
$[Ni(NO_3)_2.6H_2O]$	0.117
$[Cu(SO_4).5H_2O]$	0.099
$[Al(NO_3)_3.9H_2O]$	0.150

Each aqueous precursor was metered into the hydrothermal apparatus using an ISCO syringe pump. The cleaning cycle between each sample is described in table 2.2. Slurries were collected in 50 mL falcon tubes and cleaned manually as was described in section 2.2.1 and freeze dried for 18 hours. The resulting powders were split into 3 and heat-treated at 1348, 1448 or 1548 K for 12 hours, respectively, in air using a ramp rate of 10 $K.min^{-1}$.

2.2.3. High-Throughput Synthesis of $La_4Ni_{3-x}Fe_xO_{10-\delta}$.

Samples were synthesised on system 3, the HiTCH synthesis module of RAMSI. Reaction conditions entered into the RAMSI GUI are shown in table 2.5 and 2.6.

Table 2.5. Reaction conditions entered into RAMSI GUI.

Action	
Pressure Set Point	3600 psi
Temperature Set Point	450 °C
Collection Lag Time	50 s
Pre-Run Time	90 s
Flushing After Pre-Run	120 s
Flushing Time Via Waste	120 s
Flushing Time Via Collection	30 s
Sample Volume	42 mL

Table 2.6. Flushing conditions for ISCO and TECAN syringe pumps.

Pump	Flushing No.	Flushing Volume
ISCO	1	50
ISCO	2	30
ISCO	3	30
TECAN	1	10
TECAN	2	10

Samples were collected in 50 mL falcon tubes on the collection carousel and placed into tube racks ready for cleaning. The parameters for the clean-up were entered into the GUI using the following values in table 2.7.

Table 2.7. Clean-up conditions entered into GUI.

Action	
Centrifuge Time	20 mins.
Fixed Point	40 mL
Min. Supernatant For Washing	10 mL
Min. Summed Exchange	135 mL
Max. Continual Rejections	3
Final Volume	5 mL
Centrifuge Speed	4500 rpm

All samples were cleaned using the cleaning carousel section of RAMSI, the running order of which is explained in section 2.1.3.2. Once the cleaning cycle was completed, the supernatant pH was 7 (measured manually), and 5 mL of concentrated slurry remained in each tube.

The resulting concentrated slurries were diluted manually to 1.0 ± 0.2 g.mL^{-1} (DI water was added to wet slurry therefore actual concentration was lower) using DI water in order to produce ceramic dots that would dry without cracking. 6 × 100 μL and 6 × 125 μL dots were printed on silicon release paper using RAMSI; and dried in air overnight.

Heat-treatments were conducted on a Pt plate at 1348 K and 1573 K for 12 hours. In each case the temperature was increased at 2 K.min^{-1} to 353 K for 6 hours, before being ramped at 2 K.min^{-1} to a holding temperature of either 1348 K or 1573 K for 12 hours. The ramp rate was kept low in order to prevent cracking of the dots. The heat-treated dots were mounted onto a custom 96 well aluminium wellplate (86 × 123 mm with 4mm wide, 1.5 mm deep wells which were 9 mm apart).

2.2.4. High-Throughput Synthesis of $La_4Ni_{3-x}M_xO_{10-\delta}$ and $La_3Ni_{2-x}M_xO_{7-\delta}$ (Where M = Mn, Pd, Al and Ga $x = 0.0 – 2.0$ and $\Delta x = 0.2$)

Samples were synthesised on system 3 in the HiTCH flow synthesis of RAMSI. Starting materials, [$La(NO_3)_3.6H_2O$], [$Ni(NO_3)_2.6H_2O$], [$Mn(NO_3)_2.4H_2O$], [$Pd(NO_3)_2.2H_2O$], [$Al(NO_3)_3.9H_2O$] and [$Ga(NO_3).6H_2O$] all ≥ 99.9 % purity were purchased from the Sigma-Aldrich Chemical Company (Dorset, UK). 1.0 M KOH

≥ 85 % was purchased from VWR (Leicestershire, UK). 0.1 M Stock solutions of each metal nitrate salt were made by dissolving in DI water. The resulting La, Ni, Mn, Pd, Al and Ga nitrate solutions were attached to the 1st, 2nd, 3rd, 4th, 5th and 6th Tecan syringe pump feed lines respectively. Reactions conditions were then set as in table 2.8 and 2.9 in the RAMSI GUI.

Table 2.8. Reactions conditions entered into the RAMSI GUI for the synthesis of $La_4Ni_{3-x}M_xO_{10-\delta}$ and $La_3Ni_{2-x}M_xO_{7-\delta}$.

Action	
Pressure Set Point	3600 psi
Temperature Set Point	450 °C
Collection Lag Time	75 s
Pre-Run Time	60 s
Flushing After Pre-Run	60 s
Flushing Time Via Waste	60 s
Flushing Time Via Collection	30 s
Sample Volume	25 mL

Table 2.9. Flushing conditions for ISCO and TECAN syringe pumps.

Pump	Flushing No.	Flushing Volume / mL
ISCO	1	30
ISCO	2	30
TECAN	1	10
TECAN	2	10

Pump rates were 20 $mL.min^{-1}$ for scH_2O and 10 $mL.min^{-1}$ for both KOH and metal salt solutions. Samples were collected in 50 mL flacon tubes in the collection carousel and moved by robot arm to the tube racks. Samples clean-up was performed on RAMSI using the configuration described in table 2.10.

Table 2.10. Clean-up conditions entered into GUI for the synthesis of $La_4Ni_{3-x}M_xO_{10-\delta}$ and $La_3Ni_{2-x}M_xO_{7-\delta}$.

Action	
Centrifuge Time	1 min.
Fixed Point	40 mL
Min. Supernatant For Washing	10 mL
Min. Summed Exchange	135 mL
Max. Continual Rejections	1
Final Volume	5 mL
Centrifuge Speed	4500 rpm

Once pH 7 was reached, (checked manually) samples were freeze dried for 18 hours. Each sample was split into 3 and heat-treated at 1348 K, 1448 K and 1548 K, respectively, for 12 hours in air, on a platinum plate.

2.3. Furnaces

Heat-treatments were conducted in a CWF/1300 muffler furnace from Carbolite, UK. This furnace had a Eurotherm 3216 programmable controller allowing control of heat rate (0.1 K resolution) dwell time, and temperature (max = 1573 K).

2.4. Powder X-ray Diffraction

2.4.1 Bruker – D4

This diffractometer was in Bragg-Brentano geometry and equipped with auto-robotic arm sample changer and used $CuK\alpha_{(I + II)}$ radiation. Samples were loaded into plastic samples holders. Unless stated otherwise, data were collected between 20 – 70 2θ, in 0.05° steps at 4 $s.step^{-1}$. Divergence and anti-scattering slits were both set at 0.5 mm.

2.4.2. Bruker – D500

Bragg-Brentano Diffractometer equipped with a pre-sample monochromator and scintillation detector. This diffractometer was used for accurate cell measurements and data was collected in 2 summed ranges of 10 – 80 °2θ, 0.02 ° steps, 10 $s.step^{-1}$, slits were set at 0.3 mm.

2.4.3. Bruker – D8 – GADDS

High-throughput powder X-ray diffraction (PXRD) of wellplate libraries was conducted using a Bruker-AXS D8 (GADDS) diffractometer. This instrument utilises a large 2D area detector to record large sections of multiple Debye-Scherrer cones simultaneously. The setup with a mounted wellplate is shown in figure 2.10. Both θ and ω can be measured with 0.01 ° resolution using a Cu ($K\alpha_1$ and $K\alpha_2$) radiation source. After collection, the data across the Debye-Scherrer cones can be integrated across ω to produce a standard one-dimensional, 2θ against intensity plot. This diffractometer is equipped with an *x*-*y*-*z* translational stage that can be

programmed to adjust the position of the wellplate after each scan allowing data for each sample to be collected in turn. In high-throughput mode up to 36 patterns, could be collected in 12 hours.

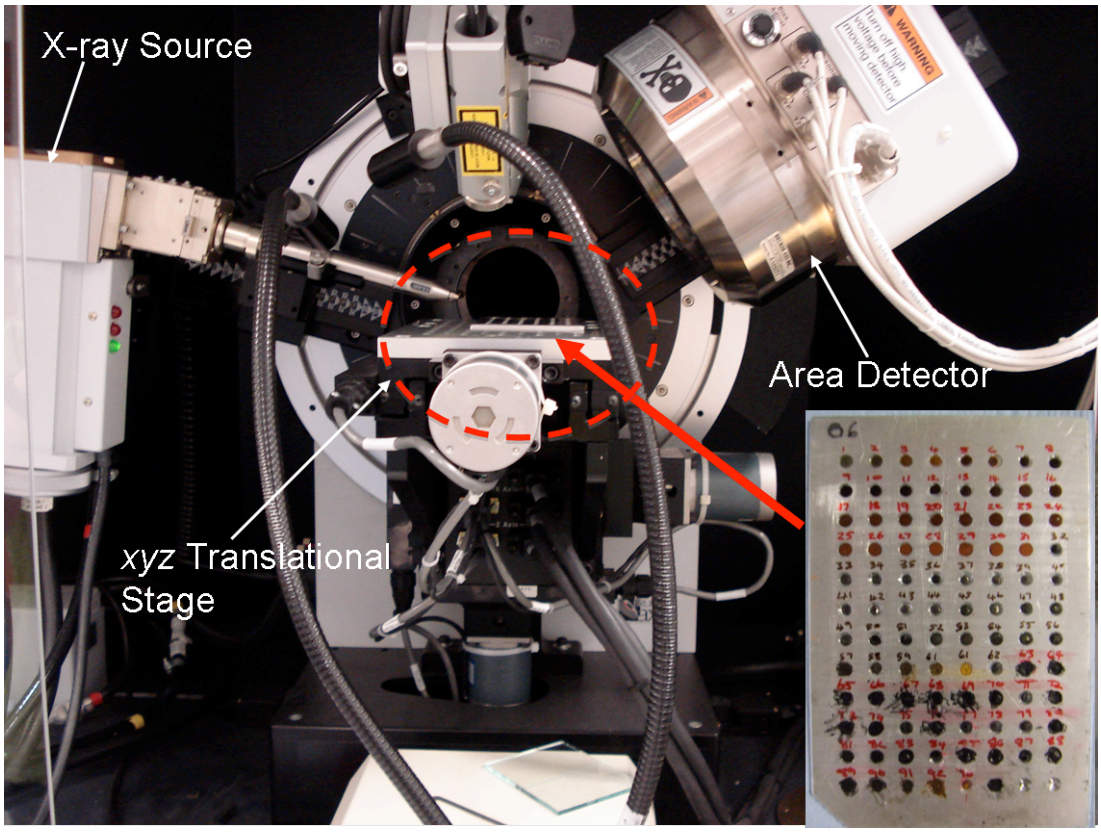

Figure 2.10. Annotated photograph of a wellplate mounted onto the *xyz* translational stage of the Bruker D8 diffractometer.

2.4.4. I11 Beamline

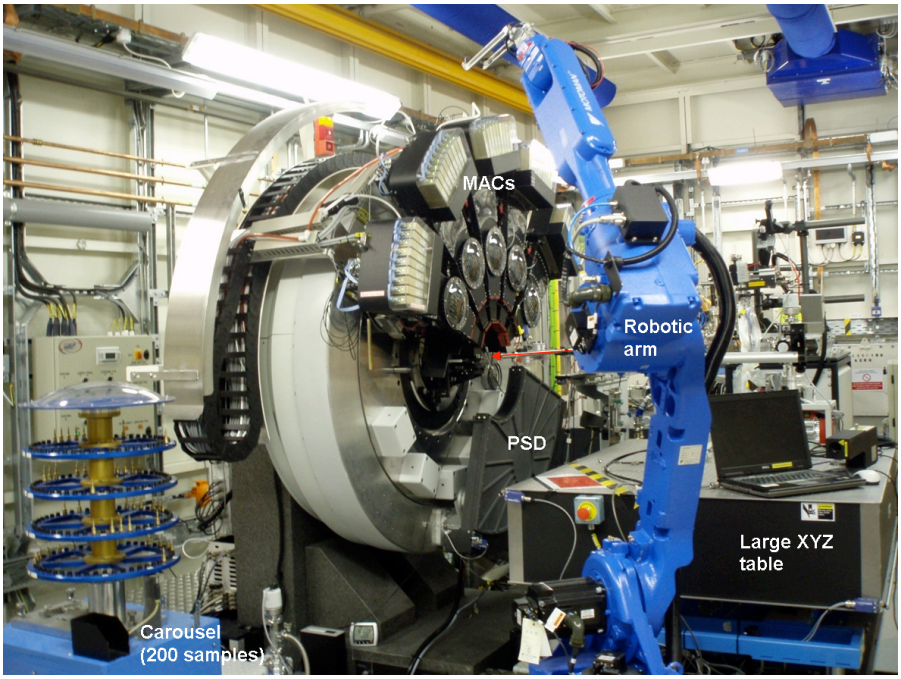

Figure 2.11. Photograph of the I11 Beamline at Diamond Light Source (Harwell, UK). MAC = multi-analyser crystal, PSD = position sensitive detector. Red arrow indicates direction of the beam. Photo courtesy of Dr. Chiu Tang, Diamond Light Source.

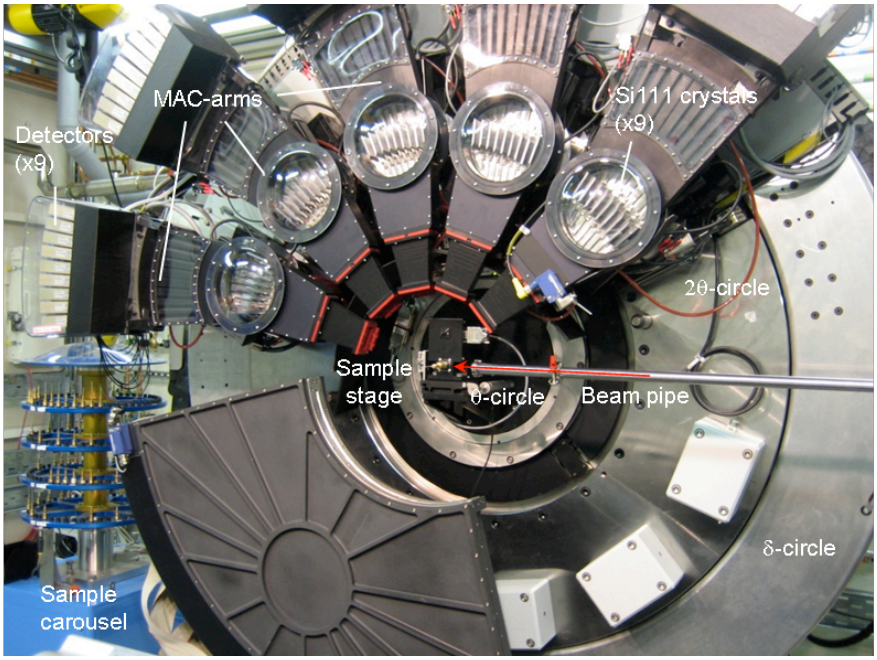

Figure 2.12. Photograph of the I11 Beamline at Diamond Light Source (Harwell, UK). Red arrow indicates direction of the beam. Photo courtesy of Dr. Chiu Tang, Diamond Light Source.

High-resolution powder diffraction data was collected on the I11 beamline at Diamond Light Source, (Harwell U.K.). This beamline had a 90 pole in-vacuum undulator insertion device and a Si(111) monochromator. The beamline had two types of detectors:

i) Multi-analyser crystal (MAC) detectors with 45-channels that allowed for a scanning range of 0 -160 °2θ with a step size of 0.0001 °. This detector was used in Chapter 3 for *in situ* monitoring of reactions involving CHFS coprecipitates.

ii) Position sensitive detector (PSD) with a 90 ° aperture that allowed collection of a powder pattern in ms, for time resolved studies. This detector was used in Chapter 6 for rapid data collection for high-throughput screening of lanthanum nickelate compounds.

Beamline sample cells and stages, including the furnace described below ere mounted onto a translational *x*–*y*–*z* stage that could be moved in and out of the beam. A robot arm was used for automatically changing samples. Loaded capillaries were placed onto the sample carousel and then picked up individually in turn by the robot arm and placed onto the beamline.

2.4.4.1. STOE Capillary Furnace

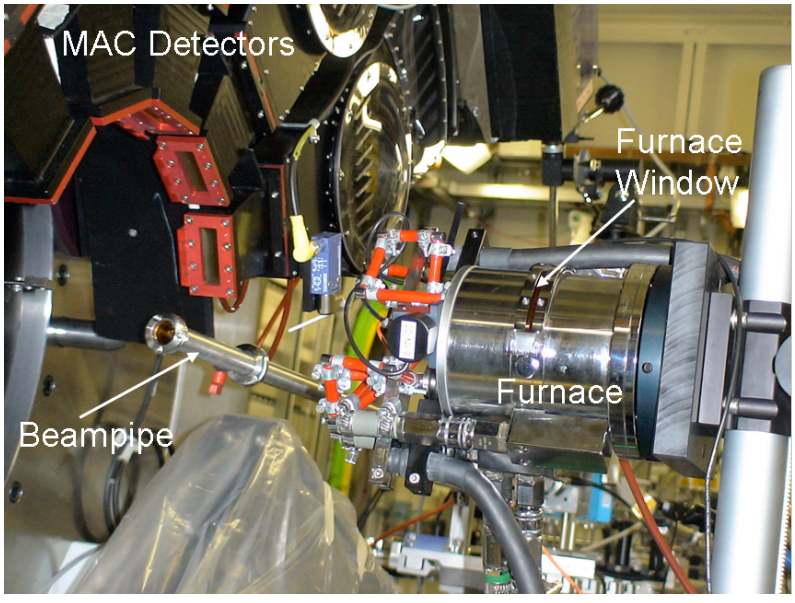

Figure 2.13. STOE capillary furnace mounted onto the I11 beamline.

In situ reactions in Chapter 3 were conducted on the beamline in 0.5 ID quartz glass capillaries (Hilgenberg, Malsfeld, GER) which were mounted into a

STOE capillary furnace. The furnace was mounted onto the *x*–*y*–*z* stage and moved into the beam for data collection. In order to prevent the heating element burning out, it was necessary to evacuate the furnace and backfill with nitrogen. The capillary end was left open to maximise pO_2 content.

2.4.4.2. Data collection – Chapter 3.

In situ data were recorded using a 45 channel multi-analyser crystal (MAC) detector in 120 s scans. A further 60 s was required for the detectors to return to their start position meaning that scans took 180 s in total including dead time. Data were collected over a range of 0 – 90 °2θ which was the maximum allowed by the beryllium window of the furnace, step size was 0.0001 °2θ. In all cases this data were rebinned to a 0.05 °2θ step size allowing correction for the detector crystal orientation. Wavelength (λ = 0.826931(1) Å) and zero point (-0.0039(1) °) were calculated using a silicon standard, (NIST srm640c).

Reactions were conducted in 0.5 mm ID quartz glass capillaries and inserted into a STOE capillary furnace with a heating rate of 10 $K.min^{-1}$ to a holding temperature of 1448 K.

2.4.4.3. Data Collection –Chapter 6.

High-throughput screening data were collected using the PSD detector, collection time was 2 seconds per pattern. A further 30 seconds were required to change samples. All 240 patterns were collected in 2.1 hours. Samples were changed using the robot arm and carousel.

Data for further refinement of 'interesting' structures were collected at room temperature using the MAC detectors. Collection time was 30 minutes of the 2θ range 0 – 160 °2θ. Wavelength (λ = 0.825582(2) Å) and zero point (0.006679(2) °) were calculated using a silicon standard, (NIST srm640c).

2.5. Energy Dispersive X-ray Spectroscopy (EDX)

Elemental ratios were calculated using EDX, on a Hitachi S-3400N SEM with a JEOL 8100 Superprobe energy dispersive X-ray spectrometer.

2.6. Extended X-ray Absorption Fine Structure (EXAFS)

EXAFS data were collected in the B18 instrument at Diamond Light Source, (Harwell, UK). A Si(111) monochromator was used. All Fe K-edges were recorded at room temperature. Each data set was truncated to 8 Å and analysed using the Excurve software package. Data were collected by Andrew Smith and analysis was conducted by Prof. G. Sankar.

2.7. DC Electrical Testing

The DC conductivity of pressed pellets was measured using the Van der Pauw method.(Van der Pauw 1958a; Van der Pauw 1958b) Pellets were pressed in a 13 mm KBr die, and sintered at 1473 K. For sintering, pellets were place onto a platinum plate and preheated at 353 K for 6 hours before increasing to 1573 K at a ramp rate of 1 $K.min^{-1}$ for 12 hours.

The pellet was mounted into a custom built 4-point probe. The pellet assembly was constructed from MACOR machinable ceramic. The design is shown schematically in figure 2.14 below and in an annotated photograph in figure 2.15.

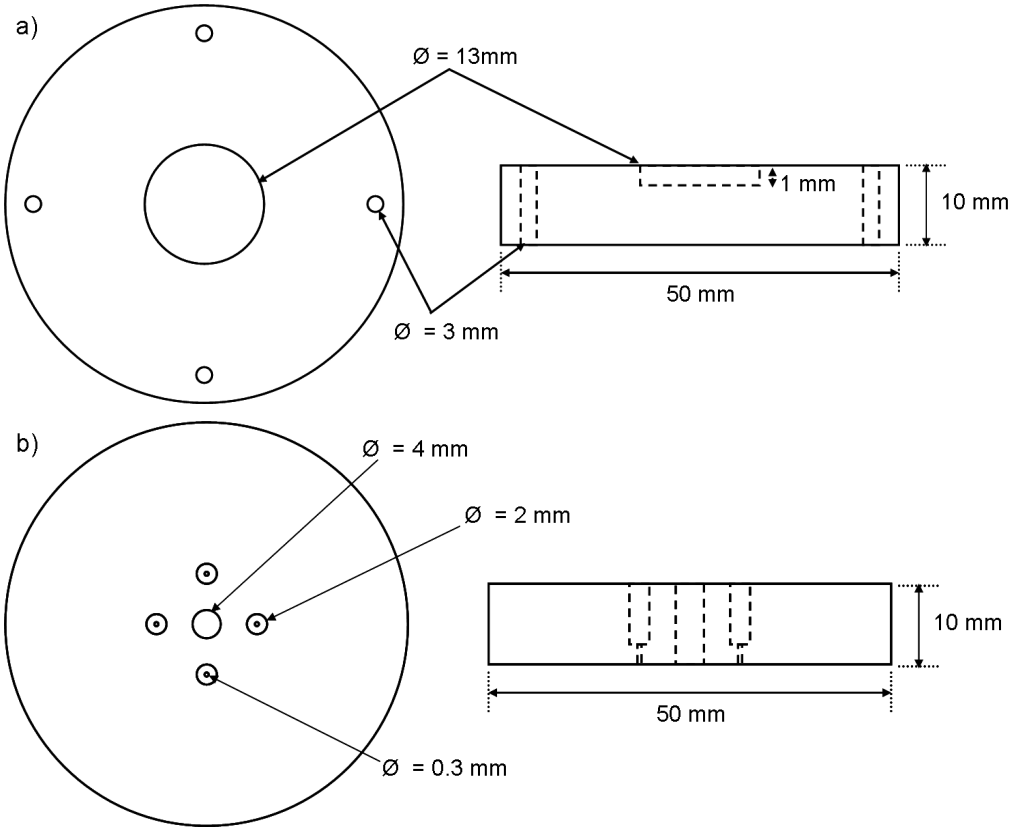

Figure 2.14. Schematic diagram of the pellet assembly of the 4-point probe. a) Bottom section. b) Top section.

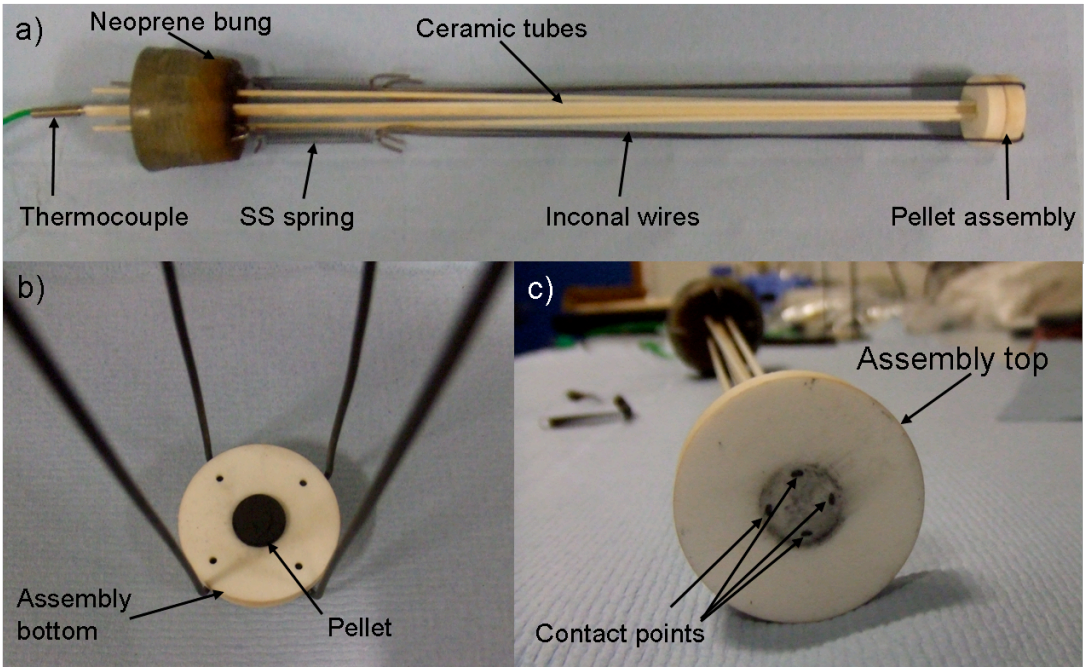

Figure 2.15. Annotated photograph of the DC 4-point probe. SS = stainless steel.

The pellet was placed in a 1 mm deep, 13 mm diameter well that formed the lower half of the assembly. Contacts 1, 2, 3 and 4 were 0.1 mm diameter platinum wire fed through 0.3 mm holes that were placed around the periphery of the pellet. The platinum wires were then fed through 4 × 500 mm ceramic tubes, (thickness = 2 mm OD) one for each wire, which were held in place by a neoprene bung that fitted inside the entrance to the work tube of the furnace. A central supporting 500 mm, 4 mm OD ceramic tube was fed through the centre of the bung and into the pellet assembly, which as well as acting as a support contained a 600 mm K-type thermocouple to monitor the pellet temperature. The whole assembly was held together by 4 × 600 mm inconal wires, which were equally spaced around the perimeter of the lower section of the pellet assembly. The other end was attached to the neoprene bung using steel springs (RS 751-691, 5.0 × 25.0 mm), which helped keep the pellet assembly under pressure.

To make the measurement, the probe assembly was placed inside a 72 mm OD ceramic work tube that was inside a tube furnace (Carbolite MTF/1000 model) the conductivity was then measured using equation 2.1:

$$\rho = \frac{\ln(2)}{\pi l} x \frac{4I}{V_{12,34} + V_{34,12} + V_{23,41} + V_{41,23}} \qquad (2.1)$$

Where ρ = conductivity in $S.cm^{-1}$, l = pellet thickness in cm, I = constant applied current in amps, and V = measured voltage in volts. A 0.5 amp current was passed through points 1 and 2, and the voltage measure through 3, and 4. This was repeated for $V_{34,12}$, $V_{23,41}$, and $V_{41,23}$ to give the total conductivity at each temperature interval.

Chapter 3

Direct Synthesis of $La_4Ni_3O_{10-\delta}$ and *In Situ* Study of the Diffusion Reaction Between $La(OH)_3$ and $Ni(OH)_2$

3.1 Aims

Hypothesis one claims that co-precipitated nano-sized precursors could be used to form the layered lanthanum nickelate, $La_4Ni_3O_{10-\delta}$ directly via a single heat-treatment and without the need for comminution due to reduced diffusion distances between the reactants. In this chapter, the direct formation of $La_4Ni_3O_{10-\delta}$ from CHFS nano-precursors in a single heat-treatment and without the need for any comminution stages was investigated. Subsequently the reaction route between $4La(OH)_3$ and $3Ni(OH)_2$ coprecipitated using CHFS was studied using *in situ* synchrotron X-ray diffraction.

3.2. Experimental Details

Two methods of synthesis were attempted in order to form $La_4Ni_3O_{10-\delta}$. The first method used continuous hydrothermal flow synthesis (which is described in chapter two) to synthesise black co-precipitated slurries of Ni and La oxide. System 1 was used and reaction conditions were 723 K and 24.1 MPa, with 0.2, 0.4, 0.6, 0.8 and 1.0 M KOH being used as the auxiliary reagent. To investigate the effect of using a CHFS coprecipitated metal hydroxide precursor (rather than oxide), the CHFS reaction temperature was set to 673 K, in this case a green slurry was collected indicating $Ni(OH)_2$ was formed. The second method was a direct coprecipitation from nitrate salts. $[La(NO_3)_3.6H_2O]$ (57 mL, 2.46 g, 0.1 M) was stirred with $[Ni(NO_3)_2.6H_2O]$ (43 mL, 1.25 g, 0.1 M), KOH (100 mL, 5.6 g, 1.0 M) was added drop wise. The solution was stirred for 10 minutes then filtered using filter paper (Fisher Scientific, QL100), the resulting green precipitate was dried on a hot-plate. Heat-treatments of the coprecipitated precursors were conducted in a CWF/1300 Carbolite muffle furnace in air, at 1348 K for 12 hours. Elemental ratios of 4.16 La and 2.84 Ni were confirmed using EDX.

Laboratory X-ray analysis was conducted using the D4 diffractometer in Bragg-Brentano geometry described in detail in chapter 2. Samples were loaded into a plastic holder, and scans were conducted in the range 20 – 70 °2θ with a 0.05° step size, 4 $s.step^{-1}$, divergence and anti-scattering slits were set to 0.5 mm.

3.2.1. In situ synchrotron measurements

The *in situ* studies were conducted at Diamond Light Source, UK, on the I11 beamline. The main set-up of the beamline and detectors is described in chapter 2. The metal hydroxide mixture with a 4La:3Ni ratio (described in the previous section) was loaded into a 0.5 mm internal diameter (ID) quartz capillary and inserted into a STOE capillary furnace which was mounted onto the *xyz* table on the beamline. In order to prevent the heating element burning out, it was necessary to evacuate the furnace and backfill with nitrogen. To maximise pO_2 content in the capillary environment the capillary end was left uncovered. The data collection strategy is described in section 2.4.4.2. The reaction was conducted using a ramp rate of 10 $K.min^{-1}$ to a holding temperature of 1448 K and data were collected continuously throughout from 0 – 474 minutes.

Data were analysed using the GSAS and EXPGUI programs.(Larson et al. 1994; Toby 2001) Quantitative refinement was performed by refining lattice parameters, background, atomic coordinates, profile parameters (for a pseudo-Vogt peak shape) and phase quantities. Zero point was set to an instrumental value using Si NIST standard reference material (srm640c).

3.3. Results and Discussion

3.3.1. Synthesis using Jet Mixer and Muffle Furnace

The synthesis of $La_4Ni_3O_{10-\delta}$ was attempted in two different ways. The first method used continuous hydrothermal flow synthesis. An aqueous mixture of 0.1 M [$La(NO_3)_3.6H_2O$] and [$Ni(NO_3)_2.6H_2O$] in a 4:3 ratio was pumped into the CHFS reactor and precipitated in a T-piece upon mixing with 1.0 M KOH. The concentration of KOH was varied to investigate the effect; concentrations were 0.2, 0.4, 0.6, 0.8 and 1.0 M. Subsequently the reaction mixture met a flow of scH_2O at 723 K and 24.1 MPa whereupon rapid nucleation and crystallisation occurred. The product was cooled in-line and collected as black slurry at *ca.* 293 K after passing

through a back pressure regulator. The total yield of La_2O_3 and NiO per 50 mL of collected slurry increased with increasing base concentration to a maximum of 63.9 % when 0.8 M KOH was used, the yield then remained approximately constant, as shown in figure 3.1. The yields observed were lower than expected, due to some loss of product during the cleaning process.

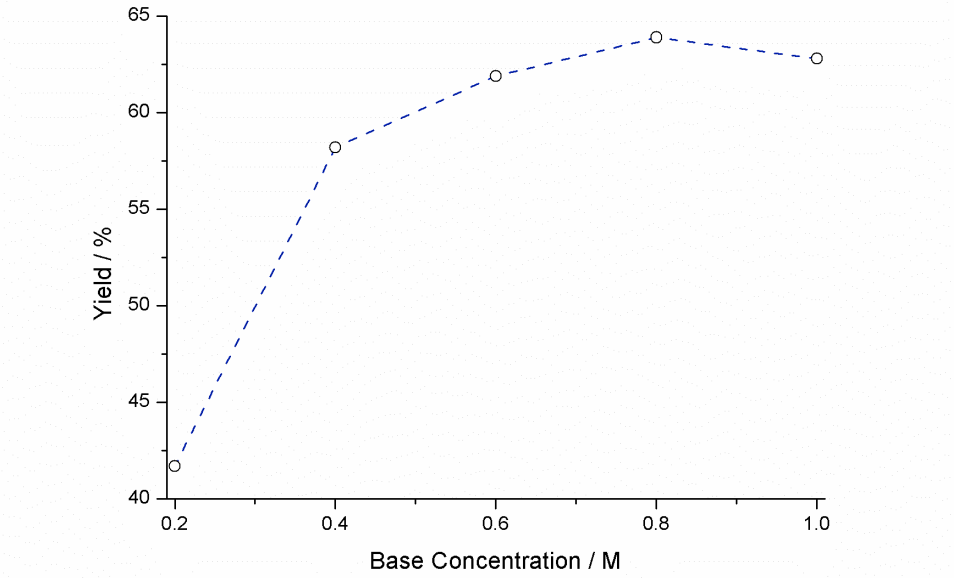

Figure 3.1. Yields of coprecipitated La_2O_3 and NiO as a function of KOH concentration. Dotted blue line is a guide to the line only.

The coprecipitates were subsequently heat-treated in air at 1348 K for 12 hours. Where KOH concentration was greater than 0.2 M, phase-pure $La_4Ni_3O_{10-\delta}$ was formed upon heat-treatment as shown in figure 3.2.

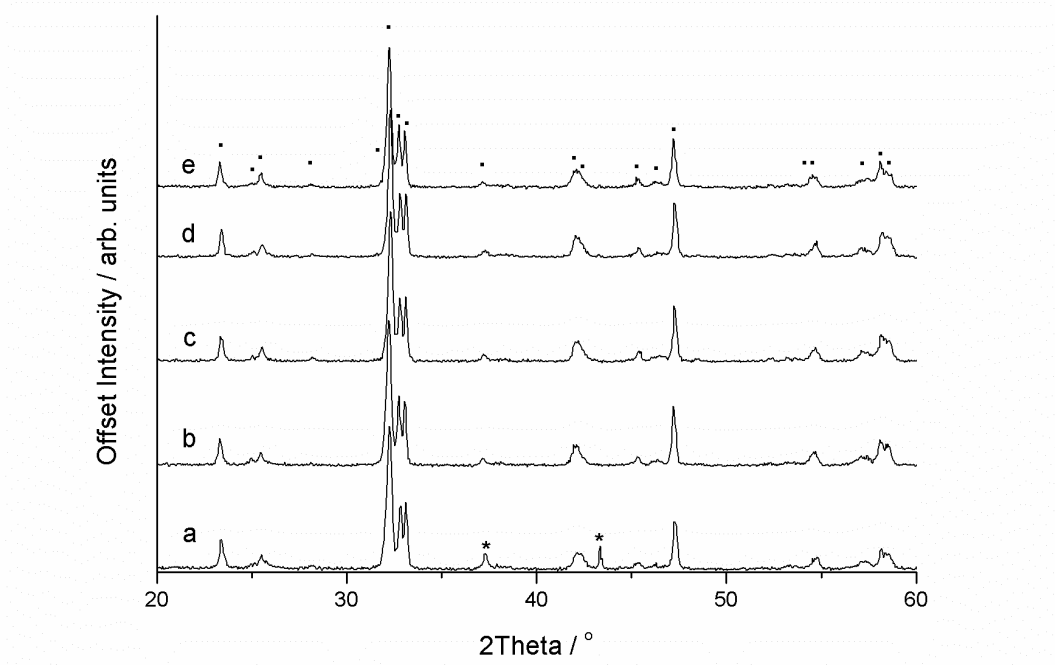

Figure 3.2. Powder X-ray diffraction patterns of the product from CHFS La_2O_3 and NiO nano-coprecipitates heat-treated at 1348 K for 12 hours. Orthorhombic peaks of the Bmab space group are marked with ■, NiO secondary phase indicated by *. KOH concentrations were a) 0.2 M b) 0.4 M c) 0.6 M d) 0.8 M and e) 1.0 M.

Figure 3.2 shows that some unreacted NiO was observed when 0.2 M base concentration was used. The NiO (200) peak at ~37 °2θ overlaps the (119) $La_4Ni_3O_{10-\delta}$ peak, which accounted for the increased intensity observed in this Bragg reflection. The low yield in this reaction (0.2 M KOH) of 41.7 % suggested that incomplete precipitation led to a non-stoichiometry in the reactants and so NiO was observed. This was confirmed using EDX spectroscopy, where the La:Ni ratio of this nano-coprecipitate was approximately 1:1. When the base concentration was greater than 0.2 M, $La_4Ni_3O_{10-\delta}$ was identified as a single phase in each case. The La and Ni content of each set of nano-coprecipitates (measured using EDX spectroscopy) is shown in table 3.1.

Table 3.1. Lanthanum and Nickel ratio, calculated using EDX spectroscopy.

[KOH] / M	La content / at%	Ni content / at%
0.2	52.53	47.47
0.4	58.61	41.38
0.6	58.43	41.59
0.8	58.01	41.99
1.0	57.86	42.14

Le Bail refinements of powder XRD data confirmed that in each case (KOH conc. > 0.2 M) $La_4Ni_3O_{10-\delta}$ crystallised in the Bmab space group. Lattice parameters were a close match to ICSD pattern 91143.(Ling et al. 1999) Figure 3.3 shows the Le Bail refinement of $La_4Ni_3O_{10-\delta}$ made using CHFS nano-coprecipitate and a 1.0 M KOH auxiliary solution. Selected refined parameters are displayed in table 3.2.

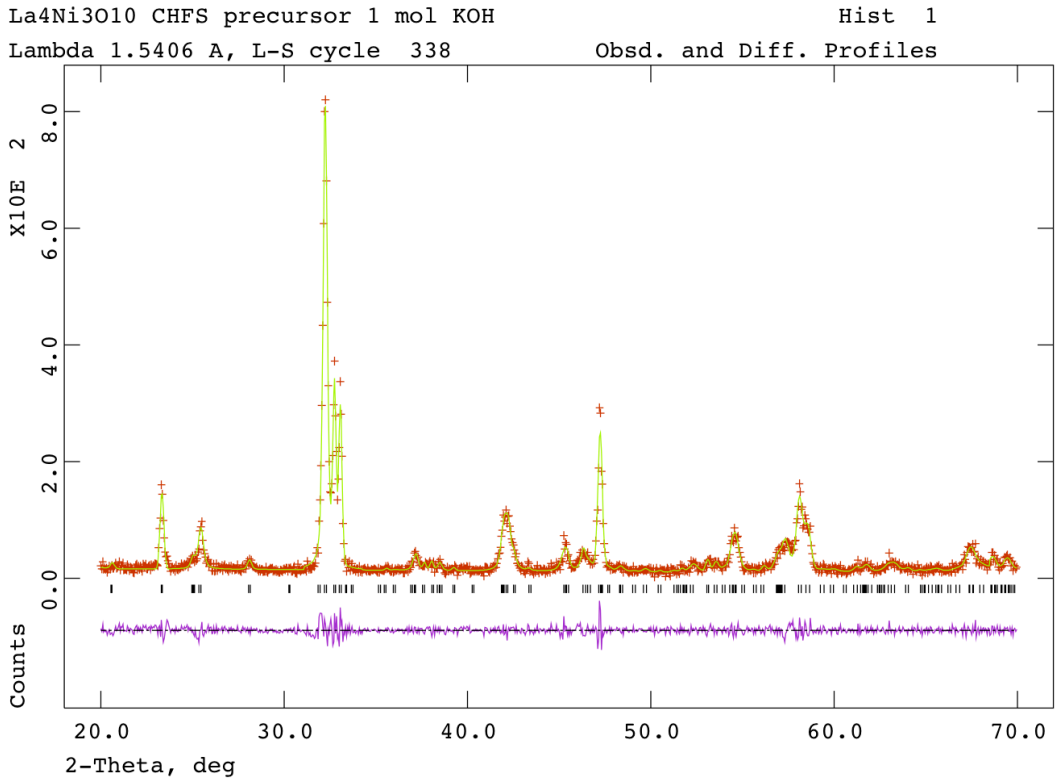

Figure 3.3. Le Bail refinement of $La_4Ni_3O_{10-\delta}$ formed from coprecipitated CHFS nano-precursors using 1.0 M KOH. Experimental data are marked with red crosses, the calculated model is given by the continuous green line, and the difference is displayed in purple. Tick marks are for the Bmab space group. $\chi^2 = 1.308$.

Table 3.2. Selected refined parameters for $La_4Ni_3O_{10-\delta}$ made using 1.0 M KOH from CHFS coprecipitated lanthanum and nickel oxides and hydroxides. Literature data is taken from (Ling et al. 1999), values are calculated from Reitveld refinement of powder neutron diffraction data.

—	Oxide Precursors	Hydroxide Precursors	Ling *et al.*
Space group	Bmab	Bmab	Bmab
a	5.4097(9) Å	5.4094(9) Å	5.41327(11) Å
b	5.4718(8) Å	5.4597(8) Å	5.46233(11) Å
c	27.988(4) Å	28.021(6) Å	27.9605(7) Å
Volume	828.5(3) $Å^3$	827.6(4) $Å^3$	826.77 $Å^3$
Crystallite size $\perp$	78(3) nm	149(12) nm	—
Crystallite size $\parallel$	35(2) nm	17(1) nm	—

The model was significantly improved by introducing an anisotropic crystallite size, [χ^2 = 1.768 (isotropic) → χ^2 =1.308 (anisotropic)] giving a perpendicular size dimension of 78 nm and a parallel size dimension 35 nm. This size anisotropy suggested a needle-like crystallite.

CHFS reactor temperature was reduced to 673 K to produce lanthanum and nickel hydroxides in a 4:3 ratio. Heat-treatment of these precursors at 1348 K for 12 hours also produced $La_4Ni_3O_{10-\delta}$ the results of which are also presented in table 3.2 for comparison. SEM images of $La_4Ni_3O_{10-\delta}$ synthesised from oxides, figure 3.4a and synthesised from hydroxides, figure 3.4b show no large differences. Both compounds appear to be formed of micron-sized agglomerated particles. Due to the agglomeration no evidence of the proposed needle-shaped crystallites was observed.

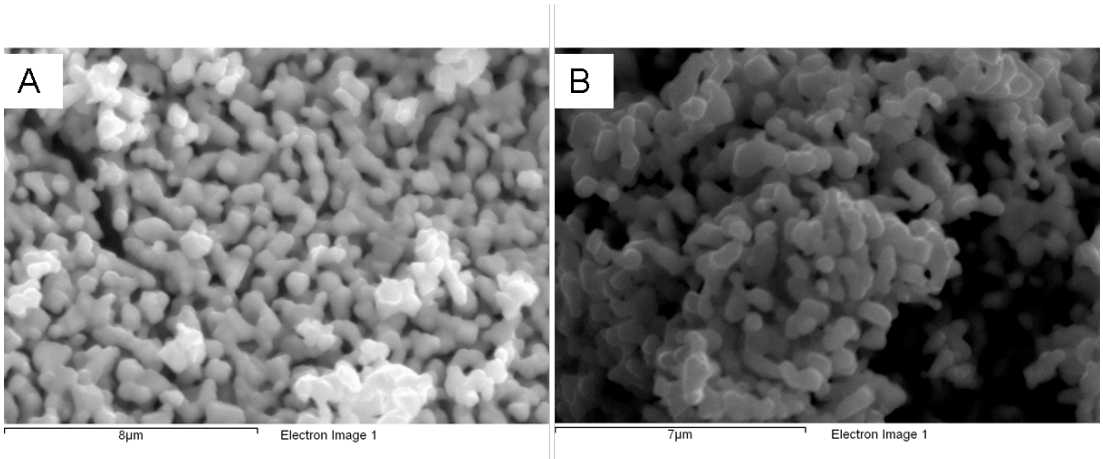

Figure 3.4. SEM image of $La_4Ni_3O_{10-\delta}$ synthesised from a 12 hour heat-treatment of CHFS nano-coprecipitates. A.) $La_4Ni_3O_{10-\delta}$ from oxide nano-precursors. B.) $La_4Ni_3O_{10-\delta}$ from hydroxide nano-precursors.

The anisotropy in $La_4Ni_3O_{10-\delta}$ synthesised from hydroxide nano-precursor was greater than when using oxide nano-precursors. This was highlighted by the large difference between the ⊥ and ‖ crystallite size of 132 nm compared to just 43 nm in the oxide nano-precursor sample. The difference in anisotropy suggested the mass transfer was incomplete after 12 hours when using hydroxide nano-precursors and a longer reaction time was needed to create a well ordered crystallite.

The second method attempted was a direct coprecipitation method of metal hydroxides from their respective nitrate salts. An aqueous mixture of $[La(NO_3)_3.6H_2O]$ and $[Ni(NO_3)_2.6H_2O]$ in a 4:3 ratio (0.1 M) was mixed and added to an equal volume of 1.0 M KOH. The mixture was stirred for 10 minutes during which time precipitation of a green solid was observed which was an amorphous mixture of $La(OH)_3$ and $Ni(OH)_2$. The precipitate was filtered and oven dried at 373 K for 12 hours to give a total yield of 58.5 %. Following heat-treatment at 1348 K for 12 hours in air, a black power was obtained that was identified as a mixture of $La_4Ni_3O_{10-\delta}$, NiO and an unidentified phase using powder XRD, shown in figure 3.5. A precipitation time of 10 minutes was not sufficient to ensure complete precipitation of the all of precursor; the 58.5 % yield supported this hypothesis.

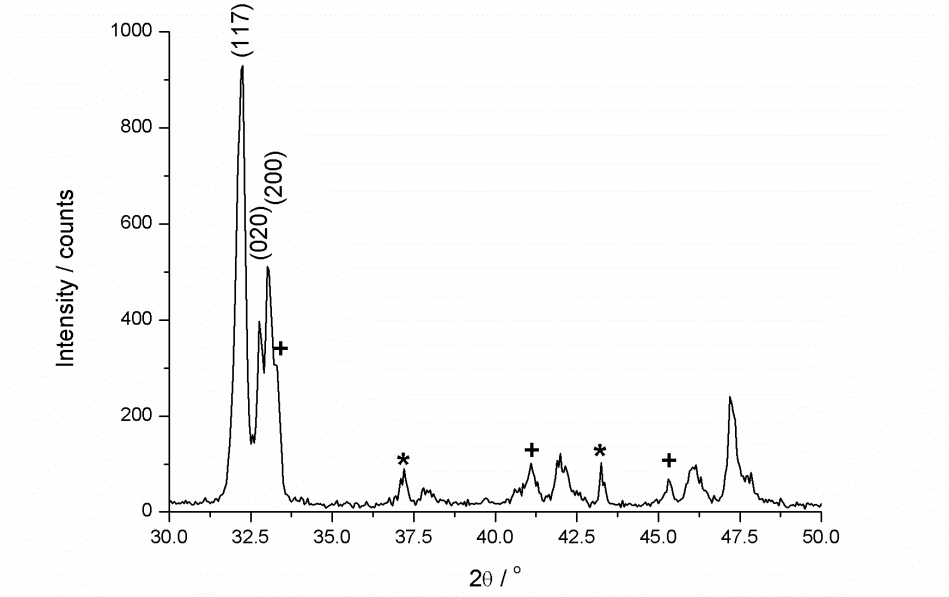

Figure 3.5. PXRD pattern of $La_4Ni_3O_{10-\delta}$ synthesised at 1348 K for 12 hours from metal nitrate precursors made using the direct coprecipitation method. * = NiO reflections, + = unidentified reflections.

3.3.2. *In-situ* synthesis of $La_4Ni_3O_{10-\delta}$

3.3.2.1. 0 – 78 minutes

Lanthanum and nickel hydroxide precursors in a 4La:3Ni ratio, were made using manual CHFS reactor one (described in chapter 2) using 1.0 M base to ensure complete precipitation and the correct stoichiometry in the nano-precursor. The nano-precursors were green in colour, visually confirming that metal hydroxides had been formed. The metal ratio was confirmed using EDX spectroscopy as 4.16 La : 2.84 Ni, and SEM indicated that very small grains had been formed as shown in figure 3.6.

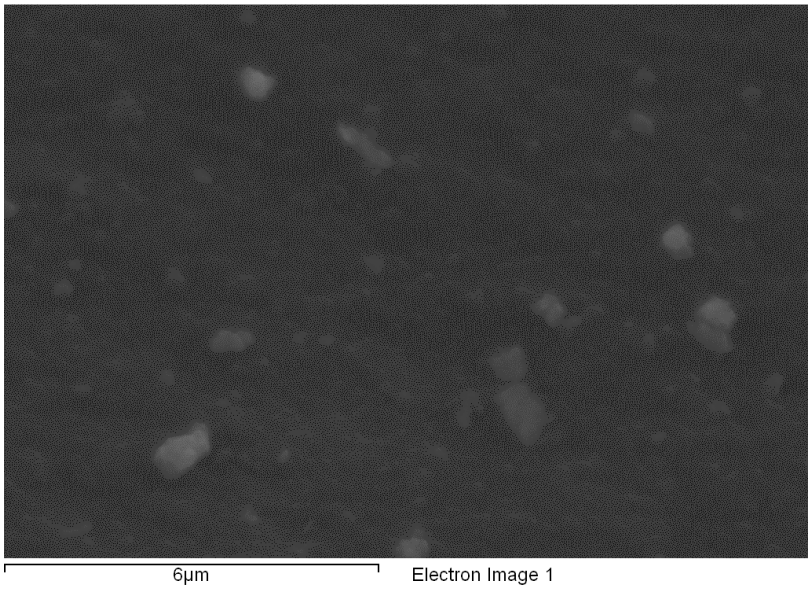

Figure 3.6. SEM image of a mixture of $La(OH)_3$ and $Ni(OH)_2$ synthesised using CHFS .

The $La(OH)_3$ crystallite size was approximately 9 nm estimated using the Scherrer equation, no Bragg peaks for $Ni(OH)_2$ were observed at this point suggesting that it was amorphous. Large broad background features in the X-ray powder diffraction pattern supported this hypothesis. The nano-precursors were loaded into a quartz capillary (0.5 mm I.D.) and placed into a capillary furnace.

120 second scans were collected using the MAC detector on the I11 beamline at Diamond Light Source, a further 60 seconds was required for the MAC detector to return to its original position. Therefore each scan was 180 seconds total. Scans were

collected continuously for the duration of the experiment. The ramp rate was set a 10 K.min^{-1} meaning each scan amounted to a 30 K difference from start to finish.

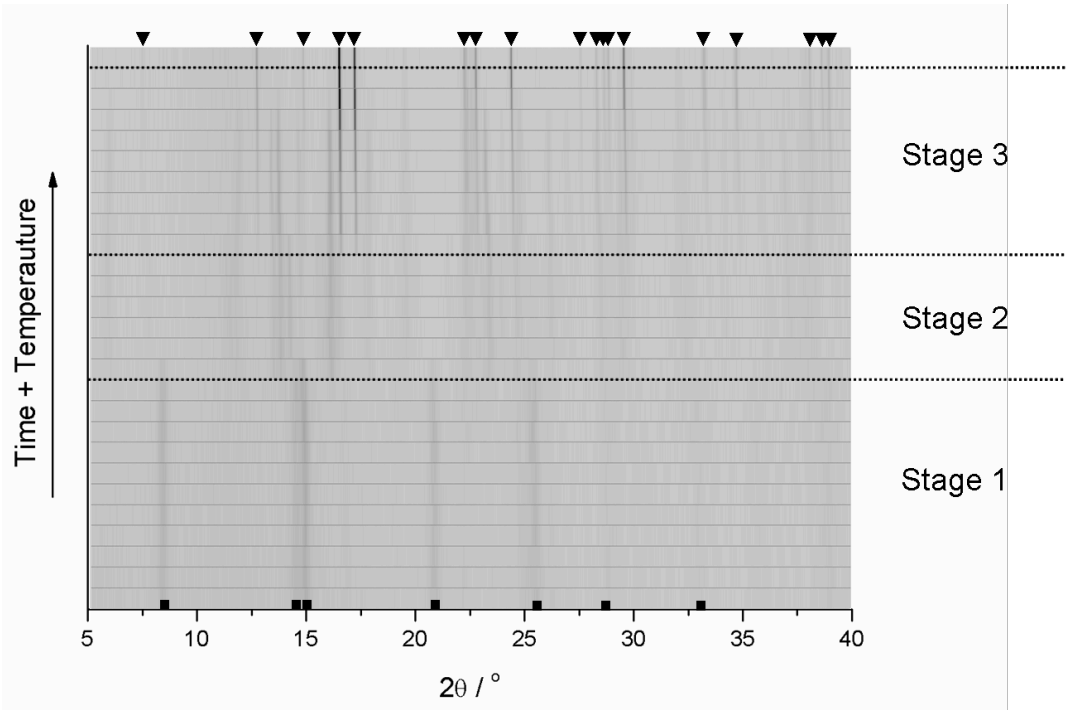

Figure 3.7. Diffraction patterns collected in the range 0 – 78 minutes, and 315 – 1133 K. Stages 1, 2 and 3 are described in the text below and represent the different stages of the reaction. ■ = $La(OH)_3$ reflections, ▼ = $La_2NiO_{4+\delta}$ reflections.

Figure 3.7 represents the region of the reaction in which the reactants were nanosized, which is in the range 0 – 78 minutes and 315 – 1133 K. During stage one (range 0 – 33 minutes, 315 – 660 K) the diffraction patterns appeared to be $La(OH)_3$ alone. Broad features in the background suggested that $Ni(OH)_2$ was amorphous at this stage.

Stage two, which was in the range 33 mins. – 51 mins. and 660 – 850 K, saw the gradual dehydration of the hydroxide precursors; mixtures of nanosized La_2O_3, LaOOH, and NiO were identified. The presence of the LaOOH species suggests dehydration of the hydroxides to oxides. Bragg reflections of all components were broad during this stage indicating a nano crystallite size, or amorphous mixture. This suggested that the mechanism was similar to that described in figure 1.11 (section 1.3.1) described by Novet *et al.* and Fister *et al*. in which the reaction proceeds through an amorphous intermediate and nucleation becomes the rate limiting step.(Fister et al. 1992; Novet et al. 1991) Some Bragg reflections were still observed however, which showed some interfacial diffusion was still occurring.

During stage three (range: 51 mins. – 78 mins., 850 K – 1133 K) , nucleation and growth of the $La_2NiO_{4+\delta}$ crystallite occurred. $La_2NiO_{4+\delta}$ was first observed at 51 minutes and continued to grow until 78 minutes (1133 K). By 78 minutes the La_2O_3 Bragg reflections had disappeared leaving a mixture of $La_2NiO_{4+\delta}$ and NiO as shown in figure 3.8 indicating that interfacial diffusion of the Ni and La species was complete.

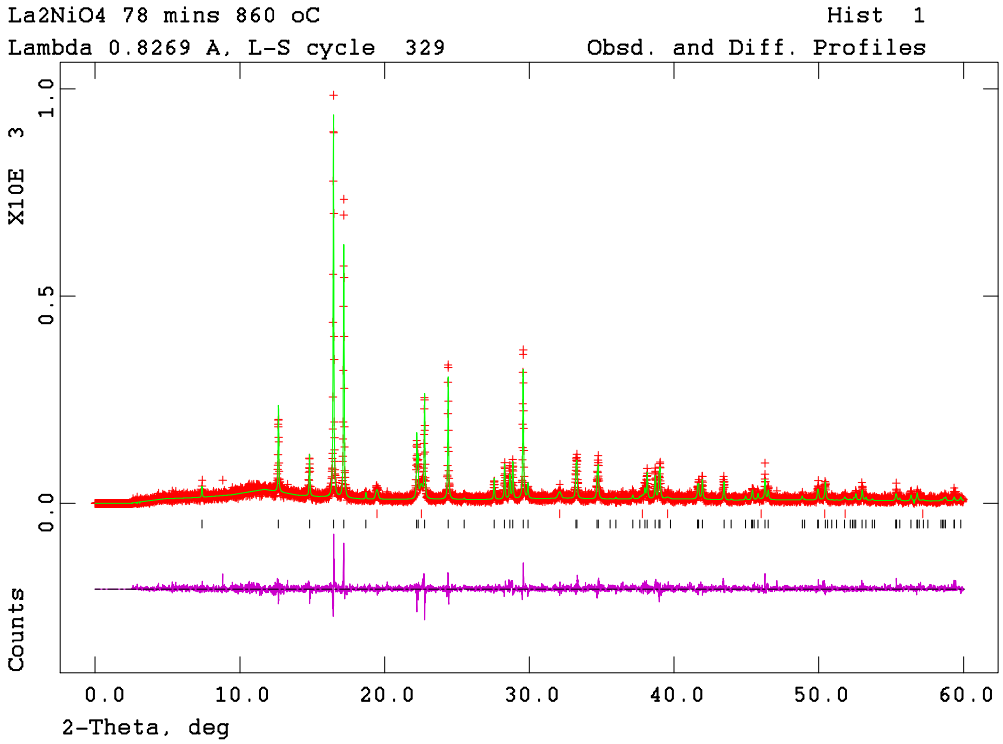

Figure 3.8. Rietveld refinement of the diffraction pattern recorded at 78 minutes and 1133 K. Experimental data is given by red crosses, green line is the model and the purple line is the difference curve. Tick marks are for NiO (upper) and $La_2NiO_{4+\delta}$ (lower). $\chi^2 = 1.621$, $R_{wp} = 0.2766$ $R_p = 0.2068$.

This route to $La_2NiO_{4+\delta}$ was in agreement with a previous investigation using CHFS precipitated hydroxides that was studied using laboratory X-ray diffraction.(Weng et al. 2011) The same study however found that $La_2NiO_{4+\delta}$ was not an intermediate phase in the formation of $La_4Ni_3O_{10-\delta}$ in disagreement with this work. (Weng et al. 2011) The presence of a small amount of NiO that remained was due to the stoichiometry of the precursor which was 4La:3Ni as shown in equation 3.1.

$$4La(OH)_3 + 3Ni(OH)_2 \xrightarrow{\Delta} 2La_2NiO_{4+\delta} + NiO \quad \textbf{(3.1)}$$

Refined values of $La_2NiO_{4+\delta}$ identified at 78 minutes (1133 K) are listed in table 3.3. Quantitative analysis of the X-ray data suggested that the wt% of the $La_2NiO_{4+\delta}$ and the NiO phases at this point were *ca*. 90 and 10 wt% respectively. This refined value approximately equated to a mass ratio of $2La_2NiO_{4+\delta}$:NiO (801.0:74.7 g.mol^{-1}, 90.6:9.3 wt%) further confirming the hypothesis that the presence of NiO was stoichiometric.

Table 3.3. Crystallographic parameters for obtained from Rietveld refinement of the powder diffraction pattern collected at 78 minutes, 1133 K.

Space Group	*I/4mmm*
a	3.91373(7) Å
c	12.8177(4) Å
volume	196.334(7) Å^3
La *00z*	0.3602(1)
100*U_{iso}	1.20(7)
$La_2NiO_{4+\delta}$ fraction	89.8(1) wt%
NiO fraction	10.2(7) wt%
$La_2NiO_{4+\delta}$ Crystallite Size	66 nm

Crystallite size was measured using the Scherrer equation via measurement of the Gaussian peak width of the (010) reflection of $La(OH)_3$ and the (103) reflection of $La_2NiO_{4+\delta}$ during stage three. The sample contribution to the Gaussian peak width was found by equation 3.2:

$$G^2_{sample} = G^2_{Total} - G^2_{instrument} \quad \textbf{(3.2)}$$

Where G is the Gaussian full width half maximum (FWHM), the instrumental Gaussian broadening was calculated using a Si standard (NIST srm640c) (111) reflection. Due to the multiphase and amorphous nature during stage two, a single peak with no overlapping reflections was not found. The crystallite size of $La(OH)_3$ did not grow during stage one and remained constant between 10 and 15 nm. From the amorphous intermediate, (*ca.* 35 – 50 mins.) nucleation of the $La_2NiO_{4+\delta}$ crystallite occurred. The crystallite size of $La_2NiO_{4+\delta}$ grew linearly through stage

three as shown in figure 3.9, as a result of the diffusion of La_2O_3 and NiO.

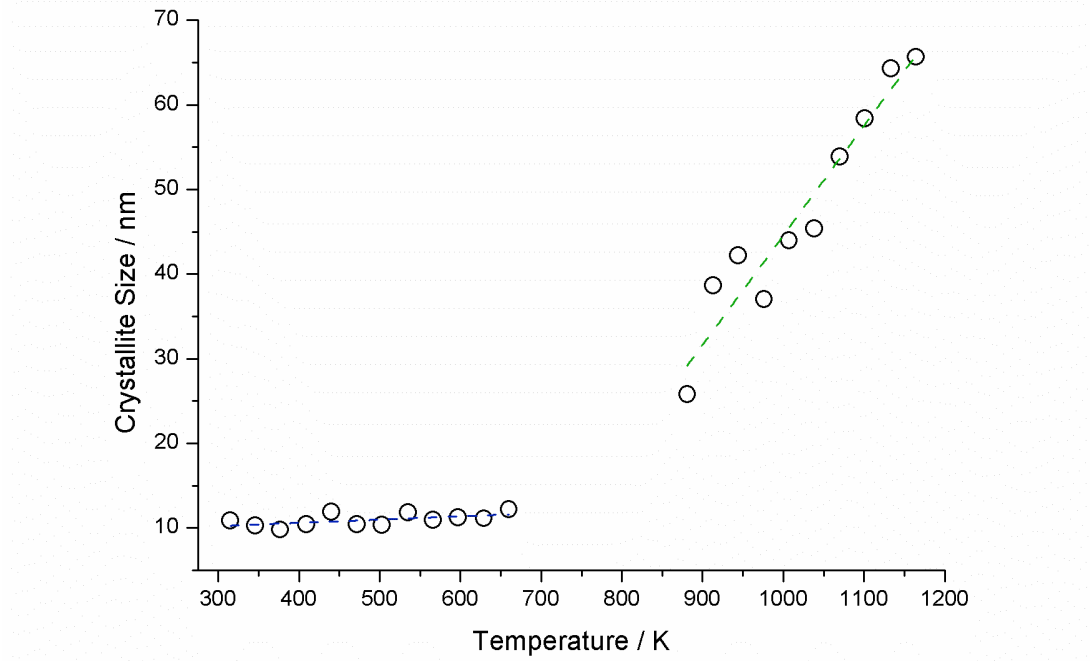

Figure 3.9. Graph showing evolution of crystallite size over time calculated using the Scherrer equation. The blue dotted line represents the values calculated from measurements of (010) reflection of $La(OH)_3$ during stage one. The green dotted line is fitted to values calculated from the (103) reflection of $La_2NiO_{4+\delta}$ during stage 3.

It was inferred that the energy required for nucleation of $La_2NiO_{4+\delta}$ was given by the point at which the green line in figure 3.9 intercepts the *x* axis, which equated to a temperature of 640 K. To test this hypothesis, $2La(OH)_3$ and $Ni(OH)_2$ co-precipitates using CHFS were reacted at 673 K for 240 hours in an electric muffle furnace. The resulting powder X-ray diffraction pattern showed low crystallinity mixture of reactants that could not be identified due to the broad low intensity peaks present (figure 3.10). Given the low intensity and quantity of broad reflections it was not possible to identify the reaction mixture using powder X-ray diffraction alone. Far greater than 240 hours was required to complete the reaction at 673 K if it could be completed at this temperature.

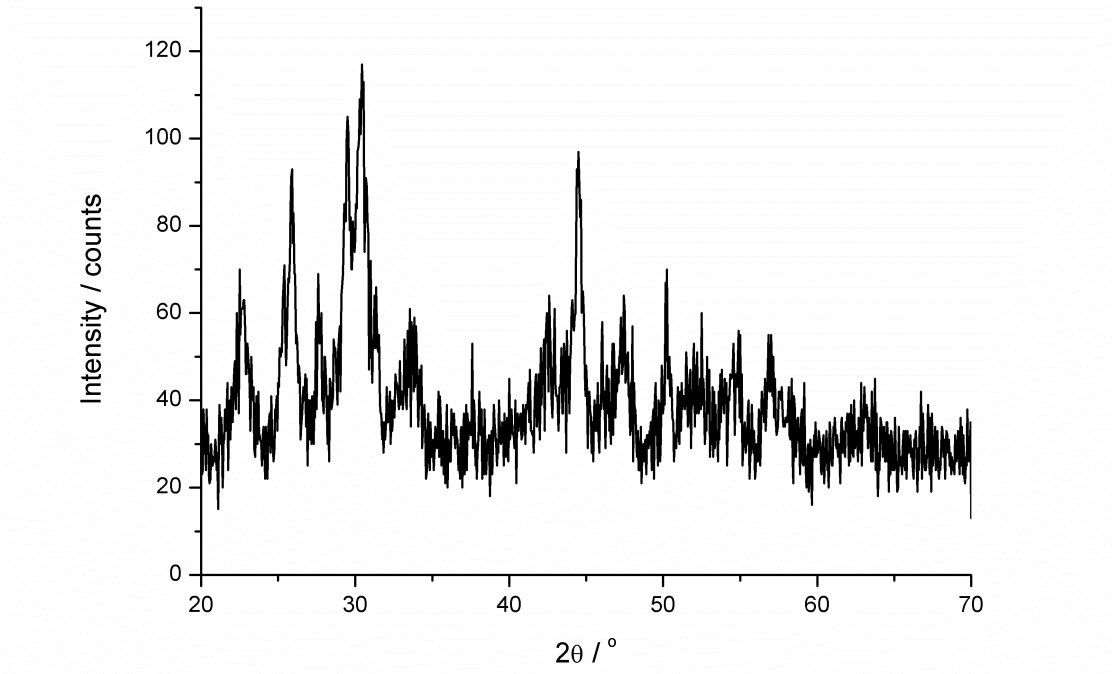

Figure 3.10. Powder X-ray diffraction pattern of products formed from 240 hour reaction of $2La(OH)_3$ and $Ni(OH)_2$ at 673 K.

3.3.2.2. 78 – 108 minutes

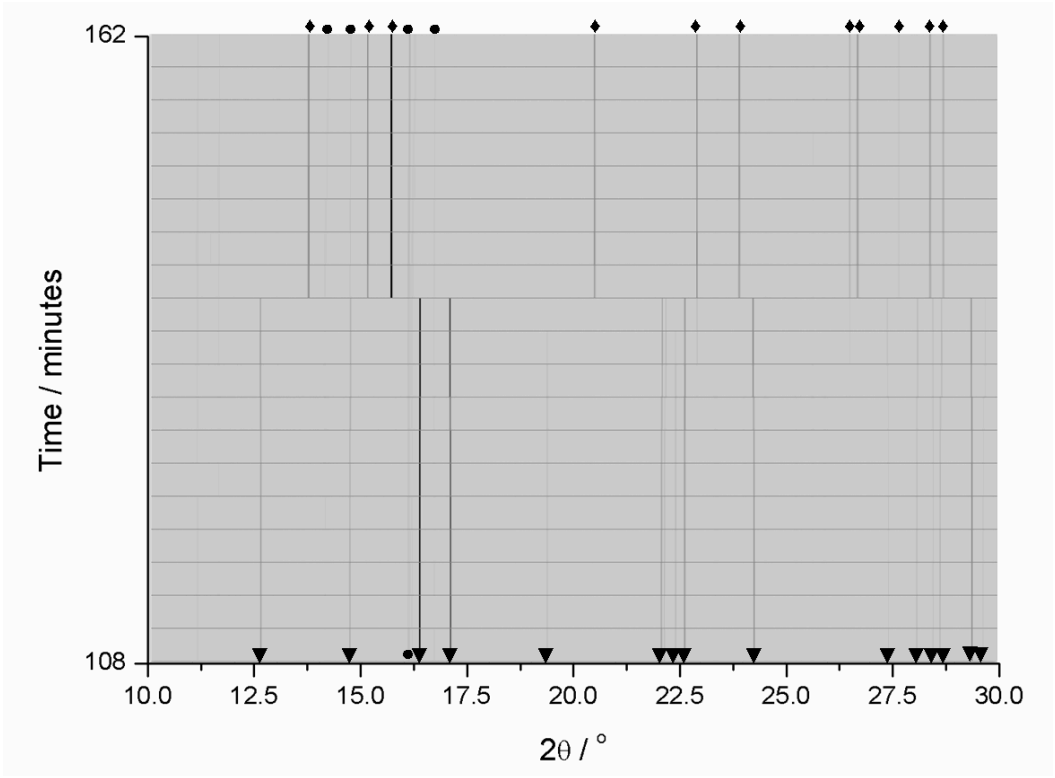

Figure 3.11. Powder X-ray diffraction patterns collected between 108 and 162 minutes at 1348 K. ▼ = $La_2NiO_{4+\delta}$, ● = UnK1 phase, ♦ = La_2O_3.

After 141 minutes, 1448 K, a rapid phase change occurred as shown in figure 3.11. The $La_2NiO_{4+\delta}$ phase decomposed to leave a mixture of La_2O_3, and NiO and an unknown phase (UnK1). This unknown phase had been observed before the phase decomposition from 87 minutes and 1227 K, showing that its formation was via diffusion based first order phase transition. Diffusion between $La_2NiO_{4+\delta}$ crystallites resulted in nucleation and then growth of the UnK1 at the interfaces.

3.3.2.3. 108 – 474 minutes

The heat-treatment was stopped after 474 minutes when no further change in the structure appeared to be occurring. However, subsequent analysis revealed that over the period of 345 – 462 minutes the intensity of the UnK1 Bragg peaks increased and the intensity of the La_2O_3 and NiO Bragg peaks declined which suggested that the reaction was in fact continuing as shown by figure 3.12.

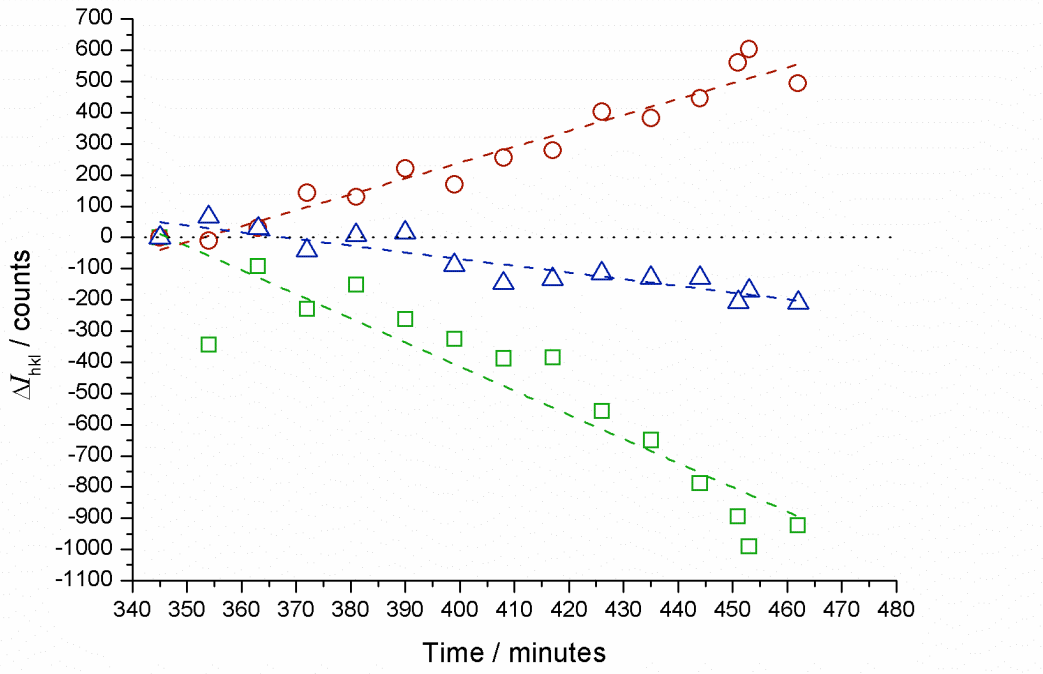

Figure 3.12. ΔI_{hkl} between 345 – 462 minutes. Red circles and dotted red line indicates the UnK1 phase. Blue triangles and dotted blue line indicates NiO, and green squares and dotted green line indicate La_2O_3.

The final scan (474 minutes, 1448 K) was a mixture of La_2O_3, NiO and UnK1, the UnK1 reflections were indexed using the TREOR90 program. The result produced a hexagonal cell in which the first 20 reflections were indexed to: $a = 9.8393$ Å, $b = 9.8393$ Å, $c = 7.2690$ Å, GOF = 80. Given the largely

orthorhombic nature of the Ruddlesden-Popper $La_{n+1}Ni_nO_{3n+1}$ phases, it was assumed that this was a pseudo-hexagonal cell, which was converted to orthorhombic by equation 3.3:

$$b*(\sqrt{3}) \qquad \textbf{3.3}$$

Giving an orthorhombic cell of: a = 9.8393 Å, b = 17.0422 Å, c = 7.2690 Å. The space group was found to be Fcna from systematic absences. Le Bail refinement demonstrated that this space group was a good fit to the data, shown in figure 3.13.

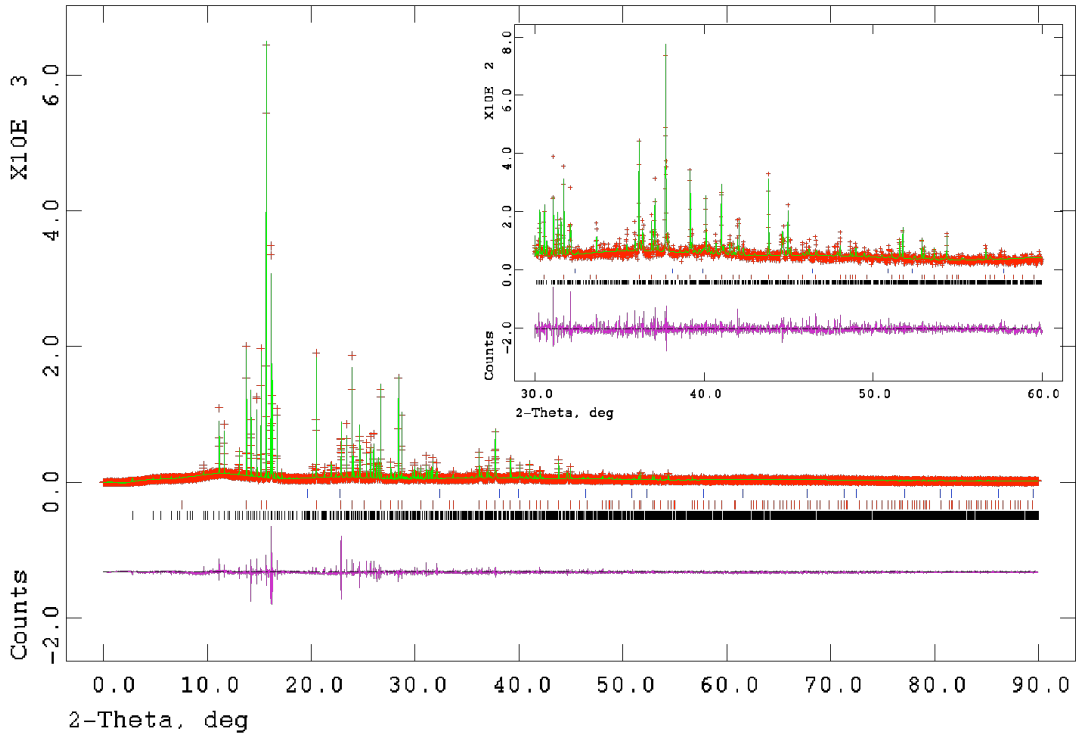

Figure 3.13. Le Bail refinement of collected after 474 minutes and at 1448 K. Red crosses indicate observed data, the continuous green line indicates the model, and the purple line indicates the difference. Blue tickmarks are rhombohedral NiO, red tickmarks are La_2O_3, black tickmarks are the Fcna phase. χ^2 = 3.761, R_{wp} = 0.2510, R_p = 0.1798. **Inset:** Highlighted high-angle data, 30 – 60 °2θ.

Rietveld refinement was attempted using potential isostructural compounds, however no match was found. The high symmetry meant that simulated annealing was inappropriate for this structure, as a result the atomic structure was not found. Unit cell information for the Fcna phase extracted from the Le Bail refinement is displayed in table 3.4.

Table 3.4. Refined unit cell values for the Fcna phase.

Space Group	Fcna
a	9.8383(3)
b	17.0304(3)
c	7.2667(2)
Volume	1217.53(4)
χ^2	3.761

The long *c* axis of the Fcna phase was approximately that of $La_3Ni_2O_{7-\delta}$ 20.5 Å. It was therefore assumed that the Fcna phase was an intermediate lanthanum nickelate that had a similar structure to $La_3Ni_2O_{7-\delta}$ without the defined layered structure of the Ruddlesden-Popper type oxides. Further reaction with La_2O_3 and NiO was therefore required to produce $La_4Ni_3O_{10-\delta}$.

The inability to form $La_4Ni_3O_{10-\delta}$ in the duration of the experiment can be explained by work of Palcut *et al*. who calculated the diffusion coefficient in the formation of $LaCoO_3$ and La_2CoO_4. (Palcut et al. 2007) They found that the diffusion coefficientt of Co was proportional to the partial pressure of oxygen, pO_2. It was assumed therefore that the low pO_2 in the capillary reduced the diffusion rate of nickel and hence increased reaction time. The changing intensities between La_2O_3, NiO and the unknown orthorhombic phase suggested that the reaction was continuing at 1448 K and therefore may not have been complete after 7 hours 54 minutes in this case. By increasing pO_2, perhaps by using a gas-flow cell it may have been possible to complete the reaction.

The total sets of equations for the entire reaction were as follows:

$$4La(OH)_3 + 3Ni(OH)_2 \xrightarrow{\Delta} 3NiO + 2LaOOH + La_2O_3 + xH_2O \rightarrow 4La_2O_3 + 3NiO \quad \textbf{(3.4)}$$

Equation 3.4 represents the gradual formation of the amorphous intermediate and completion of the majority of interfacial diffusion occurring during 0 – 51 minutes and 315 – 850 K.

$$4La_2O_3 + 3NiO \rightarrow 2La_2NiO_{4+\delta} + NiO \qquad \textbf{(3.5)}$$

Equation 3.5 represents the nucleation and growth of the $La_2NiO_{4+\delta}$ from the largely amorphous intermediate. Nucleation of the unknown orthorhombic phase (UnK1)

occurred as a result of diffusion between $La_2NiO_{4+\delta}$ crystallites shown in equation 3.6.

$$2La_2NiO_{4+\delta} + NiO \rightarrow UnK1 \quad \textbf{(3.6)}$$

At 141 minutes at 1448 K a rapid decomposition of $La_2NiO_{4+\delta}$ was observed that can be described by equation 3.7.

$$2La_2NiO_{4+\delta} + NiO + UnK1 \rightarrow xLa_2O_3 + yNiO + zUnK1 \quad \textbf{(3.7)}$$

It is assumed that the reaction then proceeded via equation 3.8.

$$xLa_2O_3 + yNiO \rightarrow\rightarrow zUnK1 \quad \textbf{(3.8)}$$

If continuation of the reaction were to lead to $La_4Ni_3O_{10-\delta}$ this result would represent an alternative route than has been previously observed.(Weng et al. 2011)

3.4. Conclusions

In conclusion, anisotropic crystallites of $La_4Ni_3O_{10-\delta}$ could be formed from a single 12-hour heat-treatment of co-precipitated CHFS precursors, which is an order of magnitude faster than a heat and grind synthesis supporting hypothesis 1. It is believed that this increased reaction rate was due to shorter diffusion distances as a result of using a coprecipitated nano-precursor. When the reaction was followed *in situ* using synchrotron diffraction it was found that $La_4Ni_3O_{10-\delta}$ could not be formed after a 7 hour 54 minute heat-treatment. This was assumed to be due to slower Ni diffusion as a result of the low partial pressure of oxygen in the capillary. However it was possible to synthesise $La_2NiO_{4+\delta}$ in 78 minutes at 1133 K, which was 4.6 times faster and at a 140 K lower temperature than when using a traditional heat and grind approach, in which a 6-hour heat treatment is required at 1273 K often with regrinding stages. This result demonstrated the potential for the formation of heterometallic layered metal oxides from CHFS nano-precursors, in which lower energy syntheses could be achieved and confirmed hypothesis 1.

Chapter 4

High-Throughput Synthesis of Doped $La_4Ni_{2.7}M_{0.3}O_{10-\delta}$ (where M = V, Cr, Mn, Fe, Co, Cu, and Al)

4.1. Aims

Hypothesis two predicted firstly that by using CHFS nano-precursors, the time taken to synthesise doped lanthanum nickelates might be shortened, and secondly that this might be achieved more efficiently by using high-throughput continuous hydrothermal (HiTCH) flow synthesis. In this chapter the use of a HiTCH flow synthesis reactor was investigated in an effort to synthesise a range of metal doped lanthanum nickelates ($La_4Ni_{2.7}M_{0.3}O_{10-\delta}$ where M = V, Cr, Mn, Fe, Co, Cu and Al). Also the feasibility of splitting precursor libraries into daughter libraries that could then be heat-treated at different temperatures in parallel was explored. The aim was to optimise reaction conditions and compositions quickly for the mapping of phase diagrams.

4.2. Experimental Details

4.2.1. Source Materials

The source materials: $[La(NO_3)_3.6H_2O]$ (99.9 %), $[Ni(NO_3)_3.6H_2O]$ (99.9 %) $[V(SO_5).5H_2O]$ (99.9 %), $[Cr(NO_3)_3.9H_2O]$ (99.9 %), $[Mn(NO_3)_2.4H_2O]$ (99.9 %), $[Fe(NO_3)_3.9H_2O]$ (99.9 %), $[Co(NO_3)_2.6H_2O]$ (99.9 %), $[Cu(SO_4).5H_2O]$ (99.9 %), and $[Al(NO_3)_3.9H_2O]$ (99.9 %) were supplied by Sigma-Aldrich Chemical Company (Dorset, UK). KOH pellets (≥85 %) were supplied by Fisher Scientific Chemical Company (Loughbourough, UK). All experiments were conducted using deionised water (10 MΩ) throughout.

4.2.2. Syntheses of Nanosized Precursor Co-precipitates Using a HiTCH Flow Synthesis Reactor

All nanosized precursors were made using CHFS system 2 (described in section 2.1.2) with pump rates of 20.0, 10.0 and 10.0 $mL.min^{-1}$ for the scH_2O, metal nitrate and KOH feed, respectively. Each composition was made at 450 °C and 24.1 MPa. Once synthesised, each nano-precursor composition was centrifuged,

washed and freeze dried as explained in chapter 2. The method of cleaning the reactor between samples to prevent contamination is described in chapter 2. Each nano-precursor sample was split into three to create three daughter libraries. Daughter libraries were then heat-treated in a Carbolite CWF 13/5 muffle furnace at 1348 K, 1448 K and 1548 K in air with a ramp rate of 10 $K.min^{-1}$, and a holding time of 12 hours.

4.2.3. Analytical Techniques

Structural characterisation data were collected using the D4 diffractometer described in chapter two. This diffractometer had an automated sample changer that was used to increase throughput and allow multiple data sets to be collected in turn. For selected samples, data were collected on the D500 diffractometer using monochromatic $CuK\alpha_1$ radiation (step size was 0.02° and count time was 10 $s.step^{-1}$). GSAS and EXPGUI programs were used for unit cell refinement and microstructural analysis.(Larson et al. 1994; Toby 2001)

DC conductivity was measured using an in-house built 4-point DC probe. Data were collected at 50 K steps in the temperature range 295 – 1173 K.

4.3. Results and Discussion

4.3.1. High-Throughput Synthesis

Increase in metal valence towards M(III) on the $Ln_{n+1}M_nO_{3n+1}$ B-site has been shown to increase M 3*d* and O 2*p* orbital hybridisation and subsequently increase DC conductivity as a result.(Sreedhar et al. 1994; Zhang et al. 1995) Dopants were selected therefore to introduce a small increase in M(III) content on the $La_4Ni_3O_{10-\delta}$ Ni-site. Dopant concentration was kept at 10 at% dopant on the Ni site to prevent large amounts of hole doping in the valence band. Eight nano-precursor slurries were synthesised using a manual HiTCH flow synthesis reactor (described in section 2.1.2) to form a library. The library was then split into three to form three identical daughter libraries. Each daughter library was then heat-treated in parallel at 1348 K, 1448 K, and 1548 K, respectively for 12 hours in air to bring about solid-state transformations from the nano-precursors. The stages that formed the high-throughput methodology are displayed in figure 4.1.

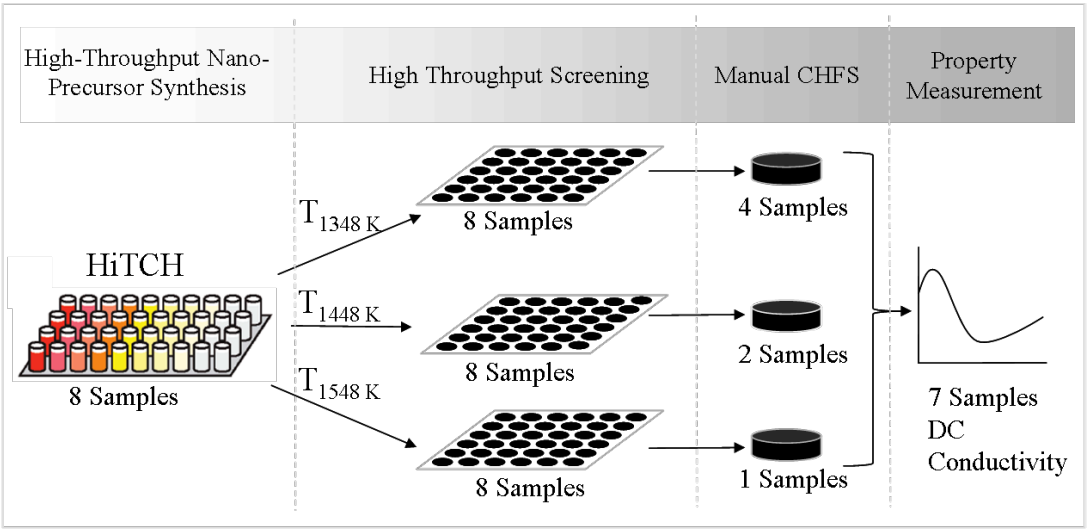

Figure 4.1. Work-flow diagram representing the stages involved in the high-throughput process.

4.3.2. Structural Screening using X-Ray Diffraction

An automated sample changer was used to rapidly collect all the powder X-ray diffraction (PXRD) data. The phases formed in each case are shown in a phase diagram in figure 4.2.

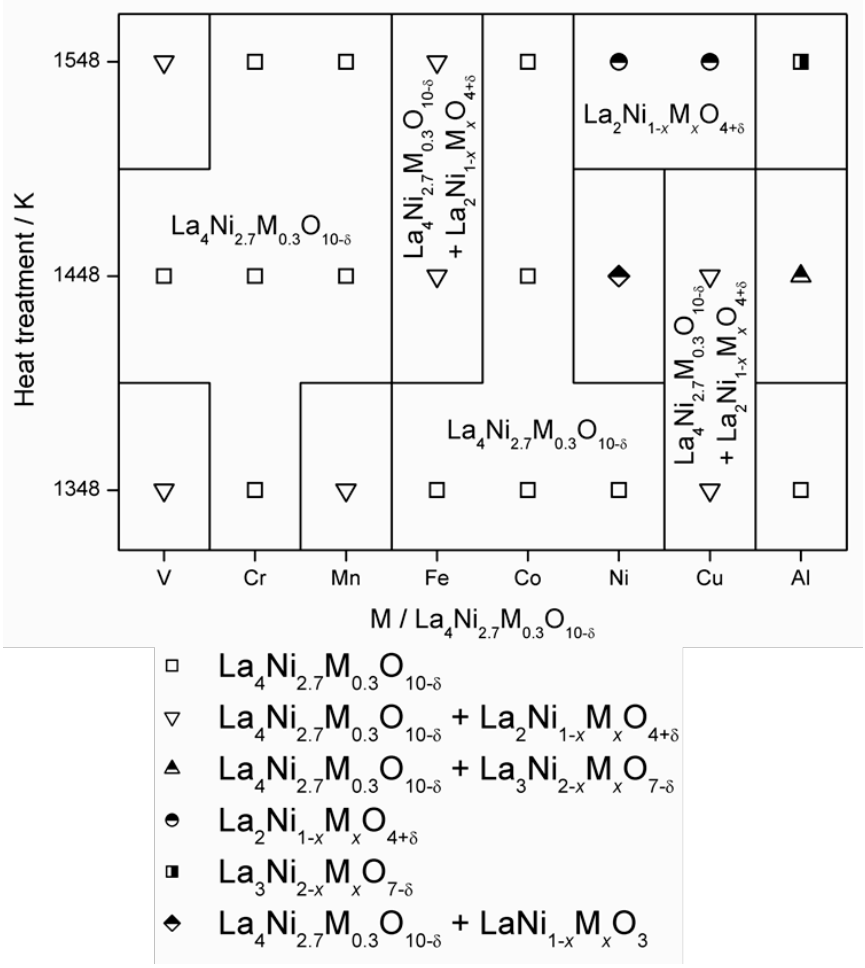

Figure 4.2. Phase diagram at atmospheric temperature and pressure for doped lanthanum nickelates synthesised at 1348, 1448, and 1548 K. Each point along the *x*-axis represents a different composition, and each point along the *y*-axis represents a different heat-treatment.

It was possible to quickly identify that the Ruddlesden-Popper phase $La_4Ni_{2.7}M_{0.3}O_{10-\delta}$ could be synthesised for all dopants except Cu at 10 at% M on Ni sites and in the temperature range 1348 – 1548 K. The strong $La_2Ni_{1-x}Cu_xO_{4+\delta}$ reflections suggested that it had formed favourably and Cu was in a +2 oxidation state, $La_4Ni_3O_{10-\delta}$ therefore could not electronically accommodate a M(II) dopant.

The most readily formed and stable $La_4Ni_{2.7}M_{0.3}O_{10-\delta}$ compounds were when M = Cr and Co, which were observed over the entire temperature range1348 – 1548 K. Where M = V, Fe and Al, $La_4Ni_{2.7}M_{0.3}O_{10-\delta}$ was only formed at either 1348 K or 1448 K and decomposed to mixtures containing $La_2Ni_{1-x}M_xO_{4+\delta}$ when the heat-treatment temperature was raised. At this stage all the phase pure

$La_4Ni_{2.7}M_{0.3}O_{10-\delta}$ materials were synthesised again manually using system 1 under the same conditions used previously, to create larger quantities for analysis.

In each case where $La_4Ni_{2.7}M_{0.3}O_{10-\delta}$ was phase pure X-ray powder diffraction patterns were analysed using Le Bail refinement. An anisotropic crystallite size had to be used in each case due to evident anisotropy in the (001) direction. The results of the Le Bail refinement are presented in table 4.1. $La_4Ni_{2.7}M_{0.3}O_{10-\delta}$ (nominal composition) where M = V, Cr, Mn, and Al, which were all hitherto unreported in the literature, are presented in figure 4.3, 4.4, 4.5, and 4.6 respectively.

Table 4.1. Selected lattice parameters in all cases of phase pure $La_4Ni_{2.7}M_{0.3}O_{10-\delta}$. Where the dopant is Ni, indicates the undoped structure. All materials were refined using the Bmab orthorhombic space group. HT = heat-treatment.

HT / K	Dopant / M	*a* / Å	*b* / Å	*c* / Å	*vol* / Å	$P^{\perp}$ / nm	$P^{\parallel}$ / nm	χ^2
1348	Cr	5.4346(5)	5.4928(5)	27.966(5)	834.8(1)	52(2)	24(1)	2.737
	Fe	5.4346(4)	5.4819(4)	28.271(6)	842.3(2)	79(3)	14(1)	8.490
	Co	5.4143(5)	5.4669(4)	27.919(4)	826.4(2)	118(4)	26(1)	1.842
	Ni	5.4132(4)	5.4567(4)	28.109(4)	830.3(1)	143(9)	20(1)	2.539
	Al	5.4182(4)	5.4656(4)	27.999(3)	829.16(8)	89(3)	32(1)	2.620
1448	V	5.4390(4)	5.4860(4)	28.189(6)	841.1(2)	91(4)	18(1)	3.067
	Cr	5.4334(2)	5.4890(2)	28.020(1)	835.7(1)	126(5)	52(3)	1.509
	Mn	5.4271(1)	5.4801(5)	27.993(4)	832.5(2)	110(4)	37(2)	1.642
	Co	5.4146(3)	5.4688(3)	27.976(2)	828.4(1)	164(9)	47(2)	1.899
1548	Cr	5.4348(4)	5.4886(4)	28.057(4)	836.9(1)	115(6)	25(1)	2.075
	Mn	5.4349(2)	5.4875(6)	28.082(3)	837.5(1)	165(8)	31(1)	2.210

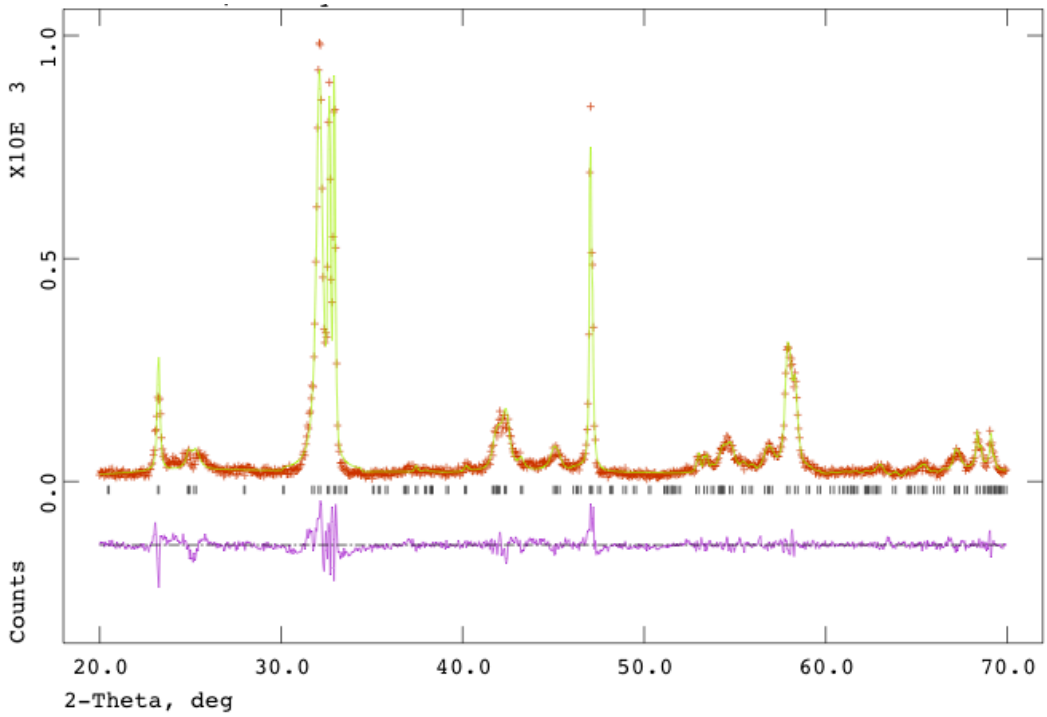

Figure 4.3. Le Bail refinement of $La_4Ni_{2.7}V_{0.3}O_{10-\delta}$. Red crosses indicate experimental data, continuous green line indicates model, and purple line is difference. Tick marks are for the Bmab space group. R_p = 12.78 %, χ^2 = 3.067.

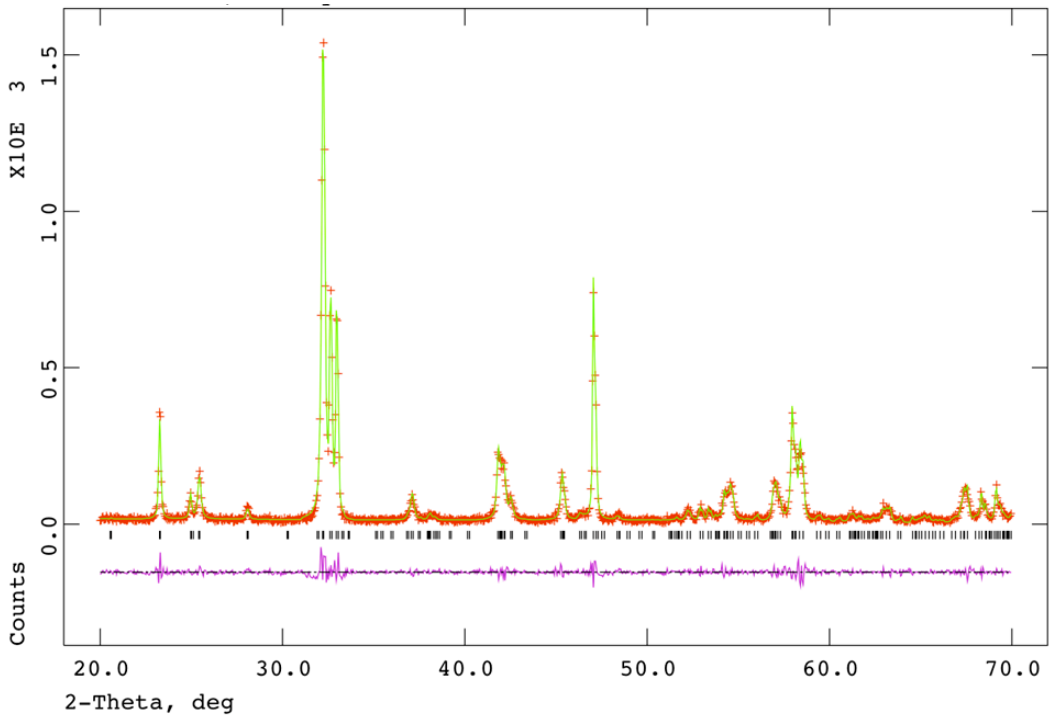

Figure 4.4. Le Bail refinement of $La_4Ni_{2.7}Cr_{0.3}O_{10-\delta}$. Red crosses indicate experimental data, continuous green line indicates model, and purple line is difference. Tick marks are for the Bmab space group. R_p = 9.81 %, χ^2 = 1.509.

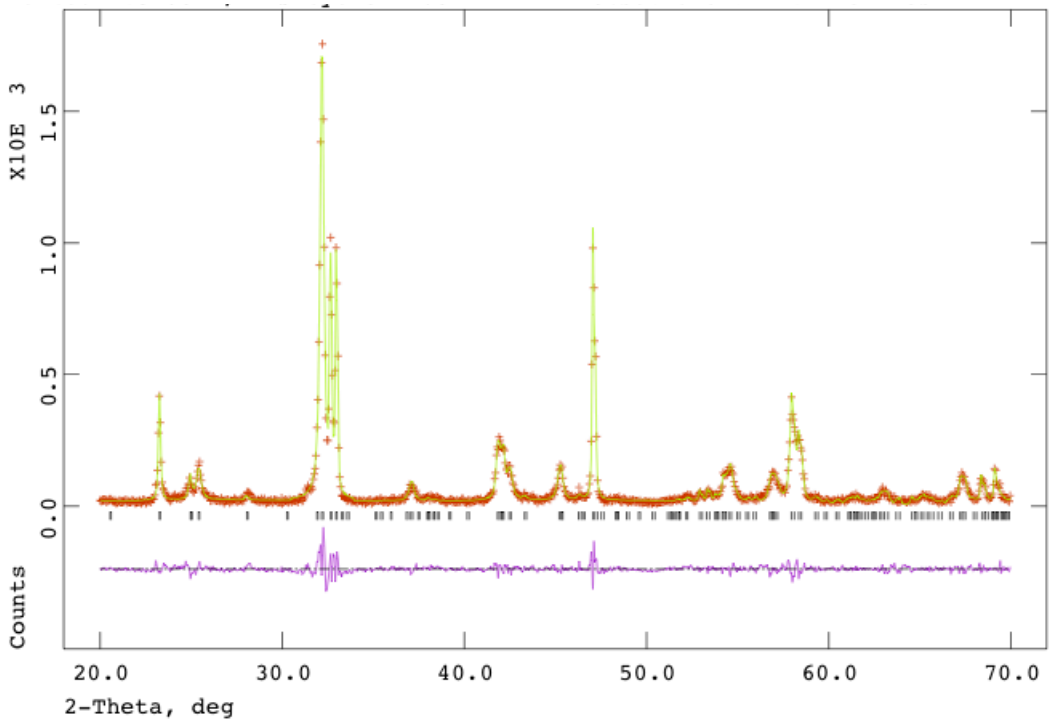

Figure 4.5. Le Bail refinement of $La_4Ni_{2.7}Mn_{0.3}O_{10-\delta}$. Red crosses indicate experimental data, continuous green line indicates model, and purple line is difference. Tick marks are for the Bmab space group. R_p = 11.05 %, χ^2 = 2.210.

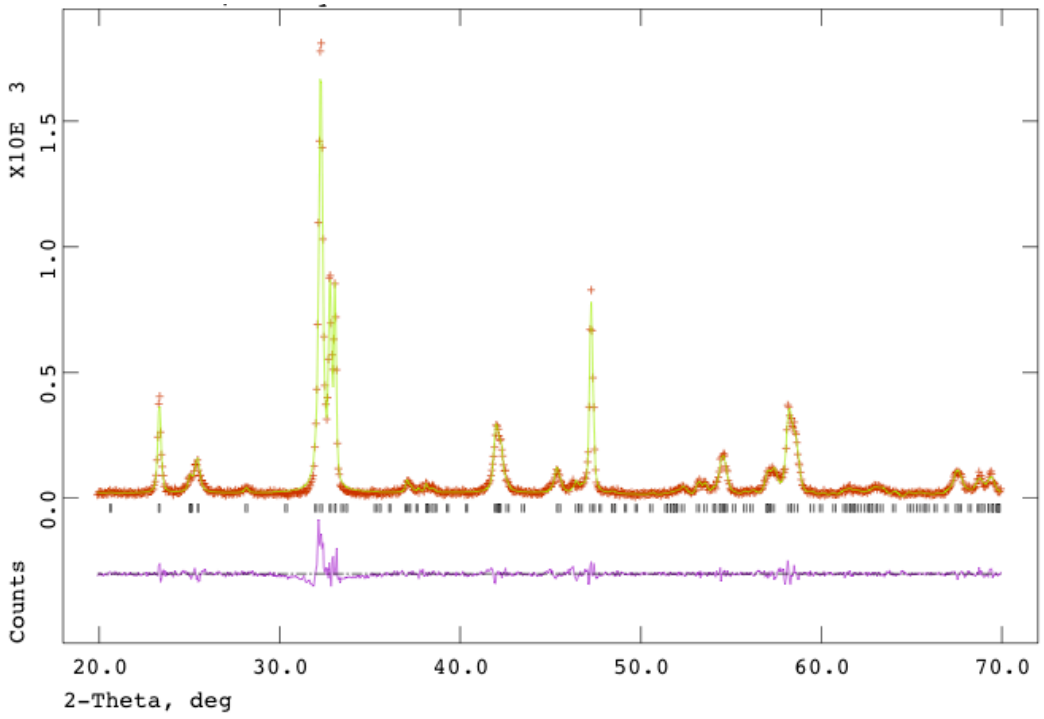

Figure 4.6. Le Bail refinement of $La_4Ni_{2.7}Al_{0.3}O_{10-\delta}$. Red crosses indicate experimental data, continuous green line indicates model, and purple line is difference. Tick marks are for the Bmab space group. R_p = 11.39 %, χ^2 = 2.620.

Unit cell volumes increased approximately linearly with increasing ionic radius, r^{3+}, as predicted by Vegard's law, shown in figure 4.7.

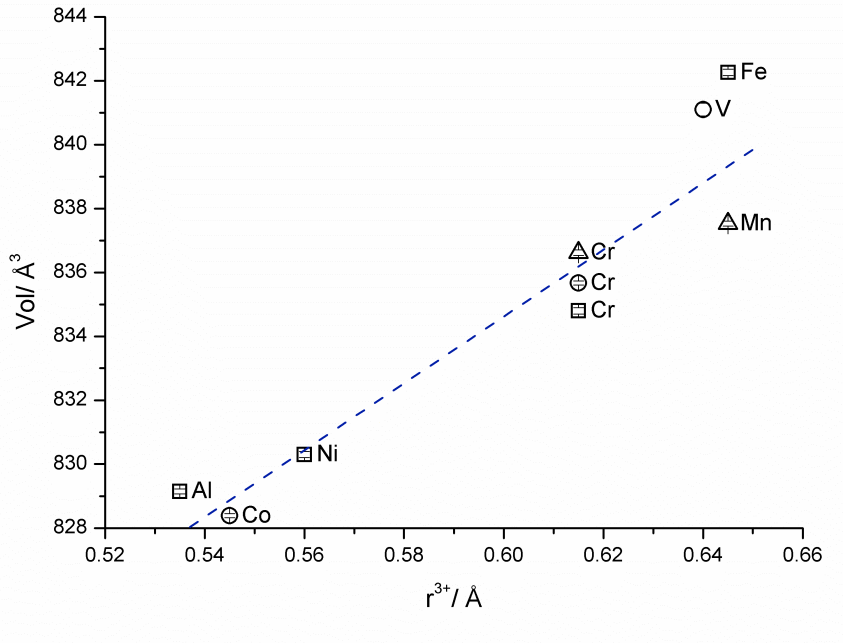

Figure 4.7. Plot of refined volume against ionic radius, r^{3+}. Values of r^{3+} are taken from Shannon ionic radii.(Shannon et al. 1969) Blue line was in keeping with Vegard's law. Squares = heat-treatment 1348 K, 12 hours, Circles = heat-treatment 1448 K, 12 hours. Triangles = heat-treatment 1548 K, 12 hours. Error bars are smaller than the symbols in all cases.

The observed anisotropy was in the (001) direction and therefore suggested a needle-like crystallite. The anisotropy was fitted using an anisotropic crystallite size which gave two values, $P_{\perp}$ and $P_{\parallel}$. The degree of anisotropy was plotted as the difference between the two values, and is shown in figure 4.8. It was assumed that by replacing Ni on the B-site with metals of both increased and decreased ionic radius, the O-M-O bond angles may move away from the ideal 180° and crystallinity may have been altered. As no correlation between the ionic radius of the dopant and the degree of anisotropy in figure 4.8 was observed, this hypothesis proved incorrect.

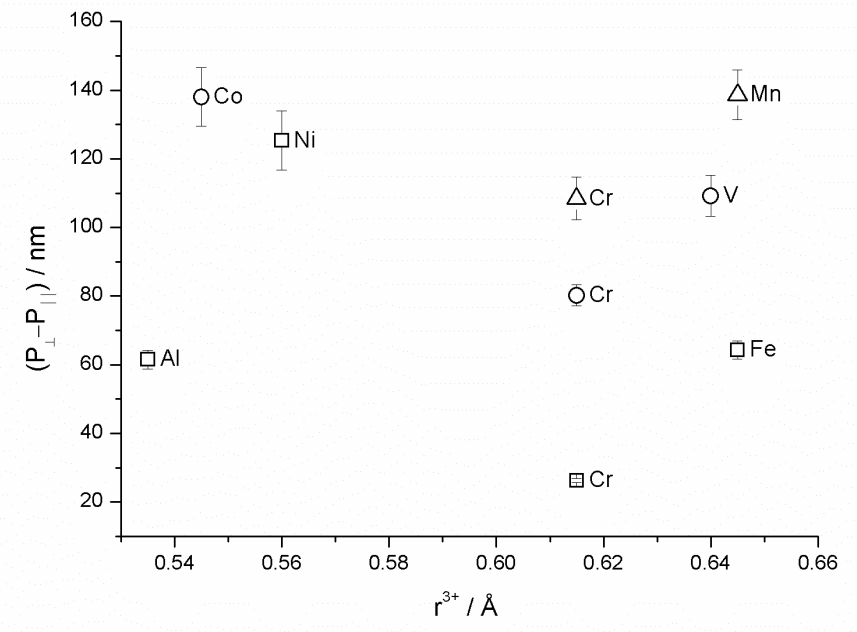

Figure 4.8. Plot of ($P_\perp$ - $P_\parallel$) against ionic radius. r^{3+}. Values of r^{3+} as taken from Shannon ionic radii.(Shannon et al. 1969) Squares = heat-treatment at 1348 K, 12 hours, Circles = heat-treatment at 1448 K, 12 hours. Triangles = heat-treatment at 1548 K, 12 hours.

4.3.3. DC. Conductivity

Phase pure Ruddlesden-Popper, $La_4Ni_{2.7}M_{0.3}O_{10-\delta}$, samples were pressed in a 13 mm KBr die, and the pellets were subsequently sintered at 1573 K for 12 hours in air with a low heating rate of 1 $K.min^{-1}$ to prevent cracking. This method produced sintered discs of 57 – 63 % of maximum theoretical density with no visible cracking on the surface. The maximum density of sintered discs in doped $La_4Ni_{3-x}M_xO_{10-\delta}$ was *ca.* 40 % of maximum theoretical density observed by Amow *et al.*(Amow et al. 2006a) The increased density observed in this study was thought to be as a result of producing smaller $La_4Ni_{3-x}M_xO_{10-\delta}$ crystallites when synthesising from nano-precursors. DC conductivity was then measured as a function of temperature in air using an in-house built 4-point probe. The variation in DC conductivity with temperature for each $La_4Ni_{2.7}M_{0.3}O_{10-\delta}$ sample is plotted in figure 4.9.

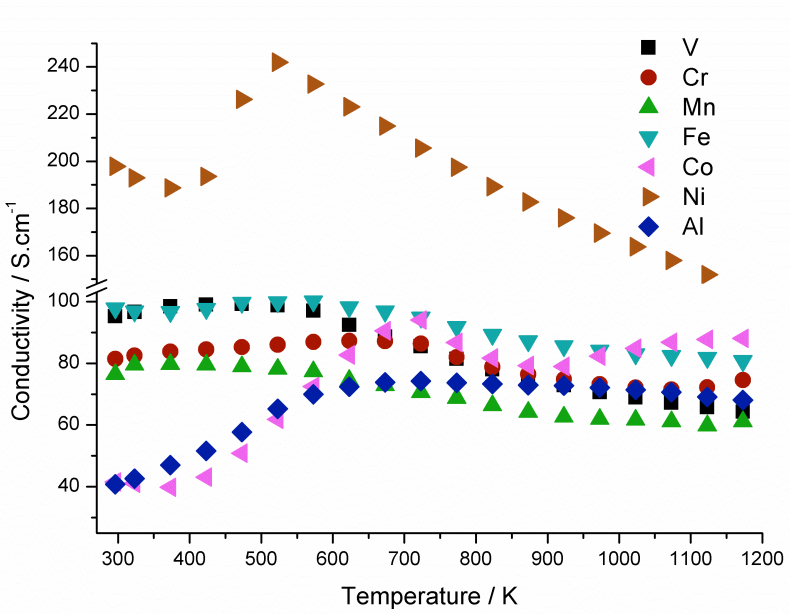

Figure 4.9. DC conductivity against temperature of each $La_4Ni_{2.7}M_{0.3}O_{10-\delta}$ sample, where M = V, Cr, Mn, Fe, Co, Ni and Al. Where the dopant is Ni, this indicates the undoped sample.

The undoped $La_4Ni_3O_{10-\delta}$ (density = 69 %) was the most conductive at 241 $S.cm^{-1}$ at 523 K. All doped samples were less conductive, most likely due to hole doping of the valence band as a result of too high an M(III) content. An anomaly was observed in all samples at ~550 K, this has been observed previously by Amow *et al.* who found that it was be correlated with a non-linearity in the thermal expansion at the same temperature.(Amow et al. 2006b) High-temperature X-ray diffraction of $La_4Ni_3O_{10-\delta}$ shows an increase in symmetry from orthorhombic to tetragonal at approximately 750 K,(Amow et al. 2006b) it was believed therefore that this anomaly was not structural in origin and was related to the loss of oxygen at 550 K. Detailed thermogravimetric analysis of each composition would be required to confirm this hypothesis, also by repeating the experiment and looking for the same response on cooling as well as heating would give some further indication as to the nature of this anomaly. The greatest conductivity of the doped samples was observed in $La_4Ni_{2.7}Fe_{0.3}O_{10-\delta}$ (density = 61 %) with a maximum conductivity of 100 $S.cm^{-1}$ at 573 K, and the least conductive was $La_4Ni_{2.7}Mn_{0.3}O_{10-\delta}$ (density = 65 %) which had a maximum conductivity of 51 $S.cm^{-1}$ at 573 K. Where dopants were: V, Cr, Mn, Co, Al, each were semi-conductors until 523 – 573 K at which point they became

metallic conductors. Both $La_4Ni_{2.7}Fe_{0.3}O_{10-\delta}$ and $La_4Ni_3O_{10-\delta}$ were metallic conductors at room temperature becoming semi conductors between 523 and 573 K. All semi-conducting samples were metallic conductors above 573 K which suggested promotion of valence electrons into the conduction band at increased temperatures. Figure 4.10 shows the comparison of conductivities at IT-SOFC operating temperature (*ca.* 973 K),

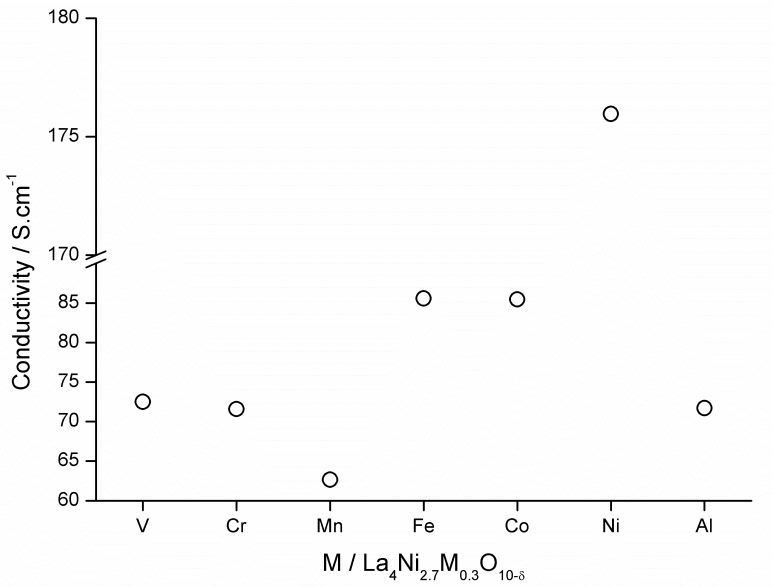

Figure 4.10. Conductivity of phase pure $La_4Ni_{2.7}M_{0.3}O_{10-\delta}$ at 973 K. (Where M = V, Cr, Mn, Fe, Co, Ni and Al). Where M = Ni indicates the undoped sample.

4.3.3.1. Anomaly in Conductivity Measurement

An anomaly was observed in each pellet which manifested itself through a loss of resistance to an equilibrium position on application of a DC bias. After the DC bias was removed the resistance increased to its starting position. This effect was present in each measurement. To test this effect, measurements were taken using the $La_4Ni_{2.7}Co_{0.3}O_{10-\delta}$ pellet in which, at each temperature the resistance was recorded immediately upon application of the voltage. Subsequently the samples were allowed to equilibriate for 10 minutes, and a second measurement was taken after no further drop in resistance was observed. A thermocouple was placed in close proximity to the sample to observe any fluctuations in temperature. The measured increase in conductivity at each temperature is plotted in figure 4.11.

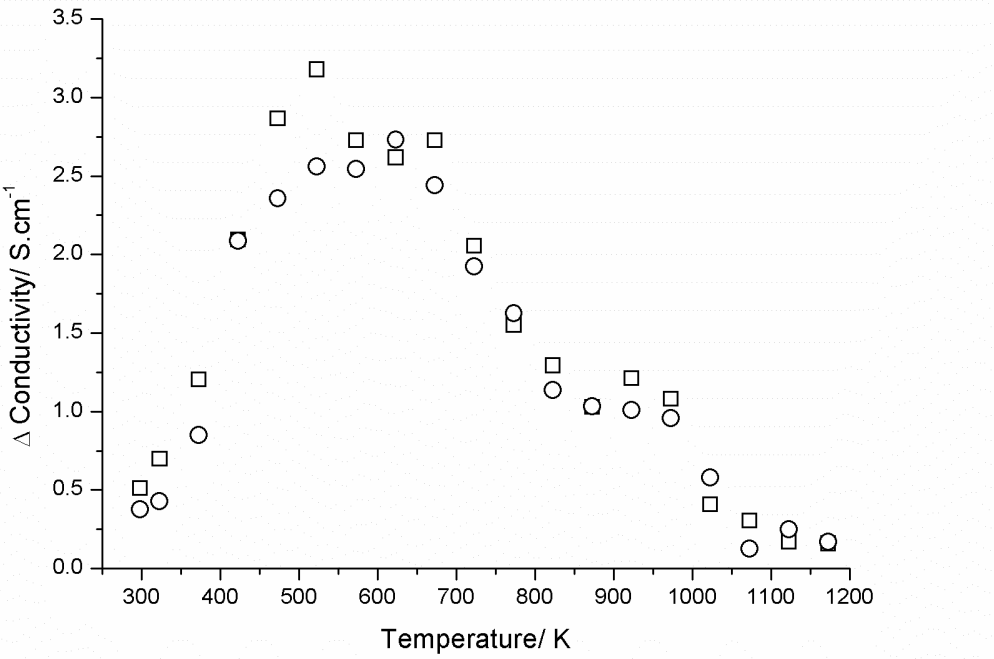

Figure 4.11. Change in conductivity of $La_4Ni_{2.7}Co_{0.3}O_{10-\delta}$ on application of DC bias against temperature. Squares indicate repeat 1, circles repeat 2.

When the change in conductivity was recorded the repeatable difference had a maximum increase in conductivity of 3.1 $S.cm^{-1}$ at 523 K. This effect was observed in all samples. This phenomenon demonstrated a maxima at ~550 K, similar to the effect seen in the change in total conductivity with temperature (shown in figure 4.8). Therefore this anomaly may have also been caused by the loss of oxygen through heating. The reversibility of this measurement was not conducted in this study, however this measurement could provide important insight into the cause of this loss of resistance and whether it is related to a loss of oxygen.

4.4. Conclusions

A manual high-throughput continuous hydrothermal flow synthesis technique has been employed to form nano-precursors for a number of doped lanthanum nickelates. Each set of precursors was divided into three to produce three cloned libraries of samples. Each library was heat-treated at 1348, 1448, or 1548 K, respectively, for 12 hours to bring about solid state transformations, the results of which were investigated using PXRD. By using this approach it was possible to investigate the phase space and optimise reaction conditions quickly supporting hypothesis two (page 61). From a total of twenty-four samples, $La_4Ni_{2.7}M_{0.3}O_{10-\delta}$

(where M = V, Cr, Mn, Fe, Co, Ni, and Al) was identified in twelve cases. In total four compositions previously unknown to the literature were identified.

In the case of phase pure $La_4Ni_{2.7}M_{0.3}O_{10-\delta}$ (where M = V, Cr, Mn, Fe, Co, Ni, and Al) the DC conductivity was tested. It was found that in general 10 at % M(III) on the Ni-site caused hole doping in the valence band resulting in a lowering of conductivity. Both $La_4Ni_{2.7}Co_{0.3}O_{10-\delta}$ and $La_4Ni_{2.7}Fe_{0.3}O_{10-\delta}$ however, demonstrated promising properties that could identify them as potential IT-SOFC cathode materials.

Chapter 5

High–Throughput Synthesis and Discovery of New Iron Doped Lanthanum Nickelates

5.1. Aims

Hypothesis 2 predicted that using a high-throughput approach could make the optimisation of reaction conditions and composition more efficient. Hypothesis 3 suggested that automation of the high-throughput process could increase the number of samples synthesised and therefore get a clearer idea of the phase stability of a target phase. In chapter 4 $La_4Ni_{2.7}Fe_{0.3}O_{10-\delta}$ was identified as a potential IT-SOFC cathode material. This chapter demonstrates a fully automated synthesis strategy with screening for the discovery $La_4Ni_{3-x}Fe_xO_{10-\delta}$ (where $x = 0.0 – 3.0$ and $\Delta x = 0.1$). By using automation the aim was to increase the quantity of samples it was possible to synthesise in a single experiment and therefore identify 'true' phase boundaries as a result.

5.2. Experimental Details

5.2.1. Source Materials

The source materials $[La(NO_3)_3.6H_2O]$ (99.9 %), $[Ni(NO_3)_2.6H_2O]$ (99.9 %) and $[Fe(NO_3)_3.9H_2O]$ (99.9 %) were supplied by Sigma-Aldrich Chemical Company (Dorset, UK). KOH pellets (≥85 %) were supplied by Fisher Scientific Chemical Company (Loughborough, UK). All experiments were conducted using deionised water (10 MΩ) throughout.

5.2.2. Syntheses of Nano-sized Precursor Co-precipitates via RAMSI

A set of co-precipitated, nano-sized precursors were synthesised using the rapid automated synthesis instrument, RAMSI (system 3) with pump rates of 20.0, 10.0 and 10.0 $mL.min^{-1}$ for the scH_2O, metal nitrate and KOH feed, respectively. Each composition was made at 450 °C and 24.1 MPa. Full details and running order of the RAMSI synthesis, clean-up and printing process can be seen in section 2.1.3. Information entered into the RAMSI GUI can be seen in section 2.2.3. Once synthesised, each nano-precursor composition was centrifuged, washed and printed as ceramic dots using the liquid handling functions of RAMSI. Ceramic dots of each

nano-precursor composition were split into two to produce two cloned daughter libraries which were heat-treated at 1348 K and 1573 K, respectively for 12 hours in air. The heat-treated dots were then mounted into a wellplate for high-throughput analysis. Larger quantities of phase pure samples used to form pellets were synthesised manually using system 1 under the same conditions.

5.2.3. Analytical Measurements

Powder X-ray diffraction (PXRD) data were collected using a Bruker-AXS D8 (GADDS) diffractometer (described in section 2.4.3.). Analysis (around phase boundaries) was collected on the Bruker D4 diffractometer using Cu ($K\alpha_1$ and $K\alpha_2$) radiation in reflection geometry. Data were collected over the 2θ range 20 - 70 º with a step size of 0.05 º and a count time of 4 $s.step^{-1}$. Whole profile fitting was conducted using GSAS and the EXPGUI interface.(Larson et al. 1994; Toby 2001) Backgrounds were fitted using a shifted Chebyschev function with six refined parameters. Instrumental peak profile parameters, U, V, and W were calculated using a crystalline CeO_2 standard that had been heat-treated in at 1473 K for 3 days. Anisotropic strain was calculated using profile function 4 in the EXPGUI program, U, V, and W were fixed to instrumental values and S_{004} and η functions refined. Phase-pure samples were prepared as round pellets typically ø = 12.5 mm and thickness = 1 mm which were sintered in air at 1473 K for 12 hours. A ramp rate of 1 $K.min^{-1}$ was used to prevent surface cracking. DC conductivity was calculated using an in-house built 4-point probe (described in section 2.7.). Room temperature Fe K-edge EXAFS data were collected at the B18 beamline at Diamond Light Source, the set-up and data processing strategy are (described in section 2.6.).

5.3. Results and Discussion

5.3.1. Phase identification and X-ray diffraction

5.3.1.1. High-Throughput Screening Stage 1

Iron was selected as a dopant after being identified in chapter 4 as having potential as an IT-SOFC material. $La_4Ni_{3-x}Fe_xO_{10-\delta}$ was doped across the full range of x (0.0 – 3.0) as Amow *et al.* found that when metal dopant content was greater than $x = 2.0$, increased amounts of M(II) were observed resulting in a more conductive compound.(Amow et al. 2006a) Using the HiTCH module of RAMSI, 31 nano-

precursor slurries for the system $La_4Ni_{3-x}Fe_xO_{10-\delta}$ (range $x = 0.0 – 3.0$, $\Delta x = 0.1$) were synthesised at a rate of 7.5 samples per hour. A colour change from green, $x = 0.0$, to brown, $x = 3.0$ was observed, visually indicating an increase in Fe(III) content in each coprecipitated slurry, shown in figure 5.1.

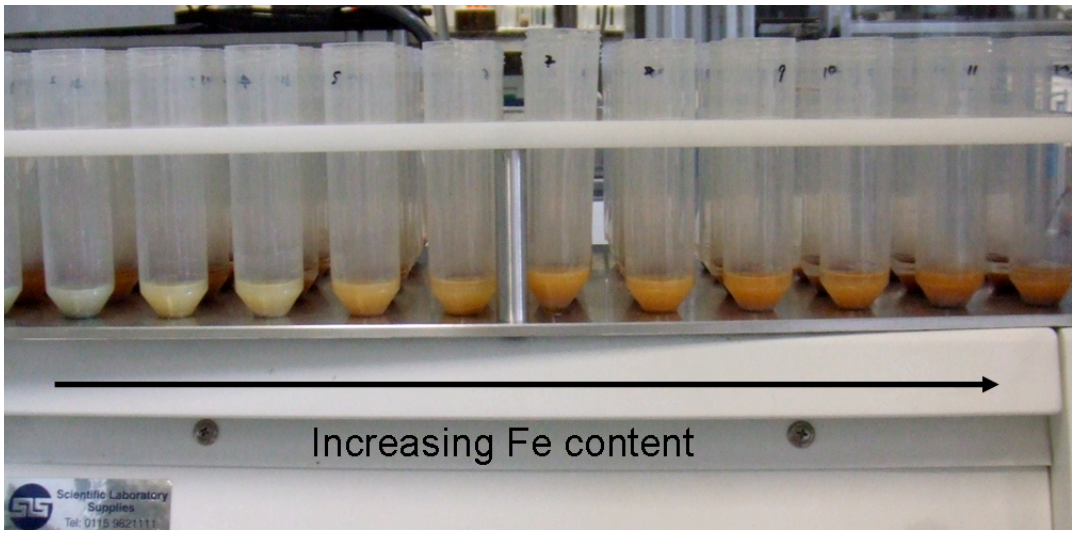

Figure 5.1. Photograph of as-prepared slurries visually indicating increasing Fe(III) content.

Following synthesis, the collected sample tubes were automatically placed into tube racks by RAMSI for 'clean-up' (centrifugation and supernatant replacement in sequence). Centrifugation was performed at 4500 rpm for 1 minute, a throughput of 9 samples per hour was achieved. Following clean-up all supernatant was removed to leave concentrated slurries and all samples were replaced into tube racks. Prior to printing, DI water was added to each sample to adjust the concentration and aid printing. Each combined tube contained approximately 5 mL of slurry to which 600 – 1000 μL of DI water was added to leave a slurry concentration of *ca.* 1.0 ± 0.2 $g.mL^{-1}$. Dots were printed in 100 μL and 125 μL sizes and dried in air. The library was then split into two daughter libraries. The daughter libraries dots were placed manually in a muffle furnace and heat-treated at 1348 K or 1573 K for 12 h on a solid 2 mm thick platinum plate. In order to minimise cracking of the ceramic dots during heat-treatment, all library dots were pre-heated at 353 K for 6 hours, also the ramp rate was kept low, at 2 $K.min^{-1}$. Even when following this method cracking of dots was observed. The samples were then manually fixed flat side up into a custom made 96 well aluminium wellplate. The wellplate was placed onto the *xyz*

diffractometer stage for PXRD screening. The complete combinatorial strategy is shown schematically in figure 5.2.

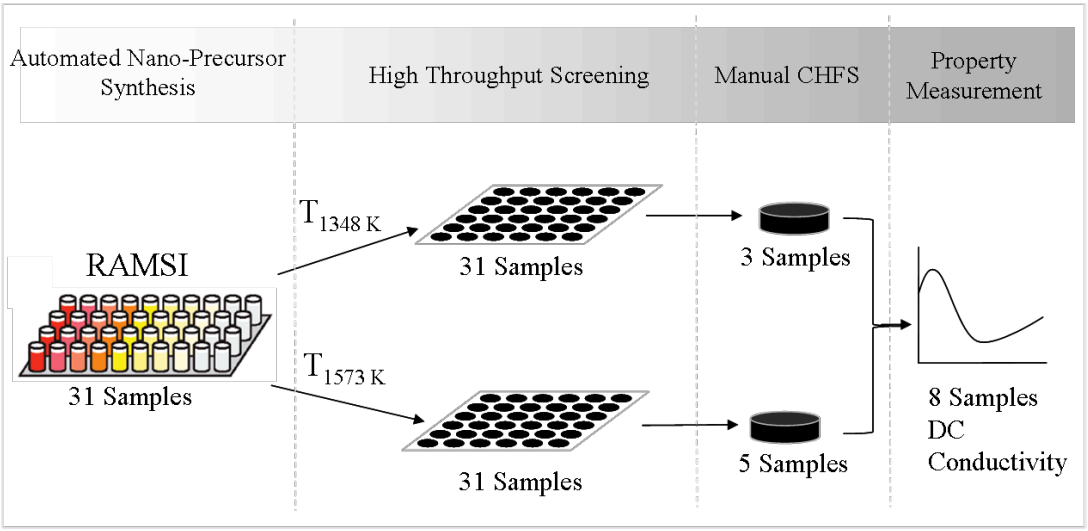

Figure 5.2. A schematic representation of the combinatorial synthesis and screening strategy.

The first screening round of both daughter libraries produced 62 diffraction patterns (31 × 2 temperatures), which highlighted that a possible phase boundary region for $La_4Ni_{3-x}Fe_xO_{10-\delta}$ was *ca.* $x = 0.3 – 0.5$ for samples heat-treated at 1348 K for 12 hours (precise identification was difficult due to the short collection times, and low data resolution). Above this upper limit of solubility for Fe in samples heat-treated at 1348 K, mixtures of $La_4Ni_{3-x}Fe_xO_{10-\delta}$ and $La_2Ni_{1-y}Fe_yO_{4+\delta}$ were observed until $x = 1.5$. In the range $x = 1.5 – 3.0$, mixtures of $LaNi_{1-z}Fe_zO_3$ and La_2O_3 were formed. The daughter library heat-treated at 1573 K for 12 h, suggested the phase boundary for $La_4Ni_{3-x}Fe_xO_{10-\delta}$ could be extended as high as $x = 1.0$. Beyond this limit mixtures of $La_4Ni_{3-x}Fe_xO_{10-\delta}$ and $La_2Ni_{1-y}Fe_yO_{4+\delta}$ were observed as in the case of the 1348 K daughter library. In contrast, previous attempts in the literature to make phase pure $La_4Ni_{3-x}Fe_xO_{10-\delta}$ obtained an upper limit of $x = 0.3$ using polymerisation synthesis based methods taking either 60 or 22 hours at 1353 – 1373 K, with several intermittent regrinding stages.(Carvalho et al. 2009; Tsipis et al. 2007) Samples where $La_4Ni_{3-x}Fe_xO_{10-\delta}$ had not formed were discarded at this point in order to investigate the phase pure Fe-doped compounds and their structure-property relationships.

PXRD data resolution was low for the initial screens due to the difficulties in sample preparation. Surface cracking of dots was seen in most cases, coupled with

short collection times and small quantities of sample, resulted in a less than perfect diffraction conditions. Unit cell refinement was not possible from this data due to large errors in the sample height as a result of imperfect flatness. However the purpose of this initial screen was phase identification only, so it was sufficient for purpose. To obtain more detailed data on structural changes, better quality sample preparation and data collection was then required for selected samples.

5.3.1.2. Manual Screening Stage 2

Once the initial X-ray screening data had been evaluated, eight selected larger samples sizes (*ca.* 0.5 g each) were remade using system 1 described in chapter 2 (using identical reaction conditions to those used during the initial RAMSI synthesis).

PXRD data confirmed that for samples heat-treated at 1348 K, a nominal Fe content as high as $x = 0.3$ ($La_4Ni_{3-x}Fe_xO_{10-\delta}$), in agreement with previously reported results in which a heat and grind method was used from micron-sized oxide precursors at 1370 K.(Kiselev et al. 2007) A La_2O_3 secondary phase was observed in the $x = 0.1$. Compositions where $x = 0.4$ and 0.5 (following heat-treatment either 1348 K and 1573 K) were not very crystalline and appeared to be mixed phases of $La_4Ni_{3-x}Fe_xO_{10-\delta}$ and $La_2Ni_{1-x}Fe_xO_{4+\delta}$. Following heat-treatment at 1573 K for 12 hours in air it was possible to extend the $La_4Ni_{3-x}Fe_xO_{10-\delta}$ phase boundary to a nominal Fe content of $x = 1.0$ (confirmed as $x = 0.94$ using EDX) as shown in figure 5.3.

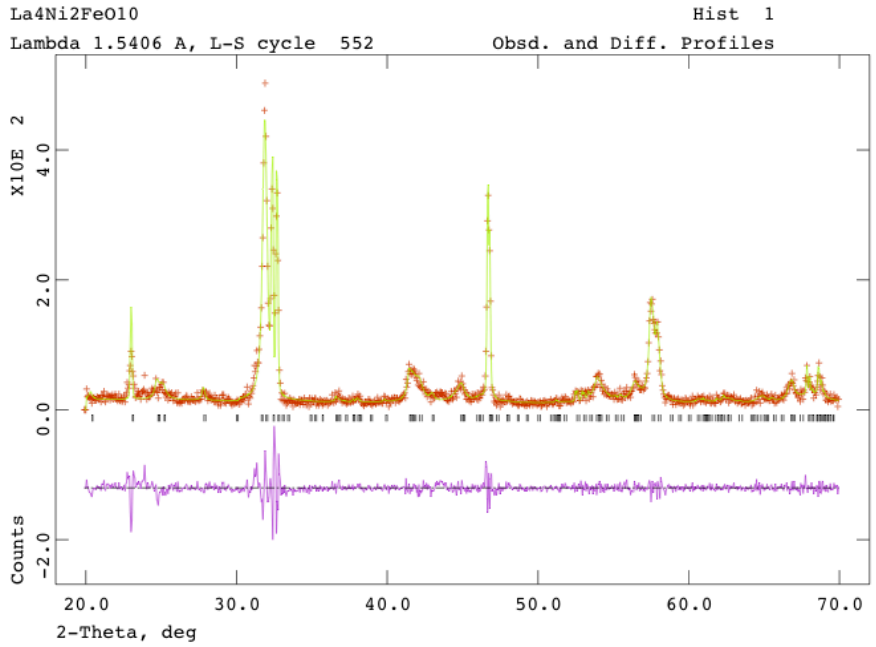

Figure 5.3. $La_4Ni_{2.06}Fe_{0.94}O_{10-\delta}$ synthesised from CHFS precursors at 1548 K for 12 hours. Red crosses indicate experimental data, continuous green line is the model and purple line is the difference. Tick marks are for the Bmab space group. $\chi^2 = 1.826$.

Both Fmmm and Bmab space groups were used in the fitting process, from previous structural studies.(Ling et al. 1999; Zhang et al. 1995) Bmab produced the best fit in all cases and was therefore chosen arbitrarily as the space group. All patterns were highly anisotropic in the (001) direction, figure 5.4 shows the variation in the cell volume with increasing Fe content. The large non-linear variations in the cell volume (particularly in samples heat-treated at 1348 K, 12 hours in air) were as a direct result of the anisotropy in the crystallites.

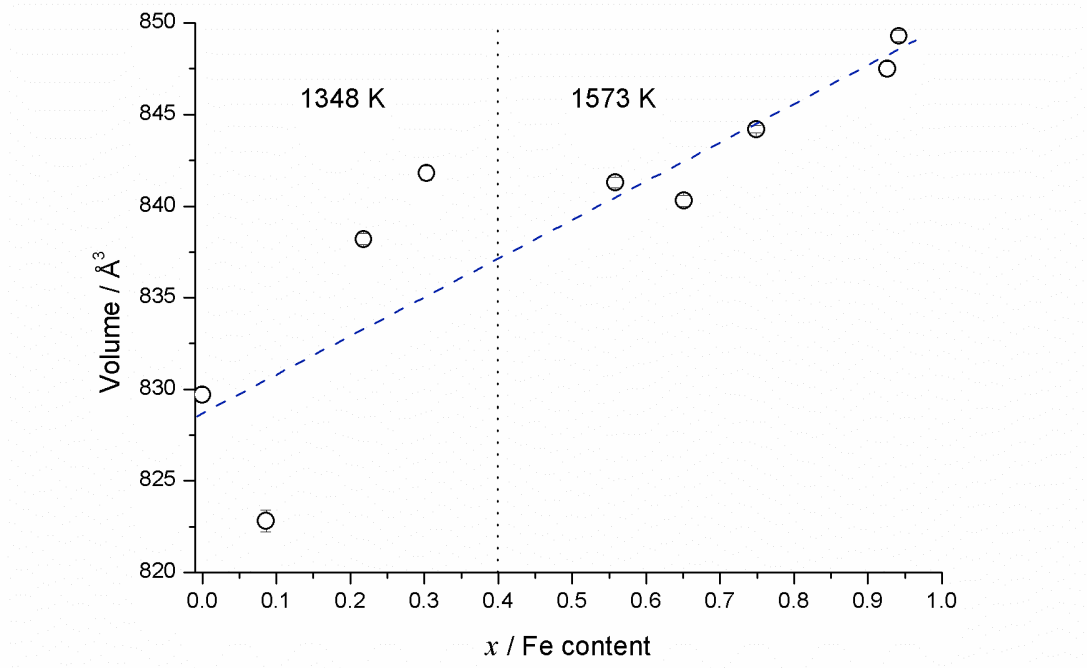

Figure 5.4. Graph of unit cell volume against Fe content for all $La_4Ni_{3-x}Fe_xO_{10-\delta}$ compounds. Error bars are smaller than symbols in all cases. The quoted temperature represents the heat-treatment required to obtain the phases.

During the fitting process it was clear that the $La_4Ni_{2.9}Fe_{0.1}O_{10-\delta}$ sample was considerably less crystalline than the other samples and some La_2O_3 was present in the product. As a result a larger χ^2 value was observed in the Le Bail refinement. This accounted for the anomalously low *c* parameter and volume, 27.73(1) Å and 822.8(6) $Å^3$, respectively. Selected unit cell parameters are described in table 5.1, where Fe content was calculated using EDX spectroscopy. The variation of unit cell parameters *a*, *b*, and *c* is shown in figures 5.5 and 5.6 respectively. A linear increase in all three parameters is observed as expected by Vegard's law, confirming that Fe ions are sitting on lattice sites.

Table 5.1. Selected unit cell values for the $La_4Ni_{3-x}Fe_xO_{10-\delta}$ system. Fe content has been calculated from EDX results.

x / Fe content	a / Å	b / Å	c / Å	Volume / Å^3
0.00	5.4103(8)	5.4567(8)	28.104(7)	829.7(4)
0.09	5.421(1)	5.473(1)	27.73(1)	822.8(6)
0.22	5.4322(7)	5.4757(7)	28.180(6)	838.2(3)
0.30	5.4331(9)	5.4794(8)	28.277(9)	841.8(4)
0.39	—	—	—	—
0.49	—	—	—	—
0.56	5.4439(4)	5.5001(6)	28.097(4)	841.3(3)
0.65	5.4430(8)	5.5016(8)	28.060(7)	840.3(3)
0.75	5.4517(6)	5.5084(6)	28.127(4)	844.7(2)
0.93	5.4591(9)	5.5119(9)	28.167(6)	847.5(4)
0.94	5.4578(7)	5.5117(6)	28.233(8)	849.3(3)

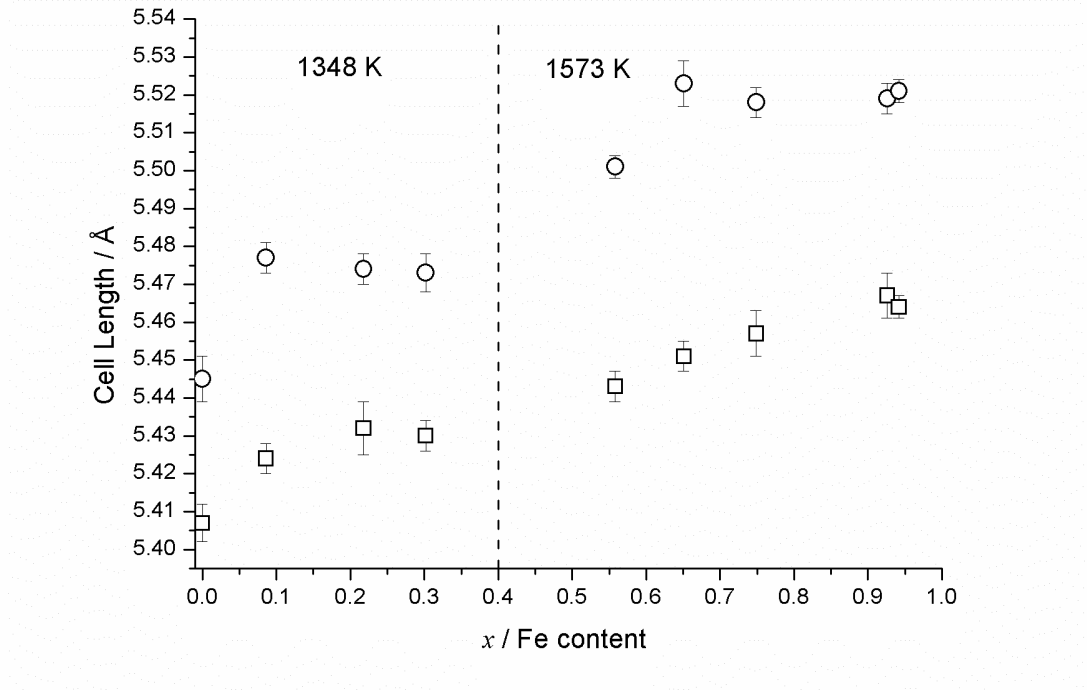

Figure 5.5. Graph showing the increase of unit cell parameters *a* (squares) and *b* (circles) with increasing Fe content. The quoted temperature represents the heat-treatment required to obtain the phases.

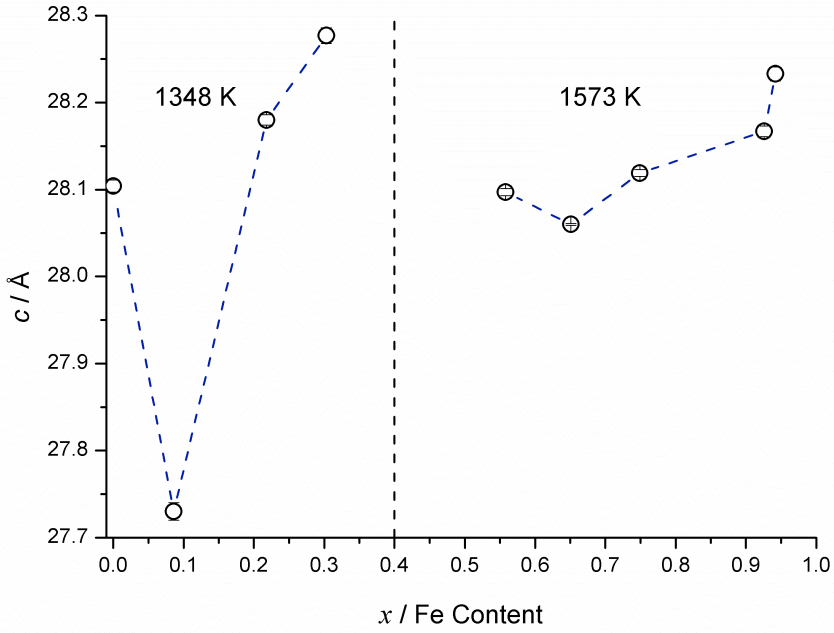

Figure 5.6. Graph of unit cell parameter *c* against Fe content. The line is as a guide for the eye only. Error bars are smaller than symbols in all cases. The quoted temperature represents the heat-treatment required to obtain the phases.

5.3.1.2.1 Anisotropy

As mentioned previously, broadening in the (001) direction was observed in all samples to some extent. The anisotropy in the (001) direction, was greatest in $La_4Ni_{2.7}Fe_{0.3}O_{10-\delta}$, and characterised by broadening in any Bragg reflections where $l \neq 0$ as shown in figure 5.7.

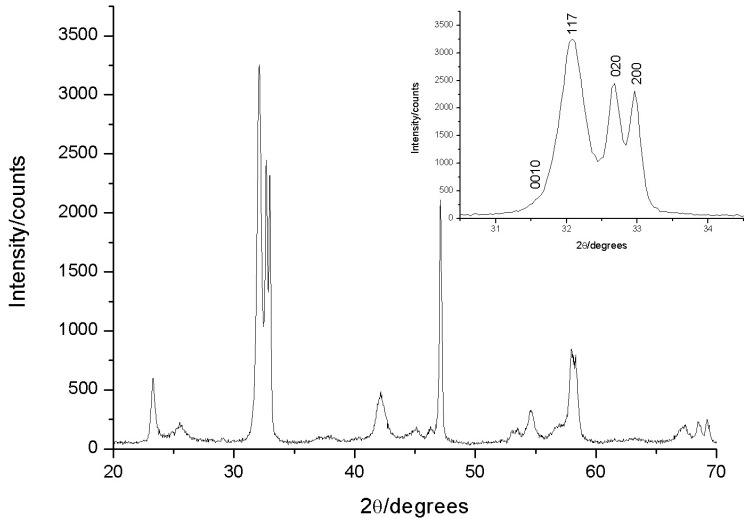

Figure 5.7. X-ray diffraction pattern of $La_4Ni_{2.7}Fe_{0.3}O_{10-\delta}$. **Inset:** Expanded peak highlighting the strong anisotropic broadening in the (001) direction.

The anisotropic broadening was quantified from the Le Bail refinements in GSAS, using an anisotropic strain function. From inspection, it was clear that anisotropy was in the (001) direction only. Therefore U, V, W parameters were set at instrumental levels, and the (001) strain was refined. When peak profiles were refined in this way, better fits were obtained in each case than when using conventional U, V, W, X, and Y profile parameters (as highlighted in figure 5.8 a and b).

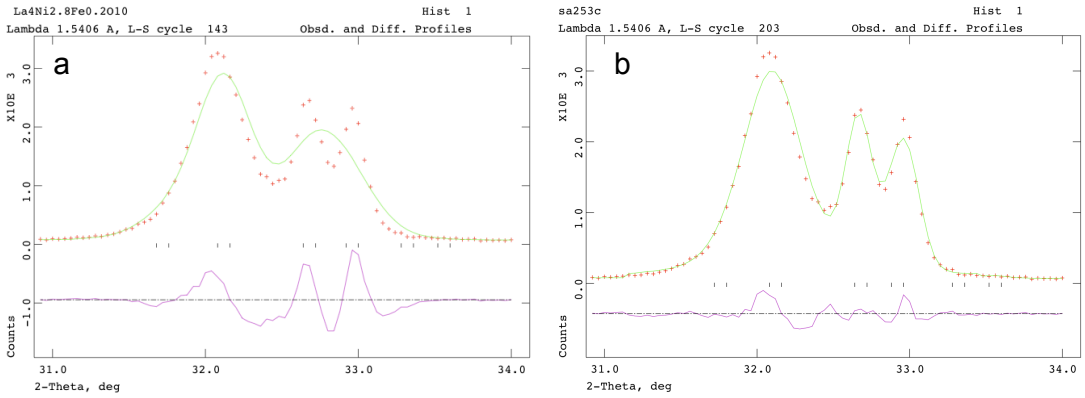

Figure 5.8. Le Bail fits of $La_4Ni_{2.8}Fe_{0.2}O_{10-\delta}$. Peaks are those highlighted (with Miller indices) in figure 5.6 inset above. Red crosses indicate experimental data, green line is model, and purple line is the difference plot. Reflections are marked with ticks. a) Fit using conventional U, V, W, X, and Y profile functions, $\chi^2 = 17.44$. b) Fit using anisotropic strain function, $\chi^2 = 6.266$.

The refined directional strain values are shown in figure 5.9, an approximate linear increase in the (001) broadening was observed in the range $x = 0.0 – 0.3$. At this point a phase boundary was reached and a higher heat-treatment temperature was required to increase Fe content in $La_4Ni_{3-x}Fe_xO_{10-\delta}$. At the higher heat-treatment temperatures the (001) broadening was reduced and remained approximately constant, increasing again only when a further phase boundary was reached ($x = 0.94$). This suggested that a greater heat-treatment temperature had the effect of annealing out the microstructural effect.

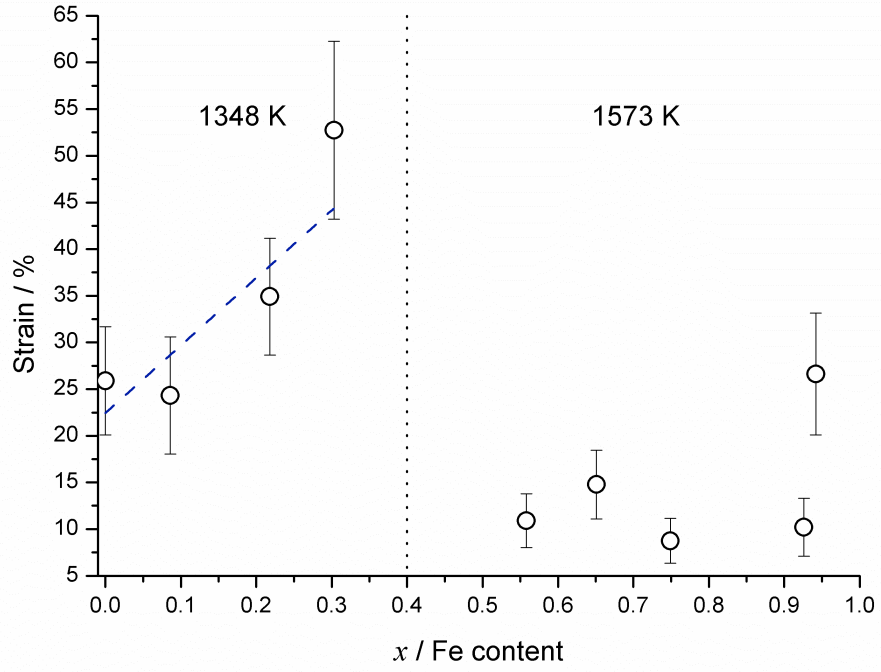

Figure 5.9. Refined percentage strain in the 001 direction for all $La_4Ni_{3-x}Fe_xO_{10-\delta}$ samples.

It is important to note at this stage, that although a strain broadening parameter was used to model the anisotropy, this could also be described using an anisotropic particle size (as in Chapter 4). The strain model was therefore just used to describe the extent of the anisotropic broadening of the diffraction peaks, and not necessarily as a direct result of microstructural strain in the crystallites. The anisotropic broadening could have been related to a loss of crystallinity, particle size effects or local strain within the NiO_6 octahedra, particularly with the introduction of a dopant. Ling *et al.* found, using powder neutron diffraction that the refined anisotropic displacement of the O(1) atoms was much larger than any other atom, with the anisotropy lying along the (001) direction, perpendicular to the Ni(1)-O(1) bond.(Ling et al. 1999)

5.3.2. EXAFS analysis

Selected samples were chosen for Fe K-edge EXAFS analysis. For the analysis, the coordinated of $La_4Ni_3O_{10-\delta}$ reported in the ICSD crystal structure database were used.(Zhang et al. 1995) The starting model was generated in the EXCURVE program and the bond distances of various neighbours and their Debye-Waller factor were refined to obtain the best fit, given in figure 5.10. A multiple-scattering method was employed here to accurately model the structure. The structural parameters obtained from the best fit are given in table 5.2.

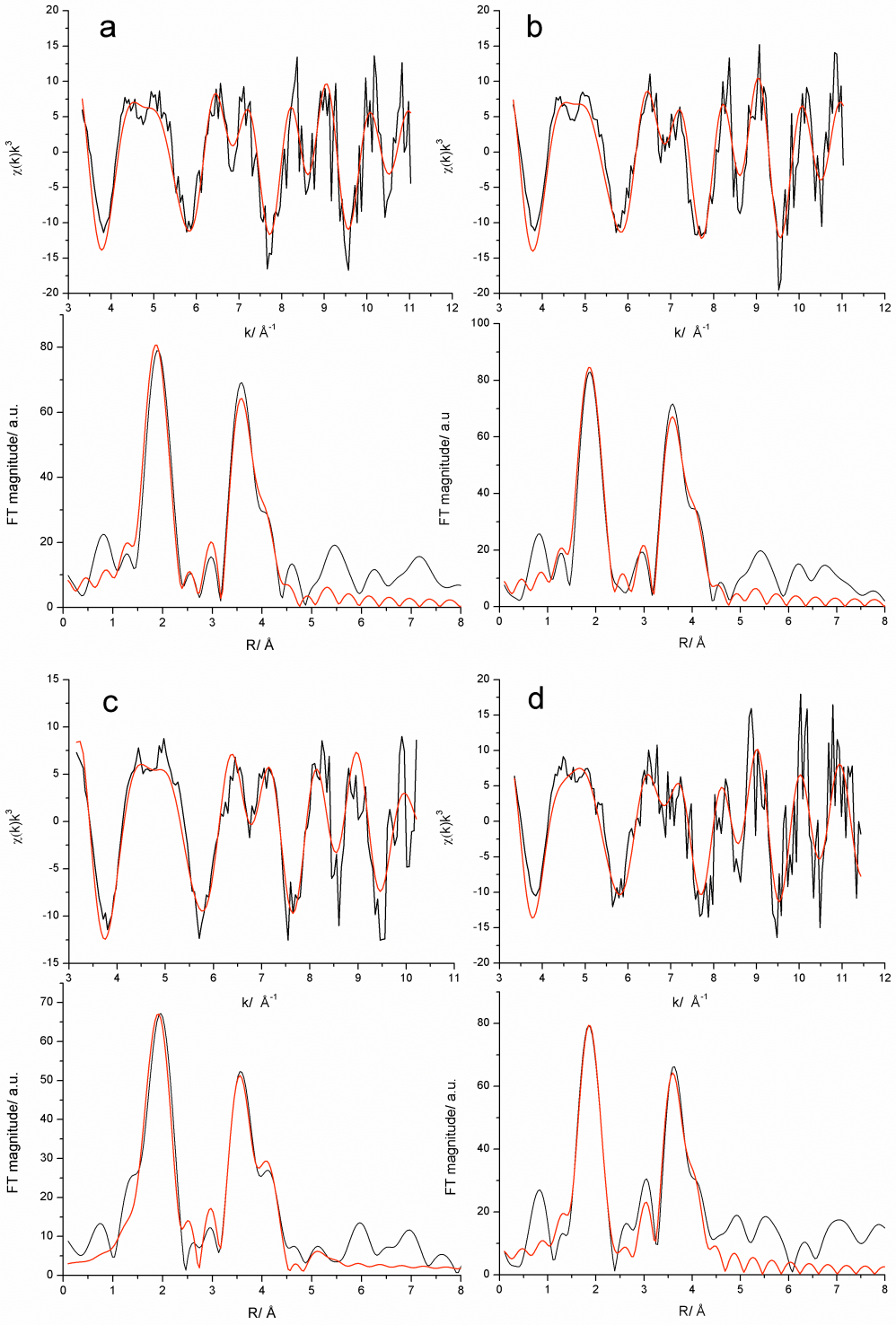

Figure 5.10. EXAFS plots (top) and fitted Fourier transform (bottom) of a) $La_4Ni_{2.8}Fe_{0.2}O_{10-\delta}$, b) $La_4Ni_{2.7}Fe_{0.3}O_{10-\delta}$, c) $La_4Ni_{2.2}Fe_{0.8}O_{10-\delta}$ and d) $La_4Ni_{2.1}Fe_{0.9}O_{10-\delta}$. The black line represents the experimental data, and the red line represents the fitted model. Data collection was performed by Andrew Smith, and data analysis was conducted by Prof. G. Sankar.

Table 5.2. Bond lengths and coordination numbers for selected samples in the series $La_4Ni_{3-x}Fe_xO_{10-\delta}$.

x / Fe content	Fe-O			Fe-La			Fe-Ni			R_{EXAFS}
	N	R	$2\sigma^2$	N	R	$2\sigma^2$	N	R	$2\sigma^2$	
0.2	6	1.944	0.019	8	3.33	0.017	6	3.82	0.028	46.69
0.3	6	1.944	0.011	8	3.34	0.017	6	3.82	0.026	43.38
0.8	6	1.960	0.017	8	3.37	0.009	6	3.86	0.027	39.28
0.9	6	1.940	0.012	8	3.34	0.015	6	3.81	0.028	54.34

EXAFS results given in table 5.2, suggested that Fe(III) cations were located on the B (Ni) sites in all cases. In particular, all the distances obtained from the analysis using the type of near neighbour listed in the table matched that of the parent form $La_4Ni_3O_{10-\delta}$. An estimation of the iron oxidation state was made using the Fe-O bond lengths that were in the range 1.944 – 1.960 Å, which suggested the dopant was Fe^{3+} in all cases. In the undoped $La_4Ni_3O_{10-\delta}$, charge ordering in non-equivalent NiO_6 octahedra was suggested, with preferential occupation of Ni^{3+} on the Ni1 site and Ni^{2+} on the Ni2 site.(Voronin et al. 2001) Bond lengths estimating Fe^{2+} were not observed, suggesting that there was no charge ordering (i.e. no preference for Fe^{3+} on either Ni1 or Ni2 site).

5.3.3. DC conductivity

For seven of the samples ($La_4Ni_{3-x}Fe_xO_{10-\delta}$ $x = 0.0 – 0.3, 0.6 – 1.0, \Delta x = 0.1$) which were shown to be phase pure and which had been scaled up using system 1, dense pressed pellets were formed by pressing powders at 660 MPa in a 13 mm diameter KBr die. The die was gently tapped before pressing, producing a green density in the range 53 – 57 % of theoretical maximum density (by measurement of dimensions). By trial and error it was found that a low heating rate of 1 $K.min^{-1}$ and a sintering temperature of 1473 K for 12 hours, yielded pellets with sintered densities in the range 59 – 69 % of theoretical maximum density, with no visible cracking on the surface of pellets. As in chapter 4 the densities were greater than those achieved in the comparative $La_4Ni_{3-x}Co_xO_{10-\delta}$ system by Amow *et al.*, which were approximately 40 % of theoretical maximum density.(Amow et al. 2006a) The conductivity as a function of temperature was measured for these pellets using the in-house built 4-point DC probe (described in section 2.7).

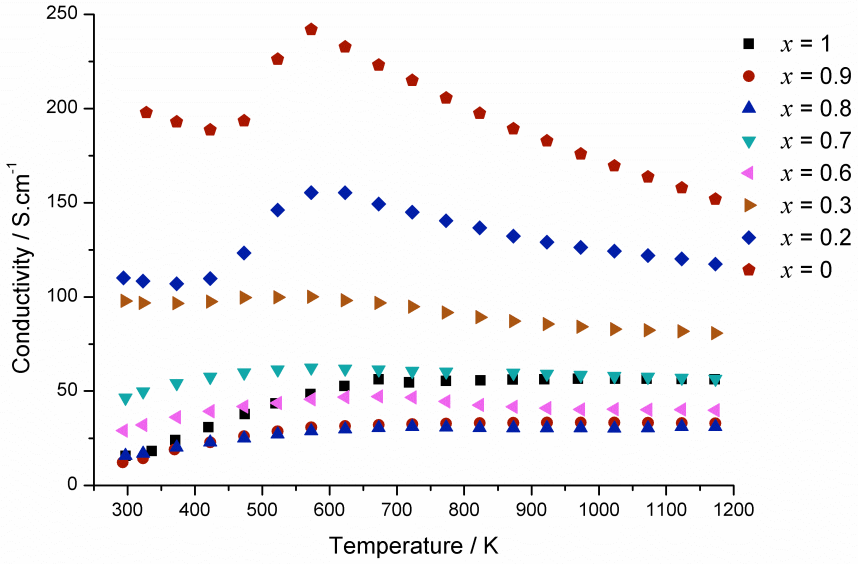

Figure 5.10. Conductivity of phase pure $La_4Ni_{3-x}Fe_xO_{10-\delta}$ as a function of temperature. All samples were 59 – 69 % of theoretical maximum density.

The conductivities of each composition are displayed in figure 5.10, when x = 0.0 – 0.3, the samples were metallic conductors at room temperatures. All others were semi-conductors. A peak in conductivity occurred at *ca.* 573 K, this behaviour had been observed before in the undoped analogues ($La_4Ni_3O_{12}$), and attributed to a structural phase transition from orthorhombic to tetragonal symmetry by Amow *et al.*(Amow et al. 2006b) however this phase transition occurs at 985 K.(Lavrova et al. 1991)

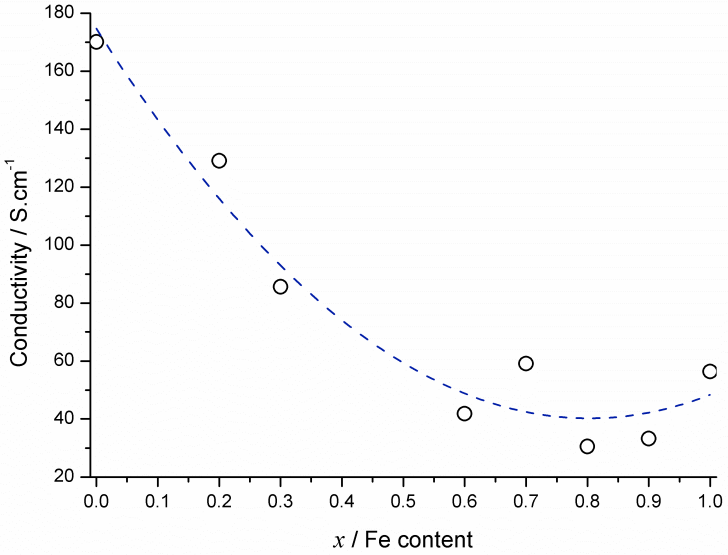

Figure 5.11. Graph showing conductivity of at 923 K against iron content for the $La_4Ni_{3-x}Fe_xO_{10-\delta}$ series.

Figure 5.11 displays how the conductivity at 923 K steadily decreased from 170 $S.cm^{-1}$ (density 62 %) to 31 $S.cm^{-1}$ (density = 58 %) in the *x* range of 0.0 – 0.8, most likely due to hole doping of the valence band as a result of increased M(III) content. These values compared with 50 $S.cm^{-1}$ at 923 K for $La_4Ni_{2.8}Co_{0.2}O_{10-\delta}$ (density = 40 %),(Amow et al. 2006a) and 95 $S.cm^{-1}$ at 950 K for undoped $La_4Ni_3O_{10-\delta}$ (density = 58 %).

Interestingly, it was observed that at lower temperatures (< 773 K) upon application of a voltage to points 1 and 2 (of the 4-point DC conductivity testing apparatus where the numbering manner is clockwise and incremental from 1-4), the observed resistance through points 3 and 4 fell rapidly over 10 – 30 s, until an equilibrium value was reached. When the voltage was then removed across pins 1 and 2, the resistance measured through points 3 and 4 slowly returned to the original value. This was an identical effect to that described in section 4.3.3.1., where it was described in more detail.

5.4. Conclusions

In conclusion, a fully automated nano-precursor coprecipitation and heat-treatment route to direct combinatorial solid state synthesis has been described. Several "difficult to make" and hitherto unknown phase-pure heterometallic Ruddlesden Popper type ($La_4Ni_{3-x}Fe_xO_{10-\delta}$) materials have been identified. The new approach used robotic automation (RAMSI) which incorporated a high-throughput reactor to rapidly synthesise a range of nanoparticle co-precipitate precursors in cloned libraries at a rate of 7.5 samples an hour. Each library could then be heat-treated at a different temperature and an initial powder XRD screen was used to locate the approximate phase boundary. A more focussed second scaled-up synthesis and PXRD characterisation of selected larger heat-treated powders was then performed to reconfirm the locations of the phase boundaries with the highest dopant level being achieved for $La_{4.13}Ni_{2.06}Fe_{0.94}O_{10-\delta}$ which is significantly greater Fe doping than has been achieved by anyone previously (despite several efforts in this field). EXAFS data suggested that Fe^{3+} was located onto Ni sites in all cases and did not exist as a separate iron oxide phase.

The DC conductivity of all the single phase materials obtained was then investigated; electronic conduction generally decreased with increasing Fe content.

In summary this fully automated combinatorial synthesis route for direct solid state chemistry coupled with rapid screening, has allowed faster access to samples that were previously unknown and inaccessible via more conventional “heat and grind” or similar approaches. It has also allowed rapid identification of the 'true' phase boundary and the conditions with which to obtain in going someway to answering hypothesis 2 and 3.

Chapter 6

Automated High-Throughput Synthesis and Screening of $La_4Ni_{3-x}M_xO_{10-\delta}$ and $La_3Ni_{2-x}O_{7-\delta}$ (where M = Mn, Pd, Al, Ga, x = 0.0 – 2.0 and Δx = 0.2)

6.1 Aims

Chapter 5 described a fully automated approach to CHFS, producing a library of 62 samples which were heat-treated in parallel to bring about solid-state transformations. The resulting phases were then screened for suitable properties using X-ray diffraction and DC electrical testing. In the previous chapter X-ray diffraction quality was low and a further screening stage was required to confirm phase boundary regions. Hypothesis 3 (page 60) stated that if the automated synthesis using RAMSI were to be combined with an automated screening method such as X-ray diffraction, it should be possible to investigate hundreds of compositionally unique heterometallic oxides in one experiment. By doing this it would be possible to optimise synthesis conditions and get a clearer idea of 'true' phase boundaries. In order to test this hypothesis 80 compositionally unique precursors was synthesised for the $La_4Ni_{3-x}M_xO_{10-\delta}$ and $La_3Ni_{2-x}M_xO_{7-\delta}$ systems (where M = Mn, Pd, Al and Ga, x = 0.0 – 2.0 and Δx = 0.2). As in previous chapters, each composition was split into three and heat-treated at either 1348, 1448 or 1548 K, to generate 3 daughter libraries (240 unique samples in total) which were then investigated structurally using automated powder X-ray diffraction in a single library.

6.2 Experimental Details

6.2.1. Source Materials

The source materials $[La(NO_3)_3.6H_2O]$ (99.9 %), $[Ni(NO_3)_2.6H_2O]$ (99.9 %), $[Mn(NO_3)_2.6H_2O]$ (99.9 %), $[Pd(NO_3)_2.6H_2O]$ (99.9 %), $[Al(NO_3)_3.9H_2O]$ (99.9 %) and $[Ga(NO_3)_3.9H_2O]$ (99.9 %) were supplied by Sigma-Aldrich Chemical Company (Dorset, UK). KOH pellets (≥85 %) were supplied by Fisher Scientific Chemical

Company (Loughborough, UK). All experiments were conducted using deionised water (10 MΩ) throughout.

6.2.2. Syntheses of Nano-Precursor Co-precipitates using RAMSI

A set of 80 co-precipitated, nano-precursors were synthesised using the HiTCH flow synthesis module within RAMSI. Full details and running order of the RAMSI synthesis and clean-up process can be seen in section 2.2.4. Following automated clean-up using RAMSI, each composition was freeze dried for 18 hours and subsequently split into three equal parts to create three daughter libraries, each composition was then heat-treated at either 1348, 1448 or 1548 K for 12 hours in air to give a total of 240 samples.

6.2.3. Analytical Measurements

High-throughput screening data were collected using a position sensitive detector, PSD. The PSD had a 90° aperture that allowed collection of a powder pattern in milliseconds. Data collection time was 2 seconds per pattern, a further 30 seconds were required to change samples using the robot arm and carousel, therefore all 240 diffraction patterns were collected in 2.1 hours. Full details are presented in section 2.4.4.2.

Data for further refinement of selected structures of interest (that were phase pure) were collected at room temperature using the MAC detectors. Collection time was 30 minutes of the 2θ range 0 – 160 °2θ. Wavelength (λ = 0.825582(2) Å) and zero point (0.006679(2) °) were calculated using a silicon standard, (NIST SRM640c). Whole profile fitting was conducted using GSAS and the EXPGUI interface.(Larson et al. 1994; Toby 2001) Instrumental peak profile parameters, U, V, and W were calculated using a Si standard (NIST srm640c). Anisotropic strain was calculated using profile function 4 in the EXPGUI program, with U, V, and W fixed to instrumental values.

6.3 Results and Discussion

Dopants Mn and Pd were selected to increase hybridisation of the M 3*d* and O 2*p* orbitals of the $La_4Ni_{3-x}M_xO_{10-\delta}$ and $La_3Ni_{2-x}M_xO_{7-\delta}$ structure and by doing so potentially increase DC conductivity.(Sreedhar et al. 1994) Al and Ga were selected

to explore the possibility of using main group metals as dopants in the CHFS system. Eighty compositionally unique nano-precursors for the attempted synthesis of doped materials $La_4Ni_{3-x}M_xO_{10-\delta}$ and $La_3Ni_{2-x}M_xO_{7-\delta}$ (where M = Pd, Mn, Al, and Ga) were synthesised using the RAMSI robot. Synthesis throughput was calculated at 9 samples per hour. Each composition was split into three and heat-treated at 1348, 1448, or 1548 K to produce a total of 240 samples. Screening was conducted using powder X-ray diffraction at Diamond Light Source, I11. Powders were loaded into capillaries and placed onto a carousel, whereupon they were collected in turn by robot arm for analysis. Data were collected using a PSD detector (described in chapter 2) for 2 seconds per pattern. Including time taken to change samples total time was 30 seconds per pattern; throughput at this stage was 120 samples per hour. The workflow diagram of the process is shown in figure 6.1.

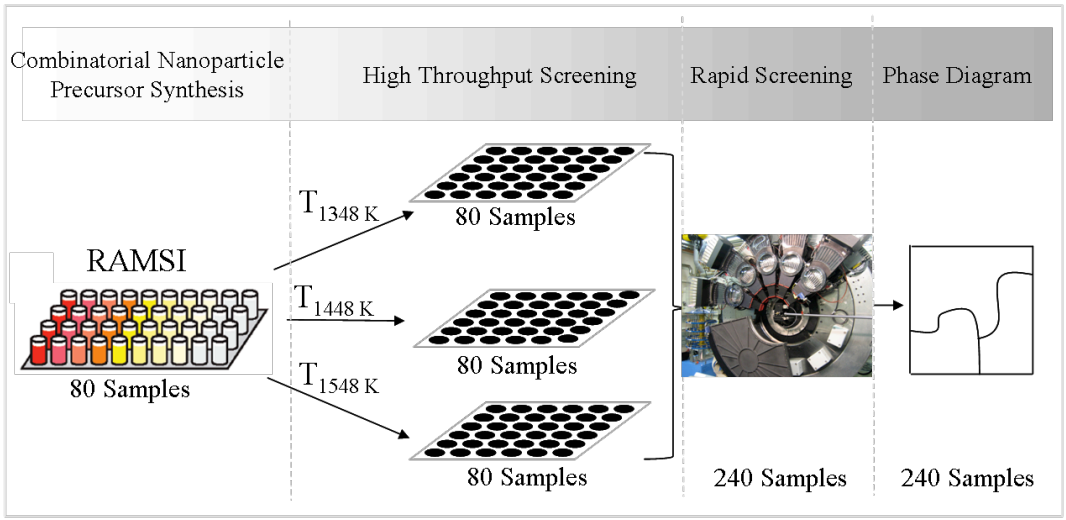

Figure 6.1. Work-flow diagram representing the stages involved in the fully automated combinatorial process.

6.3.1. High-Throughput Screening using PSD

6.3.1.1. Pd structures

For the nano-precursor ratio La_4:$Ni_{3-x}Pd_x$ in the range x = 0.2 – 2.0 and Δx = 0.2, the products formed in each case are presented in figure 6.2. Each point in figure 6.2 on the phase plot represents an individual composition, some of which were mixture and some of which were phase pure compounds (identified using powder XRD).

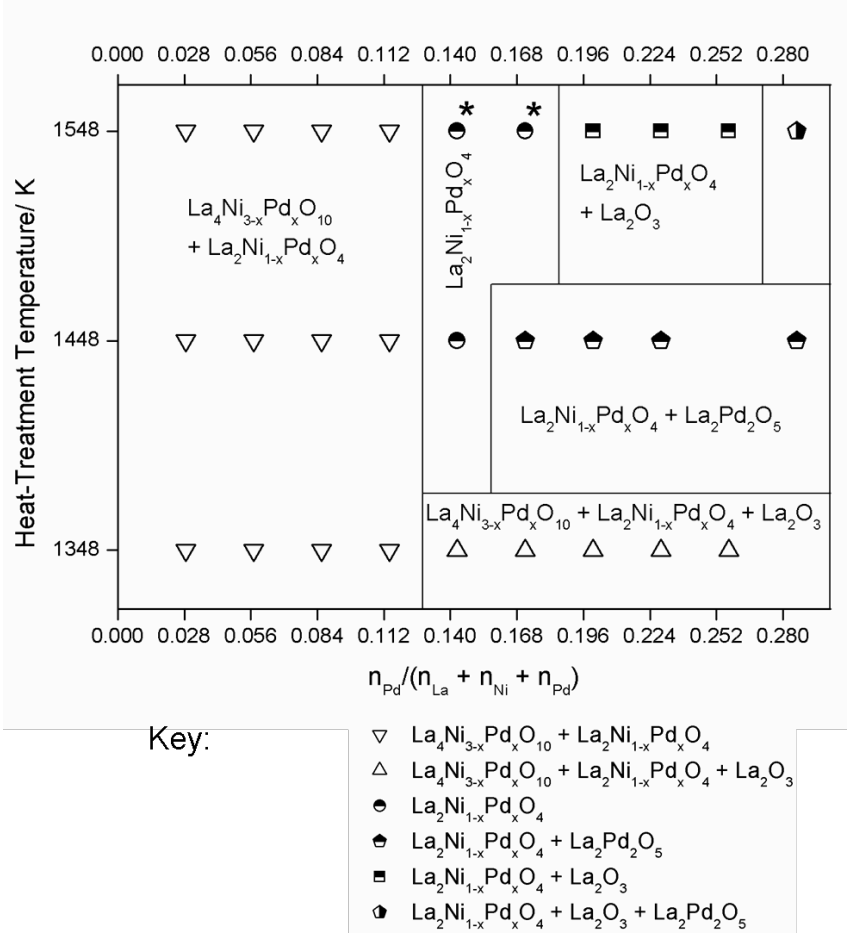

Figure 6.2. Phase diagram at room temperature pressure for the phases formed from CHFS precursors for the compositions $La_4:Ni_{3-x}Pd_x$ (where $x = 0.2 – 0.0$ and $\Delta x = 0.2$) after heat-treatment for 12 hours in air. At% of dopant = $n_{Pd}/(n_{La}+n_{Ni}+n_{Pd})$. Each point represents a unique composition, some of which are mixtures and some of which are phase pure compounds. In each case the phase identified from powder XRD is given in the key. Samples marked with an asterisk were selected for further investigation.

$La_4Ni_{3-x}Pd_xO_{10-\delta}$ could not be isolated at any dopant level of Pd. The thermodynamically more stable $La_2Ni_{1-x}Pd_xO_{4+\delta}$ was formed as a secondary product in each case. This was possible due to the difference in ionic radius between Ni^{2+} and Pd^{2+} (0.69 and 0.86 Å), and Ni^{3+} and Pd^{3+} (0.6 and 0.76 Å).(Shannon et al. 1969) The larger ionic radius of Pd meant that only small quantities ($< x = 0.2$, *ca.* 6 at%) could be incorporated into either structure without the formation of a secondary phase. At high values of Pd (> 15 at% $x = 1.2$) $La_2Pd_2O_5$ was formed at both 1448 and 1548 K (as part of a phase mixture) which further suggested that the ionic radius of Pd was

too large to be incorporated in to the Ruddlesden-Popper structure. What appeared to be phase-pure $La_2Ni_{1-x}Pd_xO_{4+\delta}$ was synthesised at 1448 and 1548 K at nominal Pd concentrations of 14 at% and 17 at% at 1548 K only (representing nominal formulas $La_2Ni_{0.66}Pd_{0.33}O_{4+\delta}$ and $La_2Ni_{0.6}Pd_{0.4}O_{4+\delta}$). These phases were selected for further investigation in detail using high-resolution powder X-ray diffraction later in section 6.3.2.1.

For the nano-precursor ratio $La_3:Ni_{2-x}Pd_x$ in the range x = 0.2 – 2.0 and Δx = 0.2, products formed from each heat-treatment are presented in figure 6.3.

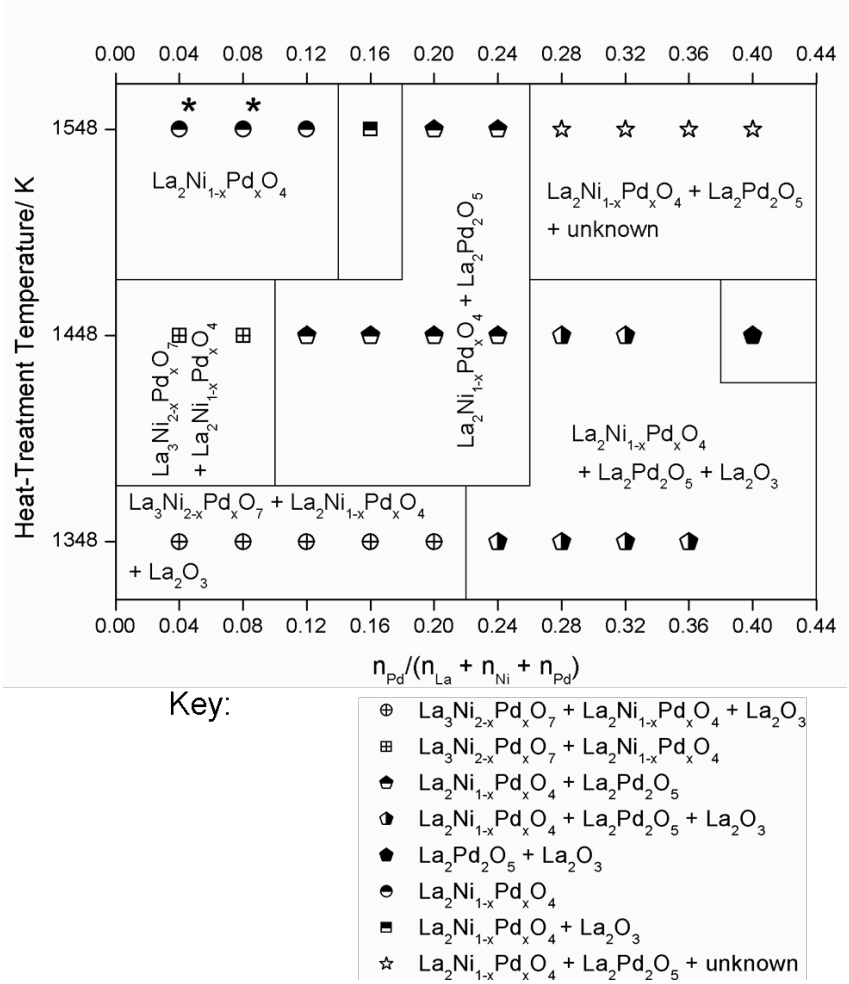

Figure 6.3. Phase diagram at room temperature pressure for the phases formed from CHFS precursors for the compositions $La_3:Ni_{2-x}Pd_x$ (where x = 0.2 – 0.0 and Δx = 0.2) after heat-treatment for 12 hours in air. At% of Pd = $n_{Pd}/(n_{La}+n_{Ni}+n_{Pd})$. Each point represents a unique composition, some of which are mixtures and some of which are phase pure compounds. In each case the phase identified from powder XRD is given in the key. Samples marked with an asterisk were selected for further investigation.

When the nano-precursors were in the ratio La_3:$Ni_{2-x}Pd_x$, (x = 0.0 – 2.0 and Δx = 0.2) phase-pure $La_3Ni_{2-x}Pd_xO_{7-\delta}$ was not isolated. In each case where small amounts of the $La_3Ni_{2-x}Pd_xO_{7-\delta}$ were observed, $La_2Ni_{1-x}Pd_xO_{4+\delta}$ was seen as a secondary minor phase product. As in the 4:3 case $La_2Pd_2O_5$ was formed at high values of dopant. This was most likely caused by the difference in ionic radius between $Ni^{2/3+}$ and $Pd^{2/3+}$ as described above. Phase pure material with the $La_2Ni_{1-x}Pd_xO_{4+\delta}$ structure (nominal formulas ($La_2Ni_{0.9}Pd_{0.1}O_{4+\delta}$ and $La_2Ni_{0.8}Pd_{0.2}O_{4+\delta}$) could be identified at 1548 K and these structures were selected for further analysis in section 6.3.2.1. Data collected using the MAC detector again revealed small quantities of NiO which appeared to be inhomogeneous suggesting that some Pd had been incorporated into the NiO structure so the nominal value of x was not representative of the 'true' Pd content.

6.3.1.2. Mn Structures

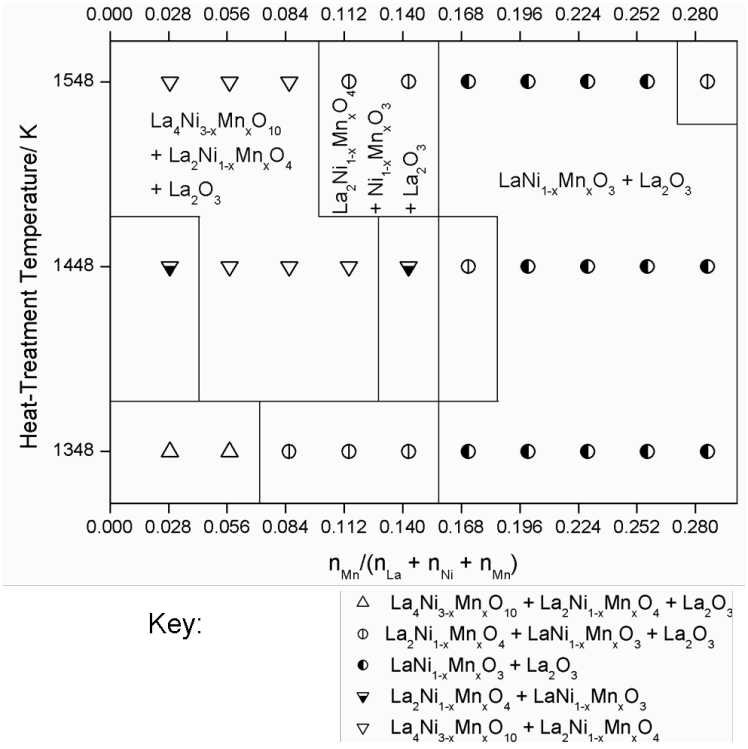

Figure 6.4. Phase diagram at room temperature pressure for the phases formed from CHFS precursors for the compositions La_4:$Ni_{3-x}Mn_x$ (where x = 0.2 – 0.0 and Δx = 0.2) after heat-treatment for 12 hours. At% of Mn = $n_{Mn}/(n_{La}+n_{Ni}+n_{Mn})$. Each point represents a unique composition, some of which are mixtures and some of which are phase pure compounds. In each case the phase identified from powder XRD is given in the key.

Where the dopant was Mn and precursors were in the ratio $La_4:Ni_{3-x}Mn_x$ (x = 0.0 – 2.0 and Δx = 0.2) no single phase material could be synthesised. Only when x < 0.8 could any lanthanum nickelate phases be isolated without a La_2O_3 decomposition phase due to $LaNi_{1-x}Mn_xO_3$ forming favourable and leaving a lanthanum excess. This could have been as a result of a combination of Mn^{3+} having a coordination number of both 5 and 6 and a larger ionic radius of 0.6, meaning that only the more flexible perovskite structure could form.

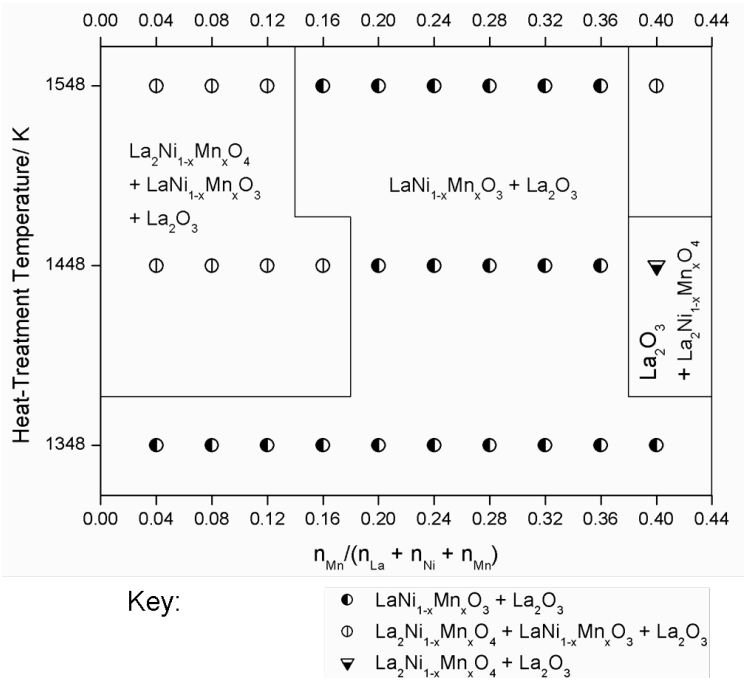

Figure 6.5. Phase diagram at room temperature pressure for the phases formed from CHFS precursors for the compositions $La_3:Mn_{2-x}Pd_x$ (where x = 0.2 – 0.0 and Δx = 0.2) after heat-treatment for 12 hours in air. At% of Mn = $n_{Mn}/(n_{La}+n_{Ni}+n_{Mn})$. Each point represents a unique composition, some of which are mixtures and some of which are phase pure compounds. In each case the phase identified from powder XRD is given in the key.

When the nano-precursor ratio was $La_3:Ni_{2-x}Mn_x$ (where x = 0.2 – 0.0 and Δx = 0.2) no phase pure materials could be obtained, La_2O_3 was obtained in all cases, the lanthanum nickelates that were observed were in the $La_2NiO_{4+\delta}$ and $LaNiO_3$ forms and these materials were not therefore selected for further analysis.

6.3.1.3. Al Structures

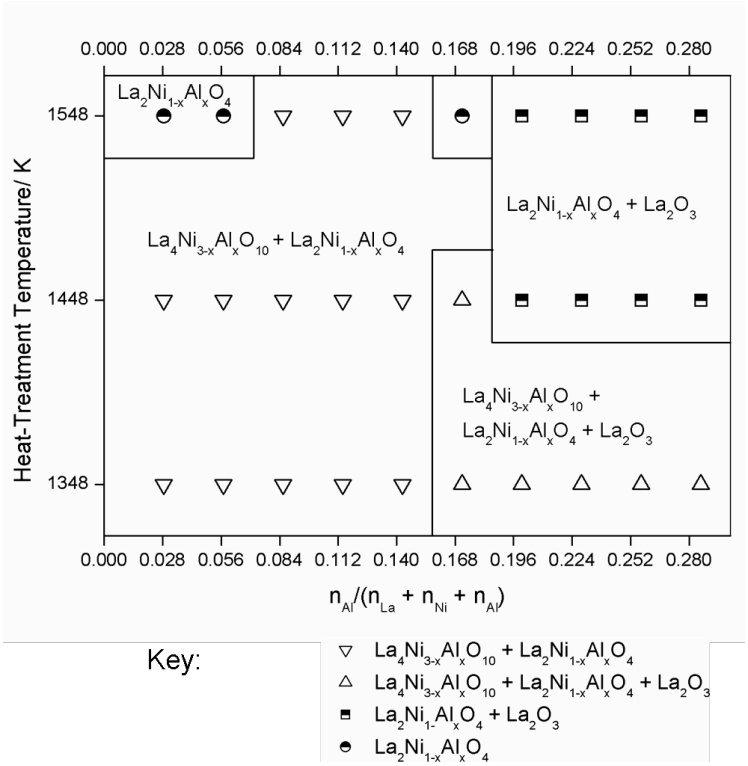

Figure 6.6. Phase diagram at room temperature pressure for the phases formed from CHFS precursors for the compositions $La_4:Ni_{3-x}Al_x$ (where $x = 0.2 – 0.0$ and $\Delta x = 0.2$) after heat-treatment for 12 hours in air. At% of Al = $n_{Al}/(n_{La}+n_{Ni}+n_{Al})$. Each point represents a unique composition, some of which are mixtures and some of which are phase pure compounds. In each case the phase identified from powder XRD is given in the key.

It was found that when Al-doped structure was formed from the nano-precursors in the ration $La_4:Ni_{3-x}Al_x$ the lanthanum nickelate, $La_4Ni_{3-x}Al_xO_{10-\delta}$ could not be isolated as a phase pure material from any composition. Where $La_4Ni_{3-x}Al_xO_{10-\delta}$ was formed, the more thermodynamically stable $La_2Ni_{1-x}Al_xO_{4+\delta}$ was observed as a secondary product in each case. The compounds $La_2Ni_{0.94}Al_{0.06}O_{4+\delta}$, and $La_2Ni_{0.87}Al_{0.13}O_{4+\delta}$ (nominal compositions) although appeared phase pure were not selected for further characterisations due to obvious inhomogeneities meaning a range of different crystallites were present in each sample.

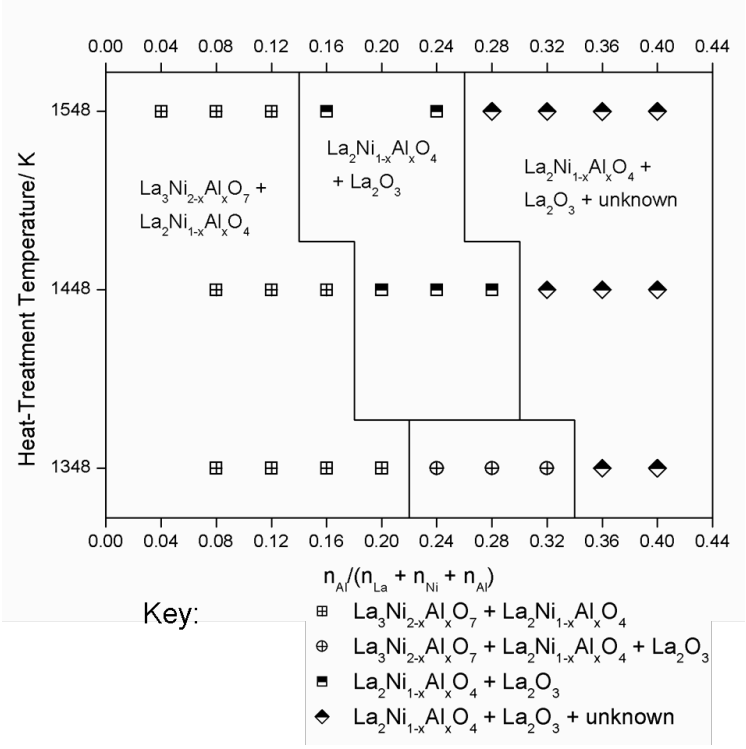

Figure 6.7. Phase diagram at room temperature pressure for the phases formed from CHFS precursors for the compositions $La_3:Ni_{2-x}Al_x$ (where $x = 0.2 – 0.0$ and $\Delta x = 0.2$) after heat-treatment for 12 hours in air. At% of Al = $n_{Al}/(n_{La}+n_{Ni}+n_{Al})$. Each point represents a unique composition, some of which are mixtures and some of which are phase pure compounds. In each case the phase identified from powder XRD is given in the key.

When precursors were in the ratio of $La_3:Ni_{2-x}Al_x$ (where $x = 0.2 – 0.0$ and $\Delta x = 0.2$) no phase pure materials were isolated from any of the nano-precursor compositions. Possibly as a result of the increased oxidation state of the B-site after the introduction increasing amounts of Al(III) When the Al content was >28 at % ($x = 1.4$) in the starting material, an unknown phase was observed that was characterised by strong broad reflections. This phase could not be identified from database patterns, and it was not possible to index the Bragg reflections, which are presented in table 6.1. It was most likely that this phase was related to an Al_xO_y phase due to the high Al content in the compositions where this phase was observed.

Table 6.1. Bragg reflection positions and intensities of the unknown phase. λ = 0.825441(3) Å

2 θ / °	I_{hkl} / counts
8.35	63616
10.39	12566
14.49	43206
14.86	62001
19.04	9764
20.83	48965
22.22	10083
25.48	31010
32.97	10021
35.65	9346
39.14	11391
41.27	6188
43.94	6928

6.3.1.4. Ga Structures

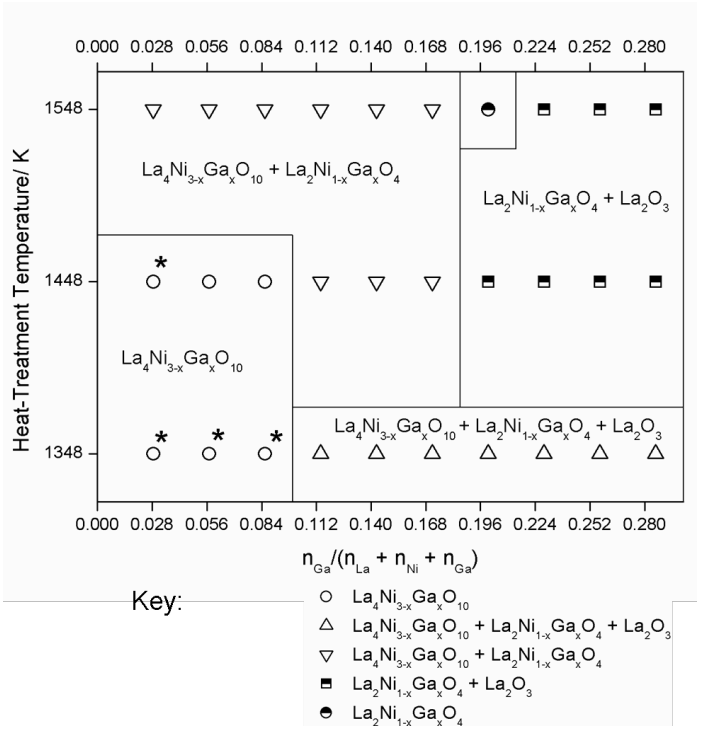

Figure 6.8. Phase diagram at room temperature pressure for the phases formed from CHFS precursors for the compositions $La_4:Ni_{3-x}Ga_x$ (where x = 0.2 – 0.0 and Δx = 0.2) after heat-treatment for 12 hours in air. At% of Ga = $n_{Ga}/(n_{La}+n_{Ni}+n_{Ga})$. Each point represents a unique composition, some of which are mixtures and some of which are phase pure compounds. In each case the phase identified from powder XRD is given in the key. Samples marked with an asterisk were selected for further investigation.

Where Ga was used as a B-site dopant, $La_4Ni_{3-x}Ga_xO_{10-\delta}$ was observed as a single phase product at three x values of 0.2, 0.4 and 0.6 at both 1348 and 1448 K. The maximum doping level achieved was *ca.* 9 at% ($La_4Ni_{2.4}Ga_{0.6}O_{10-\delta}$, nominal formula) above this value of x, $La_2Ni_{1-x}Ga_xO_{4+\delta}$ was identified as a second phase, possibly as a result of an increased M(III) content on the lanthanum nickelate B-site. The x = 0.7 composition that appeared to be phase-pure $La_2Ni_{0.3}Ga_{0.7}O_{4+\delta}$ was observed, (nominal formula) however on closer inspection a NiO secondary phase was observed after heat-treatment at 1548 K. All other heat-treated products were phase mixtures as shown in figure 6.8.

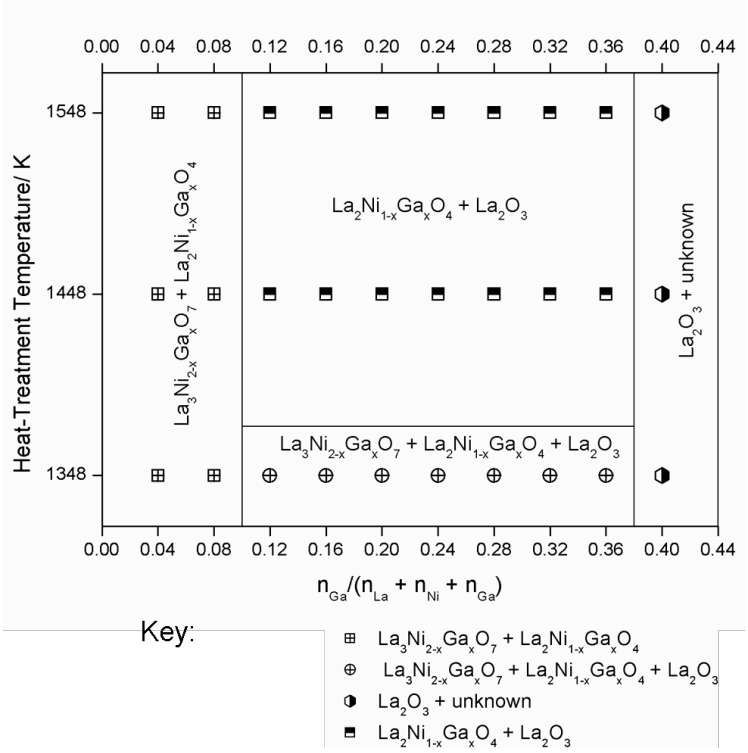

Figure 6.9. Phase diagram at room temperature pressure for the phases formed from CHFS precursors for the compositions La_3:$Ni_{2-x}Ga_x$ (where x = 0.2 – 0.0 and Δx = 0.2) after heat-treatment for 12 hours in air. At% of Ga = $n_{Ga}/(n_{La}+n_{Ni}+n_{Ga})$. Each point represents a unique composition, some of which are mixtures and some of which are phase pure compounds. In each case the phase identified from powder XRD is given in the key.

When the CHFS precursors were in a La_3:$Ni_{2-x}Ga_x$ ratio (where x = 0.2 – 0.0 and Δx = 0.2) no phase pure material was identified after heat-treatments. Some $La_3Ni_{2-x}Ga_xO_{7-\delta}$ was observed, however, this always occurred with a $La_2Ni_{1-x}Ga_xO_{4+\delta}$ secondary phase. It was not clear whether this was as a result of an incomplete

reaction or a decomposition phase at this stage. Given the 'rapid' reactions of CHFS nanoparticles and the stability of the $La_2NiO_{4+\delta}$ phase, it was more likely that the latter reason is correct.

6.3.2. Further Characterisation

Samples which appeared to be phase pure following rapid analysis were selected for further structural investigation. Each selected sample was marked with an asterisk in the phase diagrams and is listed in table 6.2. Data suitable for Rietveld refinement were collected on the I11 beamline using the MAC detectors and a collection time of 30 minutes.

Table 6.2. Samples identified for further characterisation following the initial screen.

Heat-Treatment / K	Nominal Formula
1548	$La_2Ni_{0.9}Pd_{0.1}O_{4+\delta}$
1548	$La_2Ni_{0.8}Pd_{0.2}O_{4+\delta}$
1548	$La_2Ni_{066}Pd_{0.33}O_{4+\delta}$
1548	$La_2Ni_{0.6}Pd_{0.4}O_{4+\delta}$
1348	$La_4Ni_{2.8}Ga_{0.2}O_{10-\delta}$
1448	$La_4Ni_{2.8}Ga_{0.2}O_{10-\delta}$
1348	$La_4Ni_{2.6}Ga_{0.4}O_{10-\delta}$
1348	$La_4Ni_{2.4}Ga_{0.6}O_{10-\delta}$

6.3.2.1. $La_2Ni_{1-x}Pd_xO_{4+\delta}$ structures

Structures where the nominal Pd content, *x*, was 0.1, 0.2, 0.33 and 0.4 were further investigated using higher resolution data collected from the MAC detectors. All *hk0* reflections showed halved intensity that suggested an orthorhombic distortion of the tetragonal *I4/mmm* phase to the *Fmmm* sub-group. Le Bail refinements using the Fmmm space group were successful as shown in figure 6.10. Refined values for each phase are presented in table 6.3.

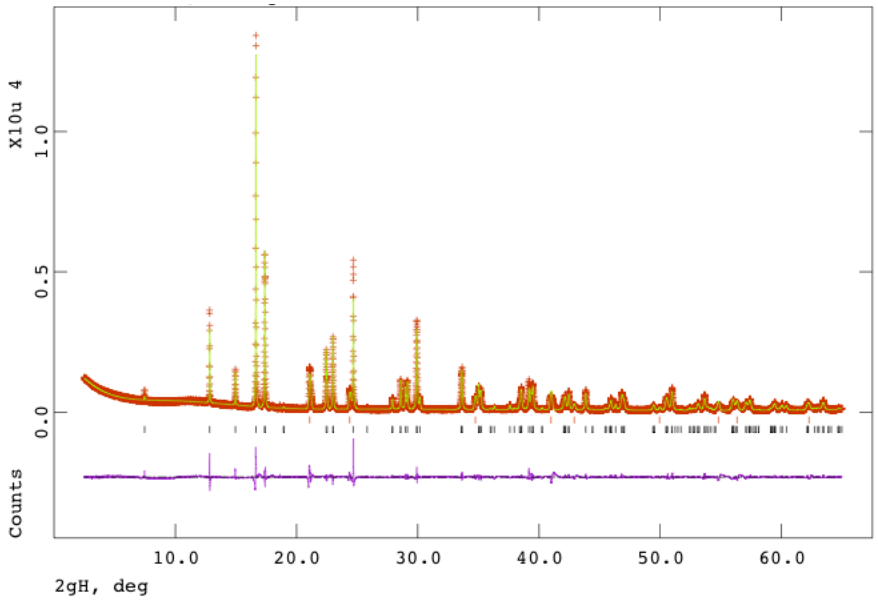

Figure 6.10. Le Bail refinement of $La_2Ni_{0.67}Pd_{0.33}O_{4+\delta}$ (nominal composition). $R_{wp} = 0.1163$, $R_p = 0.0796$, $\chi^2 = 2.781$. Measured data points are shown in red, calculated profile is shown in green and the difference shown in purple. Vertical tickmarks show the calculated peak positions for orthorhombically distorted $La_2Ni_{0.67}Pd_{0.33}O_{4+\delta}$ phase (lower) and NiO (upper) respectively.

Table 6.3. Refined values for $La_2Ni_{1-x}Pd_xO_{4+\delta}$ structures.

Nominal Pd content	Space Group	*a* / Å	*b* / Å	*c* / Å	*vol* / Å^3	Orthorhombic Strain / Å
0.1	Fmmm	5.45881(7)	5.46851(7)	12.6842(1)	378.642(5)	0.0018
0.2	Fmmm	5.45804(6)	5.46951(6)	12.6902(1)	378.836(5)	0.0021
0.33	Fmmm	5.45755(6)	5.46782(6)	12.6894(1)	378.664(8)	0.0019
0.4	Fmmm	5.46259(4)	5.47466(4)	12.6906(1)	379.552(3)	0.0022

On closer examination some stoichiometric NiO was present in each of the structures. The NiO Bragg peaks were all asymmetric, which suggested that it was not homogeneous NiO as shown in figure 6.11.

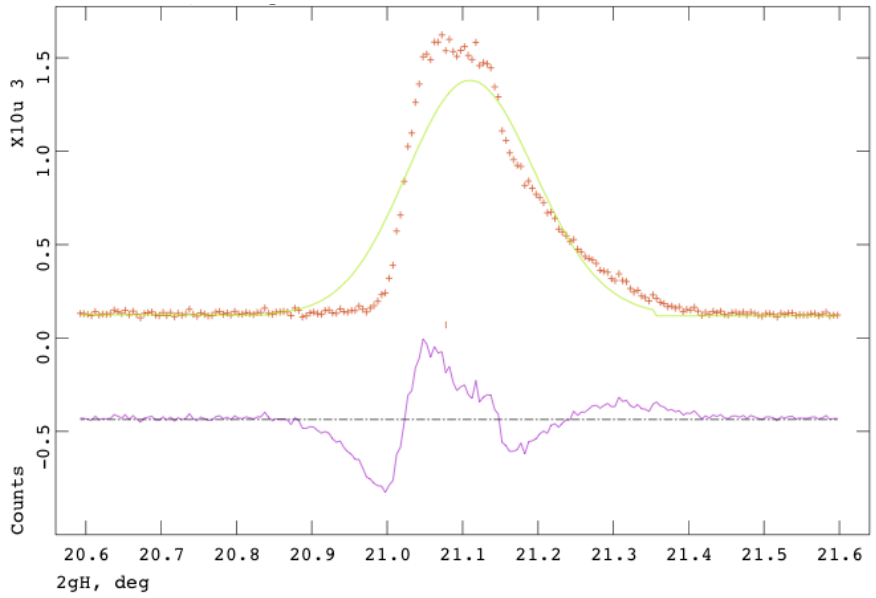

Figure 6.11. The NiO (111) reflection demonstrating the asymmetry, and hence the inhomogeneity. Measured data points are shown in red, calculated profile is shown in green and the difference shown in purple. The vertical tickmark shows the calculated peak position for NiO.

The implication of this was that some of the Pd had reacted with NiO to form an inhomogeneous solid solution (crystallites with varying unit cell sizes). The nominal Pd content was therefore not representative of the actual Pd content in the lanthanum nickelate compound. The consequence being that Vegard's law was not observed when relating cell volume to nominal Pd content, as shown in figure 6.12. Further to this, Rietveld refinement was not possible on any structures due to the uncertainty in the Pd content.

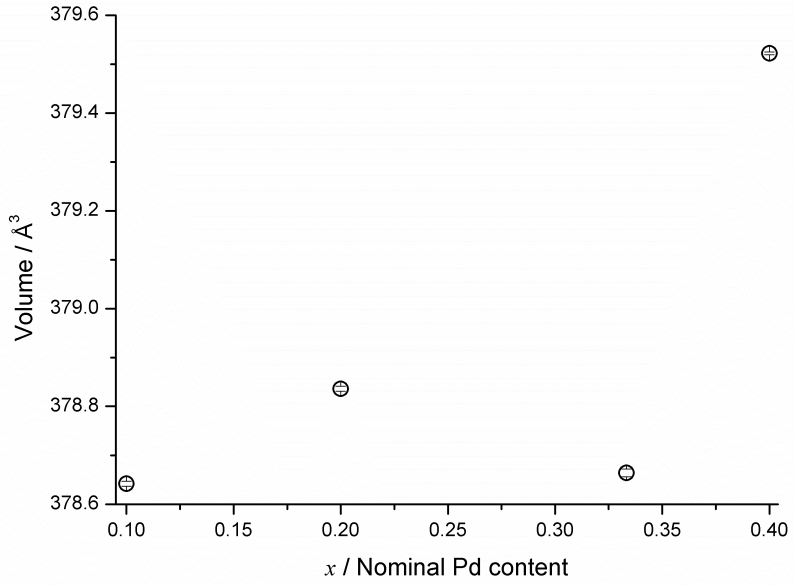

Figure 6.12. Graph showing change in unit cell volume with nominal Pd content in $La_2Ni_{1-x}Pd_xO_{4+\delta}$. Error bars are smaller than symbols in all cases.

The orthorhombic strain, which is given by equation 6.1 was approximately 0.002 Å in each case.

$$s = 2(b - a)/(b + a) \quad \textbf{(6.1)}$$

This was most likely caused as a result of the increased ionic radius of Pd^{2+} in comparison to Ni^{2+}, r^{2+} = 0.86 and 0.69 Å respectively.

6.3.2.2. $La_4Ni_{3-x}Ga_xO_{10-\delta}$ structures.

Le Bail refinements on data collected using the MAC detectors was used to confirm that $La_4Ni_{3-x}Ga_xO_{10-\delta}$ had been formed in each case. Each $La_4Ni_{3-x}Ga_xO_{10-\delta}$ phase crystallised in the orthorhombic Bmab space group.

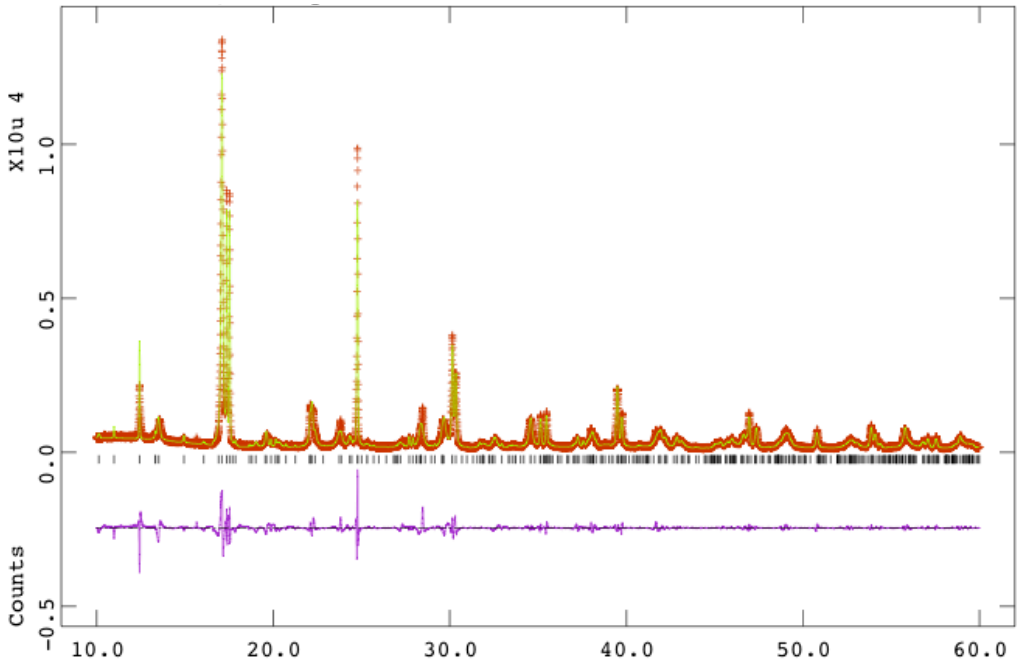

Figure 6.13. Le Bail refinement of $La_4Ni_{2.8}Ga_{0.2}O_{10-\delta}$ (nominal formula) using the Bmab space group. $R_{wp} = 0.1281$, $R_p = 0.0894$, $\chi^2 = 6.806$.

The phase boundary could be extended up to maximum nominal Ga content of $x = 0.6$ Ga on Ni sites, however this composition was confirmed using EDX spectroscopy as $La_{4.35}Ni_{2.39}Ga_{0.36}O_{10-\delta}$. In order to find the reason for the low Ga content, SEM micrographs of the same area of the $La_{4.35}Ni_{2.39}Ga_{0.36}O_{10-\delta}$ composition were recorded using both a secondary electron detector and a back-scatter electron detector shown in figure 6.14. The back-scatter electron detector records electrons scattered back after irradiation of the electron beam. Since atoms with different atomic numbers have different scattering powers, separate phases would appear as they would scatter by a separate amount and therefore appear as a different contrast in the image.

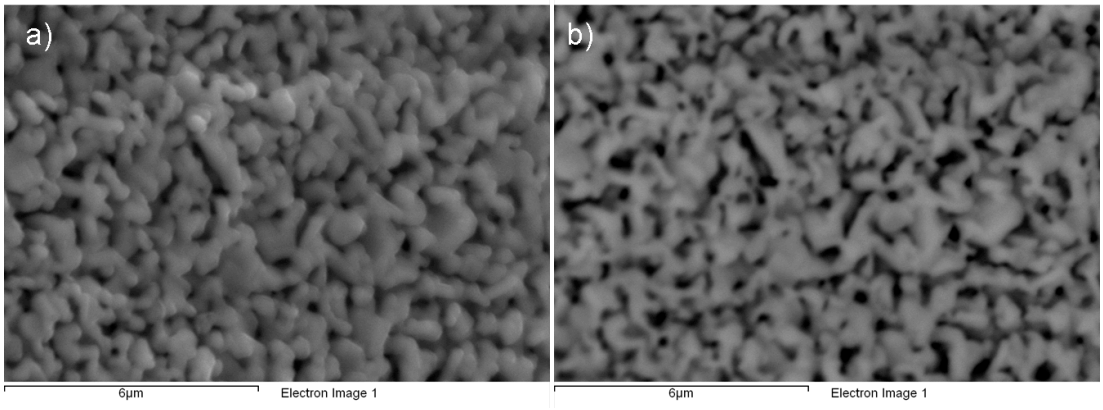

Figure 6.14. SEM micrograph of $La_{4.35}Ni_{2.39}Ga_{0.36}O_{10-\delta}$ recorded using: a) secondary electron detector, and b) back-scatter electron detector.

It is clear from the back-scatter image that only one phase was observed. It can be assumed that therefore the lower than expected Ga content was caused by an incomplete precipitation from the nitrate salt. It should also be noted that the total metal content on B-sites was 2.75, lower than the expected 3, suggesting that each material has a large concentration of B-site vacancies.

Inhomogeneities were observed in each sample, characterised by asymmetric Bragg peaks suggesting a range of crystallites. This is shown in figure 6.15., in which a magnified section of the $La_4Ni_{2.6}Ga_{0.4}O_{10-\delta}$ diffraction pattern shows clear peak asymmetry.

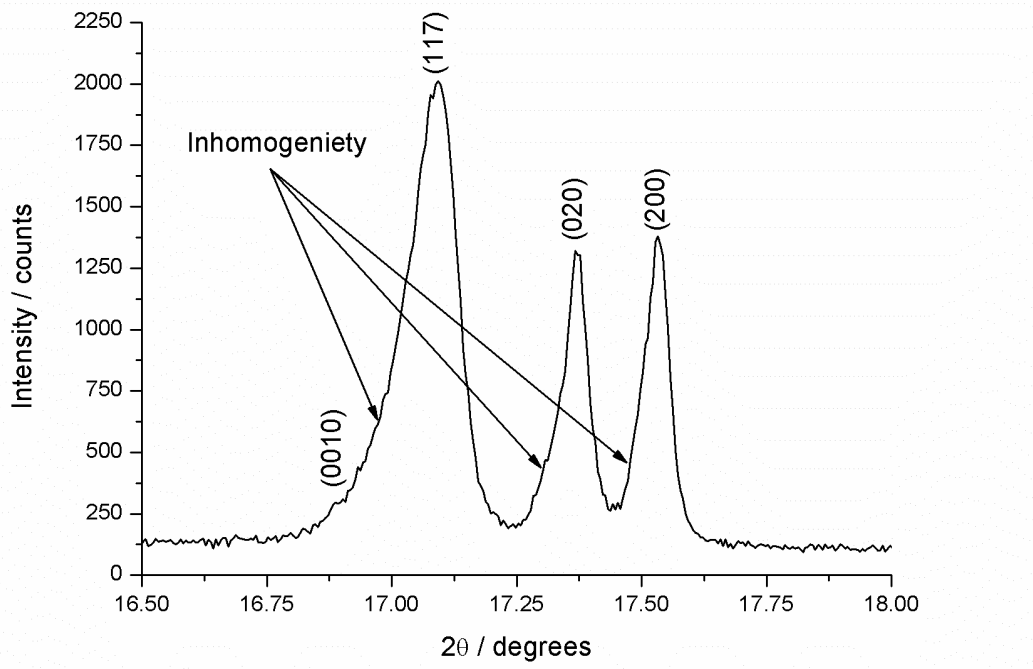

Figure 6.15. Magnified section of the $La_4Ni_{2.6}Ga_{0.4}O_{10-\delta}$ diffraction pattern between 16.5 – 18 °2θ in which clear peak asymmetry can be observed.

As a result of the inhomogeneity Rietveld refinement was not possible. As in the case of doped lanthanum nickelates in chapter 4 and 5, anisotropic broadening was observed in the *c* direction. This was modelled using an anisotropic strain parameter, Γ^2_S and varied with sample and heat-treatment, this value served to represent the extent of the anisotropy, not the amount of strain in the crystallite. The anisotropic broadening could have been caused by particle size or strain effects as previously discussed in chapters 4 and 5. Unit cell parameters extracted from the Le Bail refinements are presented in table 6.4. The values are plotted with increasing nominal Ga content in figure 6.16. Figure 6.16 shows that as nominal Ga content increased, the *a* and *b* parameters did not increase and the only increase in size was observed in the *c* direction. This contradicts the result seen in chapter 5 (page 123) where Fe^{3+} substitutions on the Ni site caused an increase in all three directions. This difference in behaviour could have been as a result of Ga^{3+} preferentially substituting onto La^{3+} sites. Given the increased ionic radius of Ga(III) in comparison to Ni(III) and Fe(III) this is a plausible explanation. Also the Ni sites in $La_4Ni_3O_{10-\delta}$ have an average valence of approximately 2.67,(Zhang et al. 1995) Ga may have been more electronically stable on the La site which has a valence of 3+.

Table 6.4. Refined unit cell values for all $La_4Ni_{3-x}Ga_xO_{10-\delta}$ compounds.

Nominal Ga content / *x*	Heat-treatment / K	*a* / Å	*b* / Å	*c* / Å	*Vol* / Å	Γ^2_s
0.2	1348	5.42053(5)	5.47023(5)	28.084(1)	832.74(2)	76.8
0.2	1448	5.42060(7)	5.46953(7)	28.189(1)	835.70(3)	118.76
0.4	1448	5.42045(9)	5.47027(9)	28.151(1)	834.72(4)	290.57
0.6	1448	5.41630(5)	5.46337(7)	28.328(2)	838.31(5)	141.40

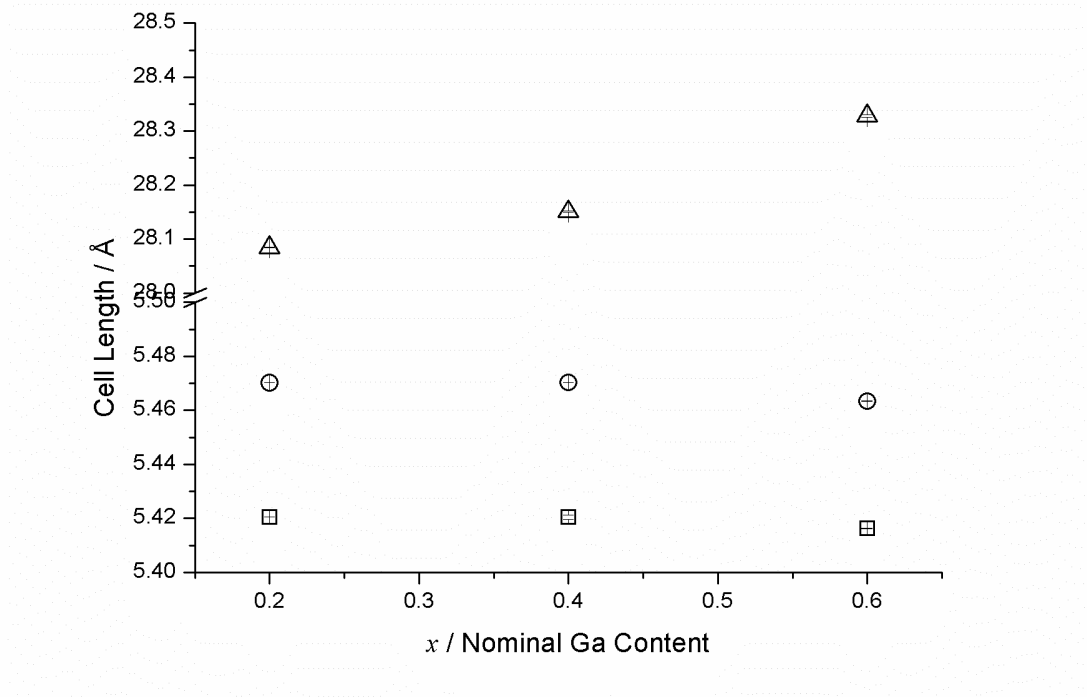

Figure 6.16. Variation in unit cell parameters with increasing Ga content in $La_4Ni_{3-x}Ga_xO_{10-\delta}$ compositions. Squares = *a* parameter, circles = *b* parameter, and triangles = *c* parameter.

6.4. Conclusions

In conclusion, a rapid synthesis and structural screening method was used to investigate 240 different heterometallic oxides in a single experiment. Samples were synthesised at a rate of 9 samples per hour meaning 80 samples were synthesised in 9 hours and all 240 compositions could be generated in a matter of a day or so. By splitting each composition into three large and heat-treating at three different temperatures, large area of compositional phase space could be investigated in a single experiment. This allowed reaction conditions to be optimised particularly in the case of the $La_2Ni_{1-x}Pd_xO_{4+\delta}$ structures which could only be synthesised in a small

compositional and temperature range. The advantage of using synchrotron based diffraction is highlighted by demonstrating not only the speed of high-resolution data collection (120 samples per hour) but that once potentially interesting composition had been identified from a rapid screen, they were then further investigated using higher-resolution data collection as part of the same experiment. In this manner 16 previously unknown in the literature compositions were identified from a total of 240 compositions. If one were to repeat the experiment using a heat and grind technique given the 96 hour reaction time reported by Greenblatt *et al.*(Zhang et al. 1995) this would take 23040 hours or nearly 1000 days or about 3 years.

Chapter 7 — Further Work

1.) In part of this thesis the possibility of creating a high-throughput materials discovery process was investigated. In chapter 6, 240 samples were made in a single experiment demonstrating the potential for this process for the discovery of complex metal oxides. To convert the high-throughput process to a combinatorial one, the data from this experiment must be used to direct further high-throughput 'screens'. This could be accomplished by using computer predictions of structure and properties to direct studies prior to synthesis. Subsequently the results should be analysed using a data-mining (chemometrics) approach, to direct the next study. By using an iterative method such as this, much larger areas of phase space and properties could be investigated and the potential to search many thousand compositions could be achieved.

2.) If the above idea is to be achieved, a greater amount of information regarding each composition will be required in order to direct the next iteration. A high-throughput method of measuring the properties of each composition will be required. Due to the large number of compositions possible, the number will have to be reduced following an initial structural screen to then allow screening of properties to progress. Some ideas regarding a multi-station 4-point probe to measure DC conductivity have been investigated this could be achieved through miniaturisation, of pellets. The multi-station probe would be constructed with about 20 – 25 stations that could accommodate pellets of about 2 – 3 mm diameter. The main issue which prevented the construction of this piece of equipment was creating an identical good contact on all pellets. However as of now no probe has yet been built that could test these ideas. When screening SOFC materials a wide range of properties are required in a good material. In this thesis electronic conductivity was used as a screening method, however a high electronic conductivity does not necessarily give a good SOFC material. In future work it would be important to look at other properties to screen. In relation to oxide materials, the most important property is perhaps the oxygen content, which would give an idea of the oxide ion mobility. Also it would give a greater idea of the vacancy structure which can have a large effect on the properties of these materials. The best way to measure the oxygen content is through thermogravimetric analysis in a reducing environment, which is a batch type process

and would be difficult to create a high-throughput version. In the future therefore thermogravimetric analysis in a reducing atmosphere should be used as part of a third screen.

3.) In this thesis supercritical water (T_c = 647 K) was used as a solvent. Supercritical ethanol and methanol (T_c = 513 K) have a lower critical temperature, T_c than water. The reactions that occurred in this thesis could probably be achieved at lower temperatures if an ethanol or methanol plus water mix were used. Crystallisation would potentially be better at lower temperatures due to the increased mass transport in supercritical ethanol and methanol, allowing direct access to compounds such as perovskites which would normally require heating at temperatures > 873 K. The *in situ* reaction between $La(OH)_3$ and $Ni(OH)_2$ showed that during the first 30 minutes of this reaction hydroxides converted to oxides. If a more crystalline oxide starting material were used this reaction time could be reduced accordingly. At lower temperatures organic solvents and metal complexes could potentially survive the conditions, meaning that the high-throughput process may also be applied to a far wider range of materials.

4.) This thesis concentrated on the synthesis of lanthanum nickelate Ruddlesden-Popper phases. Other layered perovskites have been identified as potential SOFC cathode materials including layered double perovskites which have the formula $AA'BB'O_{5\pm\delta}$ and are described in section 1.1.3. These materials have been identified as having a high electrical conductivity coupled with a large variable oxygen stoichiometry leading to high oxide ion mobility. These materials have a wide range of elemental combinations, meaning a lot of potential compositions, which would be laborious to search in a manual manner. In the future the possibility of exploring a wider range of materials should be pursued.

Chapter 8 — Conclusions

1.) Heterometallic layered metal oxides have been traditionally made by heating and grinding metal oxide precursors until a thermodynamic product is isolated. Many new routes have been developed that reduce diffusion distances and allow the reaction to proceed faster. Previously CHFS was used to synthesise nano-precursors to the Ruddlesden-Popper series $La_{n+1}Ni_nO_{3n+1}$ (where n = 1, 2, and 3) which could then be reacted to make the desired phase in a considerably shorter time than could be done using heat and grind methods. This was achieved by reducing diffusion distances between the reactants therefore increasing mass transport. Solid-solid reactions at nano length scales have been shown to proceed through a largely amorphous intermediate making nucleation of the crystalline phase from the amorphous mixture the rate limiting step. *In situ* powder X-ray diffraction was used to observe the reaction between $La(OH)_3$ and $Ni(OH)_2$, which formed a largely amorphous intermediate (some interfacial diffusion still occurring) after *ca.* 30 minutes. Nucleation and growth of $La_2NiO_{4+\delta}$ then occurred from this intermediate producing a phase pure compound in just 78 minutes, 4.5 times faster than when using a more traditional approach (6 hours). This was also achieved at a temperature 140 K lower than previously observed. The Hypothesis 1 suggested that this route to layered heterometallic oxides could be used to synthesise doped variations of these materials rapidly and in a single step. It was thought that due to the low energy synthesis route, previously unidentified compositions may be discovered. The intimacy of mixing of the nano-precursors may have reduced the energy barrier to synthesis and as such resulted in increased phase boundaries. Doping studies carried out in chapters 4, 5, and 6 confirmed that doped layered heterometallic metal oxides can be rapidly formed from CHFS coprecipitates in 12 hours. Particularly, chapter 5 and 6 demonstrated the ability to synthesise materials with increased phase boundaries than those that have been previously reported in the literature, for example $La_4Ni_2FeO_{10-\delta}$ (chapter 5).

2.) High-throughput synthesis of metal oxides is currently gaining interest; however is not as mature as in the drug discovery field. The main barrier to rapid materials discovery of ceramics are the high-energy multistep processes often required to synthesise new materials from parent oxides. CHFS can produce nano-ceramics with

reduced diffusion distances, and therefore increased mass transfer. The CHFS synthesis was adapted into a high-throughput process described in chapter 4. Chapter 4 demonstrated a new methodology of high-throughput synthesis, using HiTCH flow synthesis. Manually a number of intimately mixed solid ceramic nano-precursors were synthesised, and then split into three daughter libraries. The libraries were heat-treated at 1348, 1448, and 1548 K, respectively, in order to make and screen a wide range of compositional phase space in a single experiment. Four new to the literature compositions: $La_4Ni_{2.7}V_{0.3}O_{10-\delta}$, $La_4Ni_{2.7}Cr_{0.3}O_{10-\delta}$, $La_4Ni_{2.7}Mn_{0.3}O_{10-\delta}$ and $La_4Ni_{2.7}Al_{0.3}O_{10-\delta}$ were identified, and tested for DC conductivity. This work represented the first time a solid-state combinatorial approach had been applied to these kind of layered metal oxides. The approach allowed the rapid optimisation of reaction conditions (for example synthesis temperature) by synthesising the materials in parallel over a range of temperatures.

3.) Chapter 4 demonstrated a new manual high-throughput approach to synthesise layered heterometallic oxides. In chapter 5 and 6, a combinatorial robot previously used for the synthesis of nanomaterials, was programmed to synthesise a range of nano-precursors for the $La_4Ni_{3-x}Fe_xO_{10-\delta}$ series using the same daughter library methodology seen in chapter 4. The automation represented a further increase in the speed of discovery with 80 nano-precursor samples being made in *ca.* 9 hours, which once split into daughter libraries enabled the synthesis of 240 samples in a matter of a day or so. The structural screening method used meant that two screening rounds were required to identify the compounds of most interest. Chapter 6 therefore demonstrates a high-resolution rapid screening method that can identify phase boundaries and optimise reaction conditions for layered metal oxides. It also shows the potential of the automated methodology by synthesising many hundreds of samples (240) in a single experiment.

4.) In summary, fuel cells, batteries and other electrochemical devises all require a range of materials with different functionalities to run efficiently. A new range of complex heterometallic oxides have been identified recently that fulfil many of these roles. To date their synthesis has required many different multi-step processes that require high temperatures to complete. This thesis represents not only a new lower

energy route to these important new compounds, but the first demonstration of a high-throughput nanoceramics method to identify them.

References

Adschiri, T., Hakuta, Y., & Arai, K. 2000, "Hydrothermal Synthesis of Metal Oxide Fine Particles at Supercritical Conditions", *Industrial and Engineering Chemistry Research*, vol. 39, pp. 4901-4907.

Adschiri, T., Kanazawa, K., & Arai, K. 1992, "Rapid and Continuous Hydrothermal Crystallization of Metal Oxide Particles in Supercritical Water", *Journal of the American Ceramic Society*, vol. 4, pp. 1019-1022.

Amow, G., Au, J., & Davidson, I. 2006a, "Synthesis and Characterisation of $La_4Ni_{3-x}Co_xO_{10+\delta}$ ($0.0 < x < 3.0$, $\Delta x = 0.2$) for Solid Oxide Fuel Cells", *Solid State Ionics*, vol. 177, pp. 1837-1841.

Amow, G., Davidson, I., & Skinner, S. J. 2006b, "A Comparative Study of the Ruddlesden-Popper Series, $La_{n+1}Ni_nO_{3n+1}$ (n = 1, 2 and 3), for Solid-Oxide Fuel-Cell Cathode Applications", *Solid State Ionics*, vol. 177, pp. 1205-1210.

Anderson, P. S., Guerin, S., Hayden, B. E., Han, Y., Pasha, M., Whittle, K. R., & Reaney, I. M. 2009, "Optimisation of Synthesis of the Solid Solution $Pb(Zr_{1-x}Ti_x)O_3$ on a Single Substrate using a High-Throughput Modified Molecular-Beam Epitaxy Method", *Journal of Materials Research*, vol. 24, pp. 164-172.

Azad, A. M., Larose, S., & Akbar, S. A. 1994, "Bismuth Oxide Based Solid Electrolytes for Fuel Cells", *Journal of Materials Science*, vol. 29, pp. 4135-4351.

Balkenhohl, F., Bussche-Hünnefeld, C., Lansky, A., & Zechel, C. 1996, "Combinatorial Synthesis of Small Organic Molecules", *Angewandte Chemie International Edition*, vol. 35, pp. 2288-2337.

Bannikov, D. O. & Cherepanov, V. A. 2006, "Thermodynamic Properties of Complex Oxides in the La-Ni-O System", *Journal of Solid State Chemistry*, vol. 179, pp. 2721-2727.

Carey, G. H. & Dahn, J. R. 2011, "Combinatorial Synthesis of Mixed Transition Metal Oxides for Lithium-Ion Batteries", *ACS Combinatorial Chemistry*, vol. 13, pp. 186-189.

Carvalho, M. D., Wattiaux, A., Ferreira, L. P., & Bassat, J. M. 2009, "Mössbauer Investigation of ^{57}Fe doped $La_4Ni_3O_{10\pm y}$ phases", *Journal of Solid State Chemistry*, vol. 182, pp. 60-64.

Chaudhry, A. A., Haque, S., Kellici, S., Boldrin, P., Rehman, I., Khalid, F. A., & Darr, J. A. 2006, "Instant Nano-Hydroxyapatite: a Continuous and Rapid Hydrothermal Synthesis", *Chemical Communications* pp. 2286-2288.

Choi, J., Park, H., & Hoffmann, M. R. 2010, "Combinatorial Doping of TiO_2 with Platinum (Pt), Chromium (Cr), Vanadium (V), and Nickel (Ni) to Achieve Enhanced Photocatalytic Activity with Visible Light Irradiation", *Journal of Materials Research*, vol. 25, pp. 149-158.

Cockcroft, J. K., Alexander, S. J., Mason, S. A., and Darr, J. A. 2011, Revealing the Nature of Phase Discontinuity in the Ceria-Yttira Binary System. Unpublished Work

Cushing, B. L., Kolesnichenko, V. L., & O'Connor, C. J. 2004, "Recent Advances in the Liquid-Phase Synthesis of Inorganic Nanoparticles", *Chemical Reviews*, vol. 104, pp. 3893-3946.

Darr, J. A. & Poliakoff, M. 1999, "New Directions in Inorganic and Metal-Organic Coordination Chemistry in Supercritical Fluids", *Chemical Reviews*, vol. 99, pp. 495-541.

Ding, J., Bao, J., Sun, S., Luo, Z., & Gao, C. 2009, "Combinatorial Discovery of Visible-Light Driven Photocatalysis Based on the ABO_3 type (A = Y, La, Nd, Sm, Eu, Gd, Dy, Yb, B = Al and In) Binary Oxides", *Journal of Combinatorial Chemistry*, vol. 11, pp. 523-526.

Doshi, R., Alcock, C. B., Gunasekaran, N., & Carberry, J. J. 1993, "Carbon Monoxide and Methane Oxidation Properties of Oxide Solid Solution Catalysts", *Journal of Catalysis*, vol. 140, pp. 557-563.

Drews, J. 2000, "Drug Discovery: A Historical Perspective", *Science*, vol. 287, pp. 1960-1964.

Fister, L. & Johnson, D. C. 1992, "Controlling Solid-State Reaction Mechanisms Using Diffusion Length in Ultra-thin Superlattice Composites", *Journal of the American Chemical Society*, vol. 114, pp. 4639-4644.

Frischat, G. H. 1974, "Mass Transport in Solids", *Angewandte Chemie International Edition*, vol. 13, pp. 384-398.

Fujimoto, K., Takada, K., Sasaki, T., & Watanabe, M. 2004, "Combinatorial Approach for Powder Preparation of Pseudo-Ternary System $LiO_{0.5}$-X-$LiTiO_2$ (X: $FeO_{1.5}$, $CrO_{1.5}$ and NiO)", *Applied Surface Science*, vol. 223, pp. 49-53.

Fukushima, Y. 2000, "Application of Supercritical Fluids", *R&D Review of Toyota CRDL*, vol. 35, pp. 1-9.

Galkin, A. A., Kostyuk, B. G., Lunin, V. V., & Poliakoff, M. 2000, "Continuous Reactions in Supercritical Water: A New Route to La_2CuO_4 with a High Surface Area and Enhanced Oxygen Mobility", *Angewandte Chemie International Edition*, vol. 39, pp. 2738-2740.

Gopalakrishnan, J. 1995, "Chimie Douce Approaches to the Synthesis of Metastable Oxide Materials", *Chemistry of Materials*, vol. 7, pp. 1265-1275.

Gösele, U. & Tu, K. N. 1989, ""Critical Thickness" of Amorphous Phase Formation in Binary Diffusion Couples", *Journal of Applied Physics*, vol. 66, pp. 2619-2626.

Guerin, S. & Hayden, B. E. 2006a, "Physical Vapour Deposition Method for the High-Throughput Synthesis of Solid State Material Libraries", *Journal of Combinatorial Chemistry*, vol. 8, pp. 66-73.

Guerin, S., Hayden, B. E., Lee, C. E., Mormiche, C., & Russell, A. E. 2006b, "High-Throughput Synthesis and Screening of Ternary Metal Alloys for Electrocatalysis", *Journal of Physical Chemistry B*, vol. 110, pp. 14355-14362.

Guerin, S., Hayden, B. E., & Smith, D. C. A. 2008, "High-Throughput Synthesis and Screening of Hydrogen Storage Alloys", *Journal of Combinatorial Chemistry*, vol. 10, pp. 37-43.

Haeni, J. H., Theis, C. D., Schlom, D. G., Tian, W., Pan, X. Q., Chang, H., Takeuchi, I., & Xiang, X. D. 2001, "Epitaxial Growth of the First Five Members of the $Sr_{n+1}Ti_nO_{3n+1}$ Ruddlesden-Popper Homologous Series", *Applied Physics Letters*, vol. 78, pp. 3292-3294.

Hakuta, Y., Ura, H., Hayashi, H., & Arai, K. 2005, "Effects of Hydrothermal Synthetic Conditions on the Particle Size of γ−AlO(OH) in Sub and Supercritical Water Using a Flow Reaction System", *Materials Chemistry and Physics*, vol. 93, pp. 466-472.

Ham, W. K., Holland, G. F., & Stacy, A. M. 1988, "Low Temperature Synthesis of Superconducting $La_{2-x}M_xCuO_4$: Direct Precipitation from NaOH/KOH Melts", *Journal of the American Chemical Society*, vol. 110, no. 5214, p. 5215.

Hench, L. L. & West, J. K. 1990, "The Sol-Gel Process", *Chemical Reviews*, vol. 90, pp. 33-72.

Hungría, T., Lisoni, J. G., & Castro, A. 2002, "$Sr_3Ti_2O_7$ Ruddlesden-Popper Phase Synthesis by Milling Routes", *Chemistry of Materials*, vol. 14, pp. 1747-1754.

Hyett, G., Green, M., & Parkin, I. P. 2006, "X-ray Diffraction Area Mapping of Preferred Orientation and Phase Change in TiO_2 Thin Films Deposited by Chemical Vapour Deposition", *Journal of the American Chemical Society*, vol. 128, pp. 12147-12155.

Hyett, G., Green, M. A., & Parkin, I. P. 2007, "The Use of Combinatorial Chemical Vapour Deposition in the Synthesis of $Ti_{3-\delta}O_4N$ with $0.06 < \delta < 0.25$: A Titanium Oxynitride Phase Isostructural to Anosovite", *Journal of the American Chemical Society*, vol. 128, pp. 15541-15548.

Jacobson, A. J. 2010, "Materials for Solid Oxide Fuel Cells", *Chemistry of Materials*, vol. 22, pp. 660-674.

Joyce, B. A. & Joyce, T. B. 2004, "Basic Studies of Molecular Beam Epitaxy-Past, Present and Some Future Directions", *Journal of Crystal Growth*, vol. 264, pp. 605-619.

Kahn, M., Seubsai, A., Onal, I., & Senken, S. 2010, "High Throughput Synthesis and Screening of New Catalytic Materials for the Direct Epoxidation of Propylene", *Combinatorial Chemistry and High Throughput Screening*, vol. 13, pp. 67-74.

Kanatzidis, M. G. 1997, "New Directions in Synthetic Solid State Chemistry: Chalcophosphate Salt Fluxes for the Discovery of new Multinary Solids", *Current Opinion in Solid State and Materials Science*, vol. 2, pp. 139-147.

Kellici, S., Gong, K., Lin, T., Brown, S., Clark, R. J. H., Vickers, M., Cockcroft, J. K., Middlekoop, V., Barnes, P., Perkins, J. M., Tighe, C. J., & Darr, J. A. 2010, "High-Throughput Continuous Hydrothermal Flow Synthesis of Zn-Ce Oxides: Unprecedented Solubility of Zn in the Nanoparticle Fluorite Lattice", *Philosophical Transactions of the Royal Society A*, vol. 368, pp. 4331-4349.

Kharton, V. V., Viskup, A. P., Kovalevsky, A. V., Naumovich, E. N., & Marques, F. M. B. 2001, "Ionic Transport in Oxygen Hyperstoichiometric Phases with the K_2NiF_4 Structure", *Solid State Ionics*, vol. 143, pp. 337-353.

Kim, G., Wang, S., Jacobson, A. J., Reimus, L., Brodersen, P., & Mims, C. A. 2007, "Rapid Oxygen Ion Diffusion and Surface Exchange Kinetics in $PrBaCo_2O_{5+\delta}$ with a Perovskite Related Structure and Ordered A Cations", *Journal of Materials Chemistry*, vol. 17, pp. 2500-2505.

Kim, J. H., Cassidy, M., Irvine, J. T. S., & Bae, J. 2009, "Advanced Electrochemical Properties of $LnBa_{0.5}Sr_{0.5}Co_2O_{5+\delta}$ (Ln = Pr, Sm and Gd) as Cathode Material for IT-SOFC", *Journal of the Electrochemical Society*, vol. 156, p. B682-B689.

Kiselev, E. A., Proskurnina, N. V., Voronin, V. I., & Cherepanov, V. A. 2007, "Phase Equilibria and Crystal Structures of Phases in the La-Ni-Fe-O System at 1370 K in Air", *Inorganic Materials*, vol. 43, pp. 167-175.

Klein, J., Lehmann, C. W., Schmidt, H.-S., & Maier, W. F. 1998, "Combinatorial Material Libraries on the Microgram Scale with an Example of Hydrothermal Synthesis", *Angewandte Chemie International Edition*, vol. 37, pp. 3369-3372.

Larson, A. C. & Von Dreele, R. B. 1994, "General Structure Analysis System (GSAS)", *Los Alamos National Laboratory Report LAUR* pp. 86-748.

Lashtabeg, A. & Skinner, S. J. 2006, "Solid Oxide Fuel Cells - A Challenge for Materials Chemists?", *Journal of Materials Chemistry*, vol. 16, pp. 3161-3170.

Lavrova, O. A., Somenkov, V. A., Tkalich, A. K., Shul'shtein, S. Sh., Damm, I. D., & Ivanov-Smolenskii, G. A. 1991, "High-Temperature Phase Transition in $La_4Ni_3O_{10}$", *Superconductivity*, vol. 4, pp. 1743-1745.

Lee, B., Lee, S., Jeong, H., & Sohn, K.-S. 2011, "Solid-State Combinatorial Screening of $(Sr, Ca, Ba, Mg)_2Si_5N_8:Eu^{2+}$ Phosphors", *ACS Combinatorial Chemistry*, vol. 13, pp. 154-158.

Lin, T., Kellici, S., Gong, K., Thompson, K., Evans, J. R. G., Wang, X., & Darr, J. A. 2010, "Rapid Automated Materials Synthesis Instrument: Exploring the Composition and Heat-Treatment of Nanoprecursors Toward Low Temperature Red Phosphors", *Journal of Combinatorial Chemistry*, vol. 12, pp. 383-392.

Ling, C. D. & Argyriou, D. N. 1999, "Neutron Diffraction Study of $La_3Ni_2O_7$: Structural Relationships Among n = 1, 2, and 3 Phases $La_{n+1}Ni_nO_{3n+1}$", *Journal of Solid State Chemistry*, vol. 152, pp. 517-525.

Maignan, A., Martin, C., Pelloquin, D., Nguyen, N., & Raveau, B. 1999, "Structural and Magnetic Studies of Ordered Oxygen-Deficient Perovskites $LnBaCo_2O_{5+\delta}$,

Closely Related to the "112" Structure", *Journal of Solid State Chemistry*, vol. 142, pp. 247-260.

McIntosh, S. & Gorte, R. J. 2004, "Direct Hydrocarbon Solid Oxide Fuel Cells", *Chemical Reviews*, vol. 104, pp. 4845-4865.

Meng, W. J., Nieh, C. W., Ma, E., Fultz, B., & Johnson, W. L. 1988, "Solid State Interdiffusion Reactions of Ni/Zr Diffusion Couples", *Materials Science and Engineering*, vol. 97, pp. 87-91.

Mohan Ram, R. A., Ganapathi, L., Ganguly, P., & Rao, C. N. R. 1986, "Evolution of Three-Dimensional Character Across the $La_{n+1}Ni_nO_{3n+1}$ Homologous Series with Increase in *n*", *Journal of Solid State Chemistry*, vol. 63, pp. 139-147.

Novet, T. & Johnson, D. C. 1991, "New Synthetic Approach to Extended Solids: Selective Synthesis of Iron Silicates via the Amorphous State", *Journal of the American Chemical Society*, vol. 113, pp. 3398-3403.

Novet, T., McConnell, J. M., & Johnson, D. C. 1992, "Low-Temperature Reaction of Buried Metal-Silicon Interfaces: The Evolution of Interfacial Structure", *Chemistry of Materials*, vol. 4, pp. 473-478.

Ormerod, M. 2002, "Solid Oxide Fuel Cells", *Chemical Society Reviews*, vol. 32, pp. 17-28.

Palcut, M., Wiik, K., & Grande, T. 2007, "Cation Self-Diffusion in $LaCoO_3$ and La_2CoO_4 Studied by Diffusion Couple Experiments", *Journal of Physical Chemistry B*, vol. 111, pp. 2299-2308.

Poltavets, V. V., Lokshin, K. A., Egami, T., & Greenblatt, M. 2006, "The Oxygen Deficient Ruddlesden-Popper $La_3Ni_2O_{7-\delta}$ ($\delta = 0.65$) Phase: Structure and Properties", *Materials Research Bulletin*, vol. 41, pp. 955-960.

Porob, D. G. & Maggard, P. A. 2006, "Synthesis of Textured $Bi_5Ti_3FeO_{15}$ and $LaBi_4Ti_3FeO_{15}$ Ferroelectric Layered Aurivillius Phases by Molten-Salt Flux Methods", *Materials Research Bulletin*, vol. 41, pp. 1513-1519.

Pullar, R. C., Zhang, Y., Chen, L., Yang, S., Evans, J. R. G., & Alford, N. M. 2007a, "Manufacture and Measurement of Combinatorial Libraries of Dielectric Ceramics. Part I: Physical Characterisation of $Ba_{1-x}Sr_xTiO_3$ Libraries", *Journal of the European Ceramic Society*, vol. 27, pp. 3861-3865.

Pullar, R. C., Zhang, Y., Chen, L., Yang, S., Evans, J. R. G., Petrov, P. K., Salak, A. N., Kiselev, D. A., Kholkin, A. L., Ferreira, V. M., & Alford, N. M. 2007b, "Manufacture and Measurement of Combinatorial Libraries of Dielectric Ceramics. Part II: Dielectric Measurements of $Ba_{1-x}Sr_xTiO_3$ Libraries", *Journal of the European Ceramic Society*, vol. 27, pp. 4437-4443.

Reichelt, K. & Jiang, X. 1990, "The Preparation of Thin Films by Physical Vapour Deposition Methods", *Thin Solid Films*, vol. 191, pp. 91-126.

Ruddlesden, S. N. & Popper, P. 1957, "New Compounds of the K_2NiF_4 Type", *Acta.Crystallographica*, vol. 10, pp. 538-539.

Ruddlesden, S. N. & Popper, P. 1958, "The Compound $Sr_3Ti_2O_7$ and its Structure", *Acta.Crystallographica*, vol. 11, pp. 54-55.

Shannon, R. D. & Prewitt, C. T. 1969, "Effective Ionic Radii in Oxides and Fluorides", *Acta.Crystallographica*, vol. B25, pp. 925-946.

Skinner, S. J. 2001, "Recent Advances in Perovskite-Type Materials for Solid Oxide Fuel Cell Cathodes", *International Journal of Inorganic Materials*, vol. 3, pp. 113-121.

Sreedhar, K., McElfresh, M., Perry, D., Kim, D., Metcalf, P., & Honig, J. M. 1994, "Low-Temperature Electronic Properties of the $La_{n+1}Ni_nO_{3n+1}$ (n = 2, 3, and infinity) System: Evidence for a Crossover from Fluctuating-Valence to Fermi-Liquid-Like Behaviour", *Journal of Solid State Chemistry*, vol. 110, pp. 208-215.

Stein, A., Keller, S. W., & Mallouk, T. E. 1993, "Turning Down the Heat: Design and Mechanism in Solid-State Synthesis", *Science*, vol. 259, pp. 1558-1564.

Takahashi, S., Nishimoto, S., Matsuda, M., & Miyake, M. 2010, "Electrode Properties of the Ruddlesden-Popper Series, $La_{n+1}Ni_nO_{3n+1}$ (n = 1, 2, and 3), as Intermediate-Temperature Solid Oxide Fuel Cells", *Journal of the American Ceramic Society*, vol. 93, pp. 2329-2333.

Tarancón, A., Burriel, M., Santiso, J., Skinner, S. J., & Kilner, J. A. 2010, "Advances in Layered Oxide Cathodes for Intermediate Temperature Solid Oxide Fuel Cells", *Journal of Materials Chemistry*, vol. 20, pp. 3799-3813.

Tarancón, A., Skinner, S. J., Chater, R. J., Hernández-Ramírez, F., & Kilner, J. A. 2007, "Layered Perovskites as Promising Cathodes for Intermediate Temperature Solid Oxide Fuel Cells", *Journal of Materials Chemistry*, vol. 17, pp. 3175-3181.

Taskin, A. A., Lavrov, A. N., & Ando, Y. 2007, "Fast Oxygen Diffusion in A-Site Ordered Perovskites", *Progress in Solid State Chemistry*, vol. 35, pp. 481-490.

Thorne, J. S., Sanderson, R. J., Dahn, J. R., & Dunlap, R. A. 2010, "Combinatorial Study of the Sn-Cu-C System for Li-Ion Battery Negative Electrode Materials", *Journal of the Electrochemical Society*, vol. 157, p. A1085-A1091.

Toby, B. H. 2001, "EXPGUI, A Graphical User Interface for GSAS", *Journal of Applied Crystallography*, vol. 34, pp. 210-213.

Tsipis, E. V., Patrakeev, M. V., Waerenborgh, J. C., Pivac, Y. V., Markov, A. A., Gaczynski, P., Naumovich, E. N., & Kharton, V. V. 2007, "Oxygen Non-Stoichiometry of $Ln_4Ni_{2.7}Fe_{0.3}O_{10-\delta}$ (Ln = La, Pr)", *Journal of Solid State Chemistry*, vol. 180, pp. 1902-1910.

Ueda, K., Tabata, H., & Kawai, T. 1998, "Ferromagnatism in $LaFeO_3$-$LaCrO_3$ Superlattices", *Science*, vol. 280, pp. 1064-1066.

Van der Pauw, L. 1958a, "A Method of Measuring Specific Resistivity and Hall Effect of Discs of Arbitrary Shape", *Phillips Research Papers*, vol. 13, pp. 1-9.

Van der Pauw, L. 1958b, "A Method of Measuring the Resistivity and Hall Coefficient on Lamelae of Arbitrary Shape", *Phillips Technical Review*, vol. 20, pp. 220-224.

Voronin, V. I., Berger, I. F., Cherepanov, V. A., Gavrilova, L. Y., Petrov, A. N., Ancharov, A. I., Tolochko, B. P., & Nikitenko, S. G. 2001, "Neutron Diffraction, Synchrotron Radiation and EXAFS Spectroscopy Study of Crystal Structure Peculiarities of the Lanthanum Nickelates $La_{n+1}Ni_nOy$ (n = 1, 2, 3)", *Nuclear Instruments and Methods in Physics Research*, vol. 470, pp. 202-209.

Wagner, C. 1969, "The Evaluation of Data Obtained with Diffusion Couples of Binary Single-Phase and Multiphase Systems", *Acta Metallurgica*, vol. 71, pp. 99-107.

Weingärtner, H. & Franck, E. U. 2005, "Supercritical Water as a Solvent", *Angewandte Chemie International Edition*, vol. 44, pp. 2672-2692.

Weng, X., Boldrin, P., Abrahams, I., Skinner, S. J., Kellici, S., & Darr, J. A. 2008, "Direct Synthesis of $La_{n+1}Ni_nO_{3n+1}$ Phases (n = 1, 2, 3 and infinity) from Nanosized Co-Crystallites", *Journal of Solid State Chemistry*, vol. 181, pp. 1123-1132.

Weng, X., Brett, D., Yufit, V., Shearing, P., Brandon, N., Reece, M., Yan, H., Tighe, C., & Darr, J. A. 2010, "Highly Conductive Low Nickel Content Nano-Composite Dense Cermets From Nano-Powders Made Via a Continuous Hydrothermal Synthesis Route", *Solid State Ionics*, vol. 181, pp. 827-834.

Weng, X., Cockcroft, J. K., Hyett, G., Vickers, M., Tang, C. C., Thompson, S. P., Parker, J. E., Knowles, J. C., Rehman, I., Parkin, I. P., Evans, J. R. G., & Darr, J. A. 2009, "High-Throughput Continuous Hydrothermal Flow Synthesis of an Entire Nanoceramic Phase Diagram", *Journal of Combinatorial Chemistry*, vol. 11, pp. 829-834.

Weng, X., Knowles, J. C., Abrahams, I., Wu, Z., & Darr, J. A. 2011, *In Situ Variable Temperature X-ray Diffraction Studies on the Transformations of Nano-Precursors to La-Ni-O Phases*.

Wold, A. & Arnott, R. J. 1959, "Preparation and Crystallographic Properties of the Systems $LaMnO_{3-\delta}$ and$LaMn_{1-x}Ni_xO_{3-\delta}$", *Journal of Physics and Chemistry of Solids*, vol. 9, pp. 176-180.

Xu, C., Lee, J., & Teja, A. S. 2008, "Continuous Hydrothermal Synthesis of Lithium Iron Phosphate Particles in Subcritical and Supercritical Water", *Journal of Supercritical Fluids*, vol. 44, pp. 92-97.

Yamamoto, O., Takeda, Y., Kanno, R., & Noda, M. 1987, "Perovskite-Type Oxides as Oxygen Electrodes for High-Temperature Oxide Fuel Cells", *Solid State Ionics*, vol. 22, pp. 241-246.

Yan, L., Niu, H., Bridges, C. A., Marshall, P. A., Hadermann, J., Tendeloo, G., Chalker, P. R., & Rosseinsky, M. J. 2007, "Unit-Cell-Level Assembly of Metastable Transition-Metal Oxides by Pulsed-Laser Deposition", *Angewandte Chemie International Edition*, vol. 46, pp. 4539-4542.

Zhang, D. L. 2004, "Processing of Advanced Materials Using High-Energy Mechanical Milling", *Progress in Materials Science*, vol. 49, pp. 537-560.

Zhang, Z., Brown, S., Goodall, J. B. M., Weng, X., Thompson, K., Gong, K., Kellici, S., Clark, R. J. H., Evans, J. R. G., & Darr, J. A. 2009, "Direct Continuous Hydrothermal Synthesis of High Surface Area Nanosized Titania", *Journal of Alloys and Compounds*, vol. 476, pp. 451-456.

Zhang, Z. & Greenblatt, M. 1995, "Synthesis, Structure and Properties of $Ln_4Ni_3O_{10-\delta}$ (Ln = La, Pr, and Nd)", *Journal of Solid State Chemistry*, vol. 117, pp. 236-246.

Zhang, Z., Greenblatt, M., & Goodenough, J. B. 1994, "Synthesis, Structure and Properties of the Layered Perovskite $La_3Ni_2O_{7-\delta}$", *Journal of Solid State Chemistry*, vol. 108, pp. 402-409.

Zhu, B., Wang, Z., Zhang, Y., Yu, Z., Shi, J., & Xiong, R. 2009, "Low Temperature Fabrication of the Giant Dielectric Material $CaCu_3Ti_4O_{12}$ by Oxalate Coprecipitation Method", *Materials Chemistry and Physics*, vol. 113, pp. 746-748.

Appendix — RAMSI Design

Appendix figure 1. Photograph of the pre-synthesis stage of RAMSI. The synthesis is controlled from the computer terminal. Figure adapted from the supplementary information from (Lin *et al.* 2011).

Appendix figure 2. Close-up photograph of the mixing pot shown in appendix figure 1. Aqueous metal nitrate salts were metered in stoichiometric quantities into the mixing point before being taken up by the ISCO syringe pump. Figure adapted from the supplementary information from (Lin *et al.* 2011).

Appendix figure 3. Photograph of the synthesis section of RAMSI. Metal salts are pumped from the ISCO syringe pump on the right, and into the reactor on the left. HC = heater controller CC = collection carousel and BPR = back-pressure regulator. Figure adapted from the supplementary information from (Lin *et al.* 2011).

Appendix figure 4. Photograph of the collection carousel, where tubes are placed, filled and the collected. Figure adapted from the supplementary information from (Lin *et al.* 2011).

Appendix figure 5. Blueprint of the RAMSI layout, including synthesis, clean-up and printing sections. Figure adapted from the supplementary information from (Lin *et al.* 2011).

Appendix figure 6. Photograph of the layout of the clean-up and printing sections of RAMSI. Figure adapted from the supplementary information from (Lin *et al.* 2011).

Appendix figure 7. Photograph of the clean-up carousel of RAMSI. Figure adapted from the supplementary information from (Lin *et al.* 2011).

Appendix figure 8. Photograph of the printing section of RAMSI. Figure adapted from the supplementary information from (Lin *et al.* 2011).

Appendix figure 9. RAMSI GUI interface showing: a) experiment assignment status, b) experiment setting and result, c) sample tracking, d) synthesis procedure status and e) synthesis real-time measurement. Figure adapted from the supplementary information from (Lin *et al.* 2011).

Publications

1. J. Parker, S. Thompson, T. Cobb, F. Yuan, J. Potter, A. Lennie, **S. Alexander**, C. Tighe, J, Darr, J. Cockcroft, C. Tang. High-throughput powder diffraction on beamline I11 at Diamond, *J. Appl. Cryst.* 2011, **44** 102-110. Impact factor = 3.02, citations = 1.

Manuscripts submitted and in preparation

2. **S. Alexander,** T. Lin, D. Brett, J. Evans, G. Cibin, A. Dent, G. Sankar, J. Darr. A combinatorial nanoprecursor route for direct solid state chemistry; discovery and electrical properties of new iron doped lanthanum nickelates up to $La_4Ni_2FeO_{10-\delta}$, *Solid State Ionics*, Submitted.

3. **S. Alexander**, R. Gruar, J. Darr. Continuous hydrothermal flow synthesis of bismuth doped ceria metastable kinetic phases, *Journal of Solid State Chemistry*, Submitted

4. **S. Alexander,** J. Darr. Combinatorial parallel synthesis of $La_4Ni_{2.7}M_{0.3}O_{10}$ from nanosized precursors; where M = V, Cr, Mn, Fe, Co and Al. In preparation for *ACS Combinatorial Science.*

5. **S. Alexander,** J. Cockcroft, J. Parker, C. Tang, J. Darr. In-Situ Variable Temperature Synchrotron Diffraction of the Direct Synthesis of $La_4Ni_3O_{10-\delta}$. In preparation for *Journal of Solid State Chemistry.*

6. J. Cockcroft, **S. Alexander,** S. Mason, J. Darr. Revealing the Nature of the Phase Discontinuity in the Ceria-Yttria Binary System. In preparation for *Journal of Materials Chemistry.*

7. R. Quesada Cabrera, C. Tighe, R. Gruar, **S. Alexander**, J. Goodall, J. Darr, Scale-Up Continuous Hydrothermal Synthesis of Zn-Ce Mixed Oxides. In preparation.